UNIVERSIDADE DE LISBOA
FACULDADE DE CIÊNCIAS
DEPARTAMENTO DE ENGENHARIA GEOGRÁFICA, GEOFÍSICA E ENERGIA

Post-rift magmatism on the Central West Iberian Margin (Estremadura Spur): new evidences from potential field data

Cláudia Cristina Araújo Escada

Mestrado em Ciências Geofísicas
Especialização em Geofísica Interna

Dissertação orientada por:
Professor Doutor Fernando Acácio Monteiro dos Santos
Doutora Patrícia Machado Madureira Fontes Represas

2019

To my Father, Rui.

In memory of my Grandmother, Salete.

Physicists believe that known laws should suffice to explain the Earth's behaviour, but the complexities of geology have defied simple explanation.

*(*John Tuzo Wilson, 1908-1993)

Acknowledgements

The path was long and made of ups and downs, but I must confess that it was the highs that define it, especially for the presence of all the people who surrounded me during this project. This thesis is also the beginning of my journey through the mysteries of geophysics. It's a new world that I do not regret to know, and I want to continue exploring.

I must start by thanking my supervisors. To Professor Fernando Santos, due to his experience and genuine appreciation for geophysics which allowed me to learn a lot of the essential things for the execution of this thesis. To Patrícia Represas, who was always present to assist me in last minute geophysical doubts and, especially many (and many…) questions related to the software. Your knowledge enabled me to look at geophysics from another perspective. I could not have chosen better supervisors it was a great pleasure to work with both of them.

To Ricardo Pereira, although he is not one of my "official" supervisors, that's how I saw him during this past year. I want to thank you for the hours of discussion that enabled me to think "outside the box" and understanding the theme of this thesis from a global perspective. I appreciate all the tireless corrections that have greatly improve the thesis.

I am grateful to Partex Oil and Gas for supporting this project, namely for financial support of my participation in the General Assembly EGU 2019, where it was presented a poster about the work developed in this thesis. I would like to thank Eng. Luis Guerreiro for making this possible.

To Pedro and Jennifer (plus Lucas, the fieldwork team!), for all the crazy talking and ideas during our long field days. Our idea was not forgotten, guys!

To the most powerful list of friends which I want to thank for all the fondness, concern and encouragement: Bibi, Carolina Marques, Daniela, Carolina, Margarida, Analdyne, Marta and, although the distance, to Sofia. Thank you for everything, girls!

To Tia Eugénia (and her famous chocolate salami!). To Vasco, for all the affection. And, not less important, to my Tia Zizinha, for all of her words.

To Alf (my cat…), for his unconditional love and company, always present during the long hours in front of the computer.

To my sister, Rita, for all of her patience during several weekends and to always cheer me up with board games, which we both love! To my mother, Cristina, who despite not being by my side, was always there for me to cheer me up with her good mood, positivism and contagious energy.

To Fábio, for being the most patient person in the world. Thanks for all of the conversations (even though he didn't realize anything I was saying…). I am grateful for all of your support and for always be there for me in the good and bad times. Thank you for being who you are!

My biggest and most special thank you goes to my dad, Rui. From the very beginning, he was the foundation stone (here it comes the geology!) that gave me the strength, the courage and the confidence to move on. Thank you for showing me that everything is possible. Thank you for all the words of encouragement, not only through my academic life, but also throughout my life, and for all the support, not only financial, mas must importantly, emotional. Without you none of this would be possible, I am eternally grateful to you!

Lastly, I want to give a huge thank you to my grandmother, Salete, although she is no longer with us, I know that she guided me throughout this journey and was always by my side, and still is...

Abstract

Rifted continental margins are one of the most complex geological entities, being intensively studied not only from the academic point of view, but also for their economic importance, due to the occurrence of geological resources, from which oil and natural gas comprise the vast majority. Understanding the geological process that underpin the formation and evolution of these resources led academia and industry, to scrutinize this type of margins.

This study is grounded in recent advances in the knowledge of continental rifting and post-breakup of West Iberia, and in the discovery of an enigmatic geological feature located southwest of the Fontanelas volcano. This feature, whose nature and geometry are unknown, was identified based on new 3D seismic data offshore central Portugal, in the Estremadura Spur. Its seismic signature and similarity with the Sintra massif (shape and areal extent), suggest that it might correspond to a magmatic intrusion, with a batholith shape and granitic nature. This feature is described here for the first time therefore it was named as Estremadura Spur Intrusion (ESI).

This thesis proposes to characterise the geometry and nature of the Estremadura Spur Intrusion and the Fontanelas volcano, based on potential field data (i.e. gravity and magnetic) modelling supported and constrained by evidence from seismic profiles, and correlate the ESI with the Late Cretaceous post-rift magmatic event.

Firstly, a qualitative analysis of potential field data was performed based on signal enhancement techniques, focusing on the characterization of the main regional geological features, in order to frame the area under study. Overall, the gravity and magnetic anomaly associated with the ESI produces a nearly circular shape, confirming its outline from the 3D seismic data. On the other hand, the gravity anomaly of the Fontanelas volcano is more diffuse than the one from the ESI, while its magnetic anomaly it is much better constrained by an approximately circular geometry. Both targets have a strong geophysical signal, being distinguished from other regional features, indicating its importance on the West Iberian Margin and, more significantly, in the Estremadura Spur setting.

Subsequently, building on the regional interpretation, a more detailed analysis was performed through 2.5D modelling of potential field data, over a seismic line across the centre of the intrusion and the southeast flank of the Fontanelas volcano, with the aim to characterise both features, including their magmatic nature and geometry.

The Fontanelas volcano is characterised by an overall triangular shape, with a longer and deeper southern flank. This magmatic feature was subdivided into two segments: a seawater-rock contact zone and a buried zone, by Tertiary sediments. The density and susceptibility values determined for its buried sector (not in contact with the seawater) were interpreted as basalt. The lower density and susceptibility values associated with the seawater-Fontanelas contact zone are caused by the alteration of its original basaltic rock. This interpretation corroborates with the results of published work on the Fontanelas volcano.

Regarding the Estremadura Spur Intrusion, its geometry is interpreted as a laccolith (sheet-like magmatic structure). Although the conclusions regarding its magmatic affinities were not straightforward, the values of density and susceptibility obtained for this magmatic feature suggest the presence of a predominantly gabbroic intrusion, according to similarities, concerning its nature, with outcropping intrusions, such as Sintra and Sines massifs.

The seismic stratigraphic interpretation and the similarities between onshore (Sintra and Sines massifs and Foz da Fonte sill) and offshore (Guadalquivir-Portimão intrusion) analogues on the West

Iberian Margin, suggest a link between the Estremadura Spur Intrusion and the Late Cretaceous post-rift magmatic event.

The results obtained in this thesis may have implications on the current models describing the evolution of the Iberian margin, the existing magmatic models and emplacement mechanisms of the Late Cretaceous magmatic event as well as on petroleum systems.

Keywords: West Iberian Margin, Estremadura Spur, Fontanelas, Gravity, Magnetism.

Resumo

As margens continentais do tipo rifte são uma das mais complexas entidades geológicas, tendo sido intensivamente estudadas não apenas do ponto de vista académico, mas também pela sua importância económica, devido há ocorrências de recursos geológicos, dos quais o petróleo e o gás natural compõem a grande maioria. Compreender os processos geológicos subjacentes à formação e evolução destes recursos económicos conduziu a academia e a indústria a investigar este tipo de margens.

Este estudo tem os seus alicerces nos mais recentes progressos realizados ao nível do conhecimento dos processos de *rifting* continental e pós-rutura continental da Margem Oeste Ibérica. A aquisição de novos dados de sísmica 3D recolhidos ao largo de Portugal permitiram a descoberta de uma nova e enigmática estrutura geológica localizada a sudoeste do conhecido vulcão de Fontanelas, no promontório submarino, designado por Esporão da Estremadura. Inicialmente, devido à sua assinatura sísmica e semelhanças com o maciço de Sintra, estra estrutura foi associada a uma intrusão magmática de natureza granítica e geometria do tipo batólito.

Esta tese propõe a caraterização da natureza magmática e geometria desta intrusão, e do vulcão de Fontanelas, baseada na modelação de dados de campo potencial (isto é, gravimetria e magnetismo) constrangida por dados sísmicos, bem como relacioná-la com o evento magmático pós-rifte do Cretácico Superior.

Durante o Mesozóico, a Margem Oeste Ibérica foi pontuada por três ciclos de atividade magmática: 1) ciclo toleítico do Triásico-Jurássico (200-198 Ma), 2) ciclo levemente alcalino do Jurássico-Cretácico (148-140 Ma) e 3) ciclo alcalino do Cretácico Superior (94-69 Ma). Os dois primeiros pulsos magmáticos são associados aos eventos de rifte do Triássico Superior e do Jurássico Superior, respetivamente, sendo, por isso, eventos magmáticos sin-rifte. O último ciclo magmático foi o mais volumoso e generalizado ao longo da Margem Oeste Ibérica, ocorrendo num contexto tectónico pós-rifte.

O evento magmático do Cretácico Superior é subdivido em dois pulsos alcalinos, que revelam o papel de uma fonte mantélica sub-listosférica, contrastando com a natureza dos magmas dos ciclos anteriores. As evidências destes dois ciclos magmáticos incluem: 1) sills e diques na região de Lisboa (com cerca de 98 Ma) e 2) o Complexo Vulcânico de Lisboa (72.6 ± 3.1 Ma), os maciços ígneos de Sintra (~79 Ma), Sines (75.4 ± 0.6 Ma) e Monchique (72.7 ± 2.7 Ma). Recentemente, foram também descritos, como parte deste ciclo, o magmatismo associado à montanha submarina Madeira-Tore e à intrusão de Guadalquivir-Portimão, localizada na bacia do Algarve.

Este estudo compreende a primeira descrição da intrusão, tendo sido nomeada de acordo com a sua localização, como Intrusão do Esporão da Estremadura (*Estremadura Spur Intrusion* – ESI). Esta intrusão e o vulcão de Fontanelas são os principais alvos deste trabalho e foram estudados devido à disponibilidade de dados de campo potencial e dados sísmicos recolhidos ao largo de Lisboa, durante duas campanhas sísmicas realizadas em 2008 (2D) e 2010 (3D), respetivamente. Neste estudo, os dados de campo potencial foram constrangidos pela informação dos dados de sísmica 3D. A disponibilidade destes três conjuntos de dados (gravimetria, magnetismo e sísmica) permitiu o acesso a várias fontes de informação, tais como estrutural, pela interpretação dos perfis sísmicos, e física, pela obtenção de valores de densidade e suscetibilidade através da modelação de dados de gravimetria e magnetismo, respetivamente.

O uso de dados de campo potencial tem várias vantagens, incluindo o facto de ser um método geofísico passivo e não-destrutivo, a sua aquisição é mais rápida e barato que a maioria dos métodos geofísicos, os dados podem ser adquiridos simultaneamente com outro tipo de aquisições, além das

suas múltiplas aplicações, nas quais se incluem, engenharia, ambiental, estudos geotérmicos, entre outros. Por outro lado, a maior desvantagem associada à utilização dos dados de campo potencial está relacionada com a não-unicidade dos resultados, sendo necessárias outras fontes de informação que permitam interpretar e validar os mesmos. Contudo, os dados de campo potencial poderão fornecer uma grande variedade de informação e, pelas suas inúmeras vantagens, serem um dos melhores métodos geofísicos a ser aplicados em áreas conhecidas e desconhecidas.

No contexto deste trabalho, a utilização de dados de campo potencial é bastante vantajosa, uma vez que é esperado que os valores de densidade e suscetibilidade das estruturas magmáticas em estudo se destaquem das estruturas de fundo como zonas anómalas, sendo estas facilmente reconhecidas de entre as demais presentes na área de estudo.

Numa primeira abordagem, foi realizada uma análise qualitativa dos dados de campo potencial, através de técnicas de processamento do sinal, com o foco na caraterização das principais estruturas geológicas a nível regional. A anomalia da Intrusão do Esporão da Estremadura é representada por uma forma aproximadamente circular, confirmando o contorno obtido pelos dados da sísmica 3D. Por outro lado, o vulcão de Fontanelas exibe uma geometria diferente consoante os dados gravimétricos ou magnéticos. Nos dados gravimétricos a sua geometria é difusa, não expressando uma forma bem definida e espacialmente constrangida, ao contrário dos dados magnéticos, cuja forma é aproximadamente circular. Em ambos os alvos, o sinal geofísico é forte e permite distinguir tanto a ESI como o vulcão de Fontanelas de outras estruturas regionais, revelando a sua importância no contexto da Margem Oeste Ibérica, mas mais importante ainda, na região do Esporão da Estremadura.

Subsequentemente, a interpretação regional serviu de base a uma análise local com o objetivo de caraterizar de forma mais detalhada os alvos magmáticos deste estudo. Esta análise foi executada através da modelação 2.5D dos dados de campo potencial, sobre uma linha sísmica que se estende desde o centro da ESI ao flanco sudeste do vulcão de Fontanelas. O principal objetivo da modelação é caraterizar tanto a natureza magmática, como também a geometria de ambas estas estruturas.

O vulcão de Fontanelas é caraterizado por uma forma triangular, caraterística dos vulcões, com o flanco sul mais longo e com uma maior extensão em profundidade. Esta estrutura magmática foi subdividida em dois segmentos: uma zona de contacto água-rocha e uma outra zona que se encontra soterrada por sedimentos do Terciário. Os valores de densidade e suscetibilidade determinadas para o setor soterrado (i.e., que não se encontra em contato com a água do mar) permitiram interpretar a sua litologia como um basalto. Por outro lado, o setor que se encontra em contato com a água do mar é caraterizado por valores de densidade e suscetibilidade menores devido à alteração da rocha basáltica original que constitui o vulcão. Esta interpretação corrobora com dados publicados, nos quais se realizou uma dragagem e onde se obtiveram amostras de rocha que permitiram identificar a natureza do vulcão de Fontanelas como um basalto alterado.

No que diz respeito à Intrusão do Esporão da Estremadura, a sua geometria foi interpretada como um lacólito (estrutura magmática em forma de folha). Relativamente, à sua afinidade magmática as conclusões não foram tão diretas e claras, no entanto os valores de densidade e suscetibilidade associados à intrusão sugeriram a presença de uma natureza predominantemente gabróica.

Os resultados obtidos através da modelação 2.5D, mais concretamente os valores de densidade e suscetibilidade magnética, são semelhantes a corpos magmáticos em *onshore* (maciços de Sintra e Sines e sill da Foz da Fonte) e *offshore* da margem do Algarve (intrusão Portimão-Guadalquivir). De acordo com os resultados obtidos neste estudo através da modelação bem como da informação da estratigrafia sísmica e as semelhanças com os análogos presentes na Margem Oeste Ibérica foi possível associar esta intrusão ao evento magmático pós-rifte do Cretácico Superior.

Os resultados obtidos têm implicações nos atuais modelos de evolução que descrevem a margem Ibérica, nos modelos magmáticos e respetivos mecanismos de instalação do evento magmático do Cretácico Superior, bem como nos sistemas petrolíferos.

Palavras-chave: Margem Oeste Ibérica, Esporão da Estremadura, Fontanelas, Gravimetria, Magnetismo.

Table of contents

List of figures

List of tables

Acronyms

ESI	Estremadura Spur Intrusion
IGRF	International Geomagnetic Reference Field
RTP	Reduced to Pole
WIM	West Iberian Margin

Chapter 1: Introduction

1.1.Rationale

Rifted continental margins are one of the most complex geological entities, being intensively studied not only from the academic point of view, but also for their economic importance, due to the occurrence of geological resources, from which oil and natural gas comprise the vast majority. Understanding the geological process that underpin the formation and evolution of these resources led academia and industry, to scrutinize this type of margins. Newfoundland is an example of a proliferous margin, concerning the petroleum and mineral exploitation, contrasting with the absence of known economic geological resources of the West Iberian Margin (WIM, corresponding to the Atlantic margin of Portugal and Spain). Economic aspects apart, these conjugated margins were, and continue to be, an important key to define the geological context associated with the continental margins (e.g. Wilson et al., 2001; Manatschal et al., 2010).

The West Iberian Margin is one of the best-studied continental margins and, in addition to the many published papers (e.g. Boillot et al., 1979; Pinheiro et al., 1996; Wilson et al., 2001; Russell and Whitmarsh, 2003; Manatschal, 2004; Reston, 2007; Tucholke and Sibuet, 2007; Alves et al., 2009; Manatschal et al., 2010; Martins et al., 2010; Pereira and Alves, 2011; Pereira et al., 2017), this margin has also been the subject of the Deep Sea Drilling Project (DSDP), the Ocean Drilling Program (ODP), numerous seismic experiments, as well as other variety of geological, geophysical and biological studies.

This master's thesis is incorporated on a partnership between the Faculty of Science of the University of Lisbon (FCUL) and Partex Oil and Gas, under the scope of the wider project entitled "Magmatism on passive margins and its implications for effective petroleum systems in the Atlantic: a case study from West Iberian Margin", in which the major goal is to investigate magmatism on the West Iberian Margin and its contribution on petroleum systems.

The motivation of this study is grounded in the recent advances in the knowledge of continental rifting and post-breakup of West Iberia (e.g. Alves et al., 2009; Pereira and Alves, 2011; Soares et al., 2012) and also in the discovery of an enigmatic geological feature located southwest of the Fontanelas volcano (e.g. Pereira et al., 2017). This feature was identified based on new 3D seismic data offshore central Portugal (Pereira, personal communication), in the Estremadura Spur. Its nature and geometry are unknown, although, according to its seismic stratigraphic criteria (including, the information from the seismic facies and reflectors; Figure 1.1), it likely correspond to a magmatic intrusion with a granitic nature and batholith shape.

The interpretation of seismic profiles provides important information about the geometry /structure of the bodies, as well as the relative geological ages through seismic stratigraphy and, consequently, suggests a possible lithology.

In this thesis it is proposed a geophysical characterisation of the intrusion and of the Fontanelas volcano, which will led to a geological description of the possible lithology and geometries associated with both targets. This task will be accomplished by applying qualitative (signal enhancement techniques) and quantitative (2.5D modelling) methods to potential field data (gravity and magnetic) constrained by seismic data.

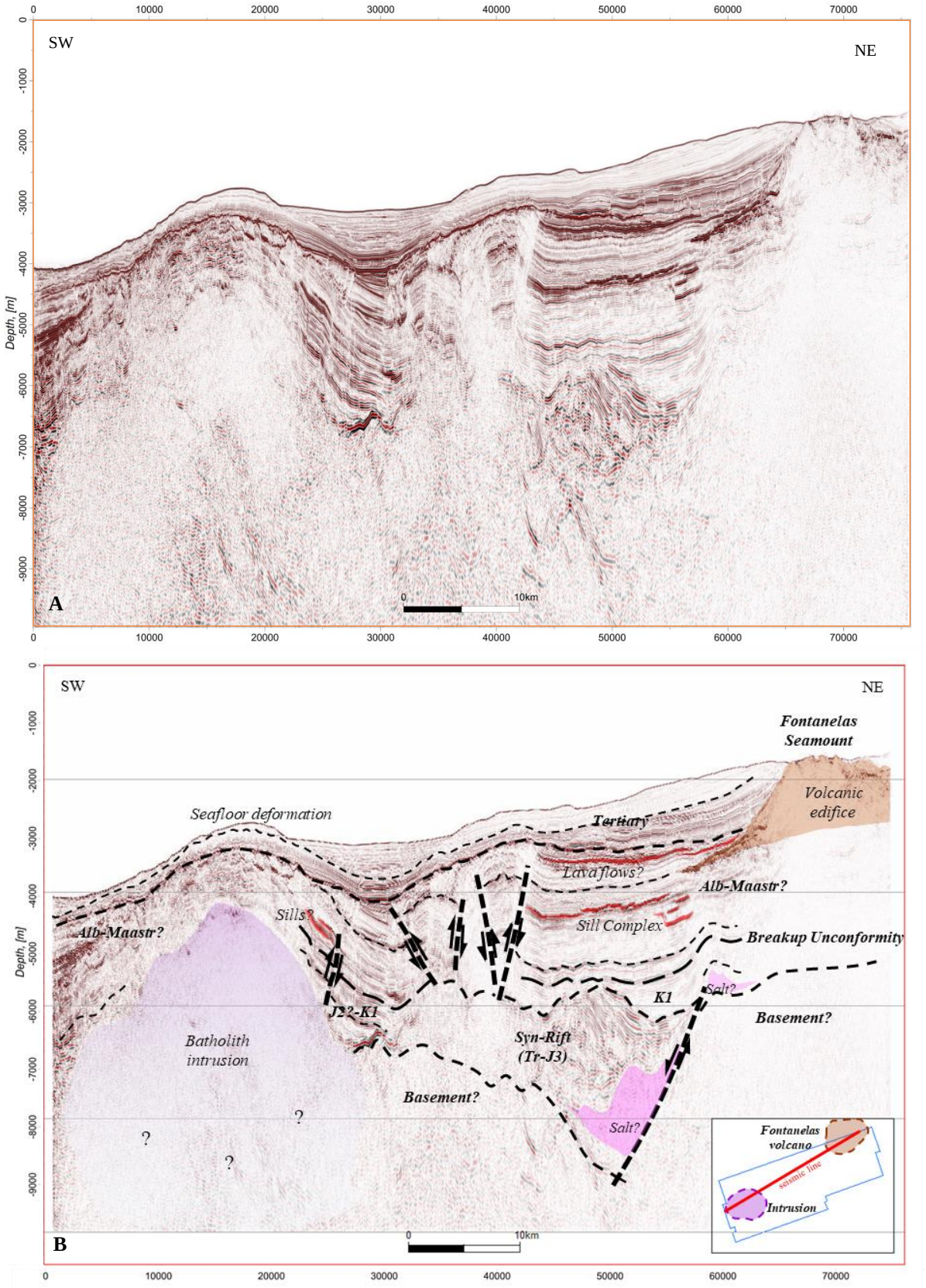

Figure 1.1. Seismic profile (A) not interpreted and (B) interpreted. This seismic profile is an important source of information to this study, since it shows both the intrusion and the volcano magmatic features. It is also based on this seismic profile that the modelling of gravity and magnetic data was performed.

The importance of this study is supported by numerous aspects, including: 1) knowledge of a new area; 2) knowledge of a new magmatic feature, which has never been studied before; 3) study of a paleo-volcano that has never been studied through potential field data and 4) explore the potentiality of gravity and magnetic data, as well as the methodology applied to improve the characterisation of shallow magmatic plumbing systems (e.g. Magee et al., 2018).

Regarding the presence of magmatic features on the offshore areas of the WIM, this study contributes to increase the knowledge on its thermal evolution and, ultimately, on the regional effects on widespread uplift and impact on postulated petroleum systems. Despite its regional implications, this study may also be important in clarifying the importance of magmatic events on continental margins worldwide, especially in margins throughout the Atlantic.

1.2.Magmatism on passive continental margins

The classification of continental margins resulting from extension of the lithosphere was first introduce by Sengör and Burke (1978), that divide it into “active” and “passive” continental margins, according to the forces that initiated rifting.

Continental rifting is traditionally described as a thinning process of the lithosphere which ultimately leads to continental breakup, formation of a mid-oceanic ridge and seafloor spreading (Merle, 2011). This stretching may result from one of two distinct types of rifting (Corti et al., 2003; Geoffroy, 2005; Merle, 2011). The active rifting is defined by thermal upwelling of the asthenosphere as a result of the ascent of a mantle plume to the base of the lithosphere (Figure 1.2), implying that the mantle upwelling is an active process of the deformation (Merle, 2011). This type of continental rifting is characterised by crustal doming and abundant volcanism during early stages (Merle, 2011).

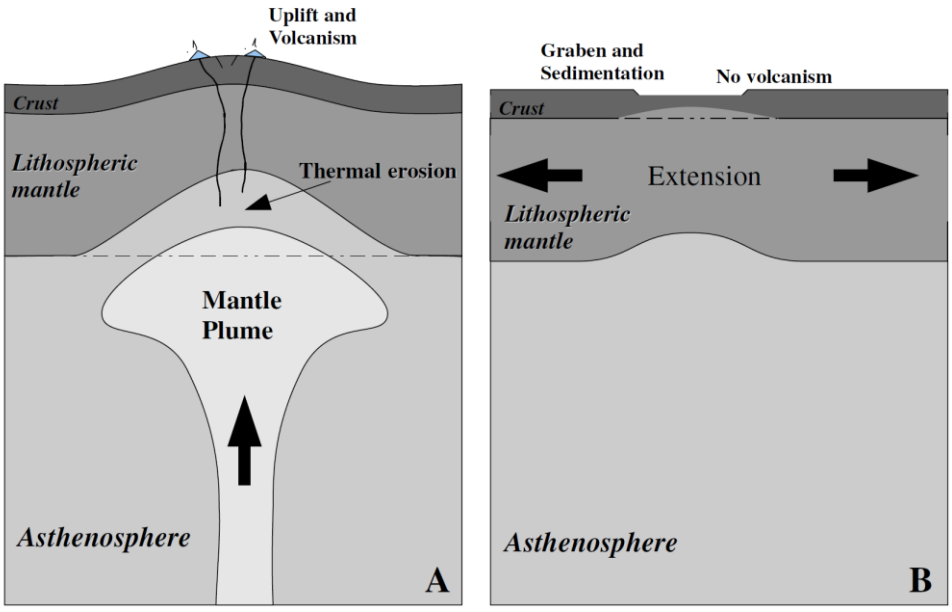

Figure 1.2. Illustration of the early stage of the tectonic evolution for (A) "active" and (B) "passive" rifting. “Active” rifting displays lithospheric uplift and volcanism, whereas “passive” rifting displays graben formation and sedimentation without volcanism. From: Merle (2011).

In passive rifting, the plate tectonics drives to lithospheric extension, as a result of regional stresses located within or at the boundaries of the lithosphere (Geoffroy, 2005; Merle, 2011). The passive rifting exhibits graben formation and marine sedimentation in the first stage, followed by volcanism at

a later stage (Figure 1.2; Merle, 2011), although this type of continental rifting is characterised by a scarcity of igneous activity compared with the active rifting. Nevertheless, the subsidence, and consequent sedimentation, occurs both during the syn- and post-rift stages (Geoffroy, 2005). In this type of margin, the role of magma intrusion in favouring and focusing extension may be important as the lithosphere can be both thermally weakened or compositionally strengthened by cooled mafic intrusion (Geoffroy, 2005).

Passive margins are characterised by variable crustal stretching, rift-related faulting and igneous activity (e.g. Alves et al., 2009). As a result, this type of margin can be subdivided into "volcanic" or "non-volcanic" (see Wilson et al., 2001, and references therein), depending on the timing and relative amount of magmatic activity in relation to lithosphere extension and breakup (Geoffroy, 2005). Manatschal (2004) renamed the "non-volcanic" to "magma-poor" passive margin. This latter term is more appropriate, because there is not a single passive margin that is completely absent of intrusive and extrusive rocks (Franke, 2012; Russell and Whitmarsh, 2003).

Volcanic passive margins (Figure 1.3) are commonly associated with the Large Igneous Provinces (LIP; Geoffroy et al., 2015). The breakup of lithosphere mantle occurs first or during the breakup of the crust, resulting in the extrusion and intrusion of large amounts of syn-rift magmatism. In this case, all stages, until the continental breakup, are accompanied by magmatism (Geoffroy, 2005). One distinctive feature associated with this type of margins, and recognized in the seismic data, is the presence of strongly reflective Seaward Dipping Reflectors (SDR) sequences due to the development of flood-basalts during continental breakup (Geoffroy, 2005).

Magma-poor passive margins (Figure 1.3) are characterized by (Reston, 2016): 1) low-moderate sediment accumulation rates, 2) extreme crustal thinning and highly rotated fault blocks, 3) detachment faults rooting at deep crustal levels and 4) the presence of a transitional domain from the continental to the oceanic crust. The structure of magma-poor margins is known due to their transparency to seismic waves, comparing with the volcanic margins which are poorly constrained due to the strong impedance contrast within the SDRs (Geoffroy, 2005). The best-known examples of magma-poor margins comprise the Brazil-Angola, the NW Australian, the South China Sea and the Iberia-Newfoundland. These latter margins are a type-example in the study of the geometry and processes related to magma-poor rifted margins.

Iberia-Newfoundland margins are characterised by 1) polyphasic rifting, 2) localized deformation, migrating towards the area of final breakup (ocean-continent boundary) and 3) magmatism, which includes underplating, diking and extrusion of alkaline magmas before, during and after continental breakup (Manatschal et al., 2010). As a result of forces exerted in the lithosphere, rifted margins develop distinct crustal architectures during their evolution (Pereira, 2013). According to Manatschal et al. (2010), the Iberia-Newfoundland margins reveals five distinct crustal domains referred to as: proximal margin, necking zone, distal margin, the ocean-continent transition (OCT) and the oceanic crust. These domains contrast with the classical rift models, which distinguish only two main domains: continental and oceanic (Manatschal et al., 2010).

The distal margin is characterised by highly rotated upper crust tilt blocks (Pereira, 2013) and formed by an hyper-extended crust domain, where the crust thins to less than 10 km (Manatschal, 2014; Manatschal and Bernoulli, 1999, 1998). Hyper-extension is defined by an extreme stretching process conducting to a coupled and embrittled lower and upper crust, allowing main faults to penetrate to the mantle (Doré and Lundin, 2015). Mantle exhumation leads to partial hydration (serpentinization) of the uppermost mantle (Doré and Lundin, 2015), in response to depth-dependent extreme thinning and polyphase faulting (Manatschal, 2014; Ocdanologique and Azur, 2001).

Concerning its global geodynamic significance, hyper-extended margins may have significant roles at critical stages of the Wilson Cycle, since the presence of weaker exhumed mantle, due to the partial replacement of peridotite by serpentinite, and the extreme crustal thinning may become important in localizing subduction events (Doré and Lundin, 2015).

As referred previously, this type of rifted margin is not entirely devoid of magmatism. West Iberia (as well as other Atlantic magma-poor margins) shows occasional magmatic activity during the rifting process and subsequent post-rift evolution (Pereira, 2013). Throughout West Iberia, magmatic events are described in the Late Triassic – Early Jurassic, Late Jurassic – Early Cretaceous and in the Late Cretaceous (e.g. Martins et al., 2008; Miranda et al., 2009; Pinheiro et al., 1996; Tucholke and Sibuet, 2007).

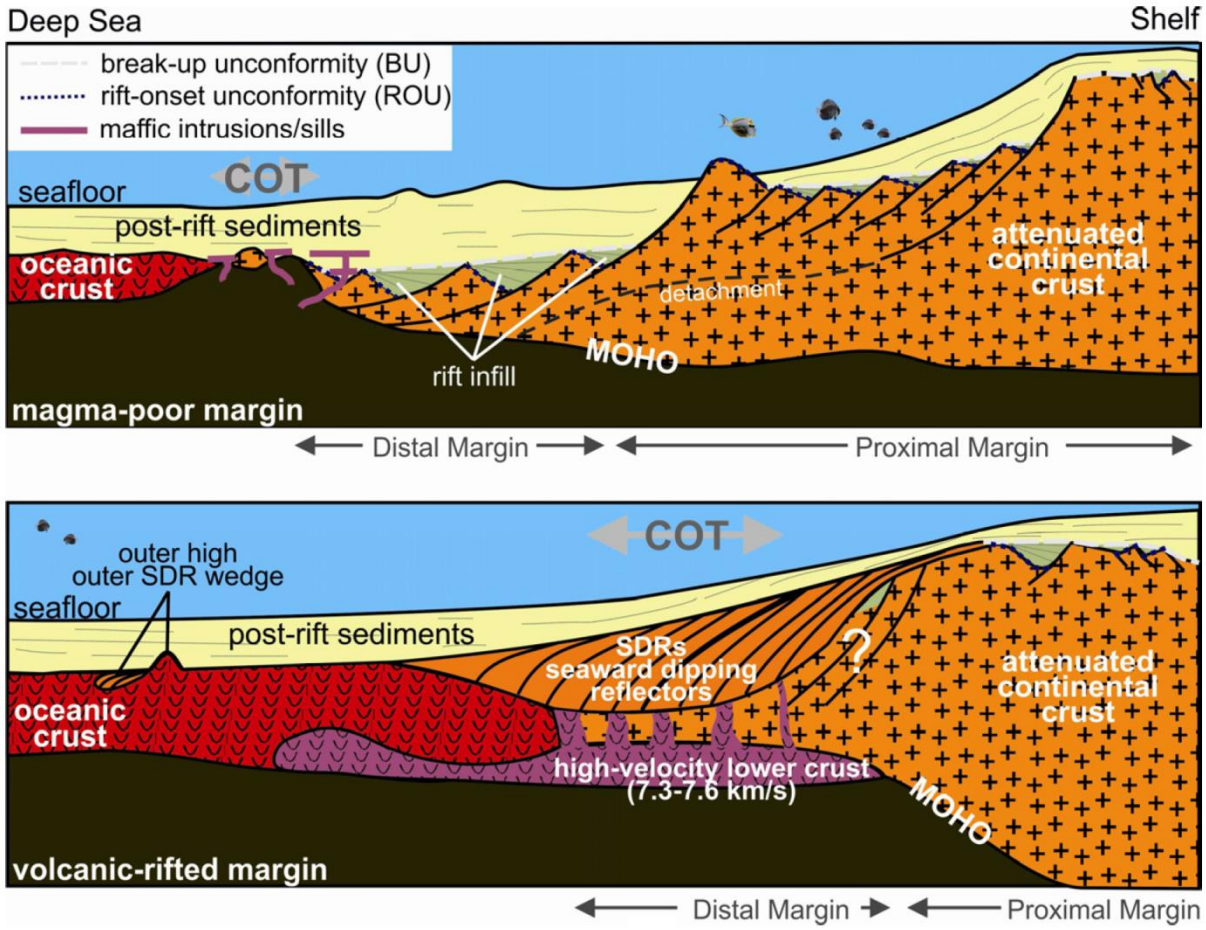

Figure 1.3. Schematic sketch of the end-member extremes of passive continental margins: magma-poor and volcanic rifted margins. SDRs = Seaward Dipping Reflectors; COT = Continent-Ocean Transition. From: Franke (2012).

This study will focus on the latter magmatic cycle (Late Cretaceous) being the most voluminous and widespread episode of the WIM, and responsible for the formation of the onshore complexes of Sintra (Terrinha et al., 2003), Sines (Ribeiro et al., 2013) and Monchique, the volcanic complex of Lisbon and other several minor intrusions, which include the Foz da Fonte (Neres et al., 2014, 2012) and Paço de Ilhas (Neres et al., 2012) sills. Several authors also correlated various offshore seamounts with this magmatic event in the WIM: the Tore Seamount (Neres et al., 2014; Roque et al., 2009), the Fontanelas Seamount (Miranda et al., 2010) and, more recently, the Guadalquivir-Portimão Banks (Neres et al., 2018).

1.3. Potential field data and methodology

A likely magmatic intrusion and the Fontanelas volcano are the main targets of this study. These two magmatic features are studied through potential field data (i.e. gravity and magnetic) acquired during a seismic campaign by Austin Exploration Inc, offshore Portugal, during 2008, as part of industry exploration activities on the margin.

The gravity exploration method consists on the study of the mass distribution in the subsurface. This technique provides information on the density distribution in the crust and allows the identification of anomalous geological features with distinct density, which stands out from the background geology. The gravity method uses measurements of the gravity acceleration at different locations, in the case of this study, aboard a marine vessel. The lithology is one of the possible geological information that can be derived from the gravity data, since the strength of the gravitation field is directly proportional to the mass and, therefore, the density of crustal materials, enabling inference of rock type (Lichoro, n.d.). Besides lithological information, contrasting densities also allows to detect and delineate geological discontinuities, faults, intrusions, dykes, among others (Lichoro, n.d.).

On the other hand, the magnetic method studies the distribution of the magnetic properties (i.e., susceptibility, remanence) in the earth's crust, by recording the variations in the magnetic field due to lateral variability in the magnetization of the magnetic minerals in the crust (Lichoro, n.d.). Similarly to the gravity method, the magnetic method is also able to provide lithological and structural information. The variation of magnetization of magnetic minerals throughout the crust gives rise to magnetic anomalous regions, which are indicative of structural contrasts, allowing the mapping of basements structures, fault systems, dykes and intrusions (Lichoro, n.d.).

The use of potential field data has several advantages: 1) they are a passive and non-destructive geophysical method, 2) the acquisition is faster and cheaper than most geophysical techniques, 3) the data can be acquired simultaneously with other geophysical methods and 4) they have multiple applications (engineering, environmental, geothermal studies, among others). The biggest disadvantage of potential field data is related to the non-uniqueness character of the results, which implies the use of other sources of information to fully interpret and understand the results (Lichoro, n.d.). However, the potential field data can give us a lot of different information and be one of the best geophysical methods to apply in known and unknown areas as a first geophysical approach.

In this study, potential field data was constrained by 3D seismic data. The availability of these three datasets (gravity, magnetic and seismic) allows the access to several pieces of information, such as structural, by the interpretation of seismic profiles, and physical, by obtaining density and susceptibility values with the modelling of gravity and magnetic data, respectively.

Applying potential field data, within the geological context of this work, is very advantageous, because it is expected that the magmatic features under study stand out from the background structures as anomalous zones. Several studies applied potential field data to study the continental margins, e.g. Srivastava et al. (2000), Russell and Whitmarsh (2003), Bronner et al. (2011), Girolami et al. (2016), Casacão et al. (2018), Neres et al., (2018), Bernard et al. (2019) and Sanchez et al. (2019).

Concerning the methodology applied in this work, potential field data was used to perform a regional analysis through enhancement techniques, while the analysis with greater detail was completed by the modelling of the potential field data with the aid of 3D seismic data.

1.4. Location and physiography of the study area

The study area is located in the offshore southwestern part of the continental margin of Portugal, extending from Lisbon to Porto (Figure 1.4). The target magmatic bodies of this study are located in the Estremadura Spur (ES, Figure 1.4), which constitutes an important submarine promontory. With a roughly trapezoidal shape, elongated in an east-west direction, it has about 200 km length and 90 km width, extending from the coastline to the Tore Seamount (Badagola, 2008).

Figure 1.4 shows the location of the regional study area in relation with Iberia, and the polygon at the SW indicates the area where 3D seismic data were acquired, which comprises both the location of the intrusion and (partially) the Fontanelas seamount.

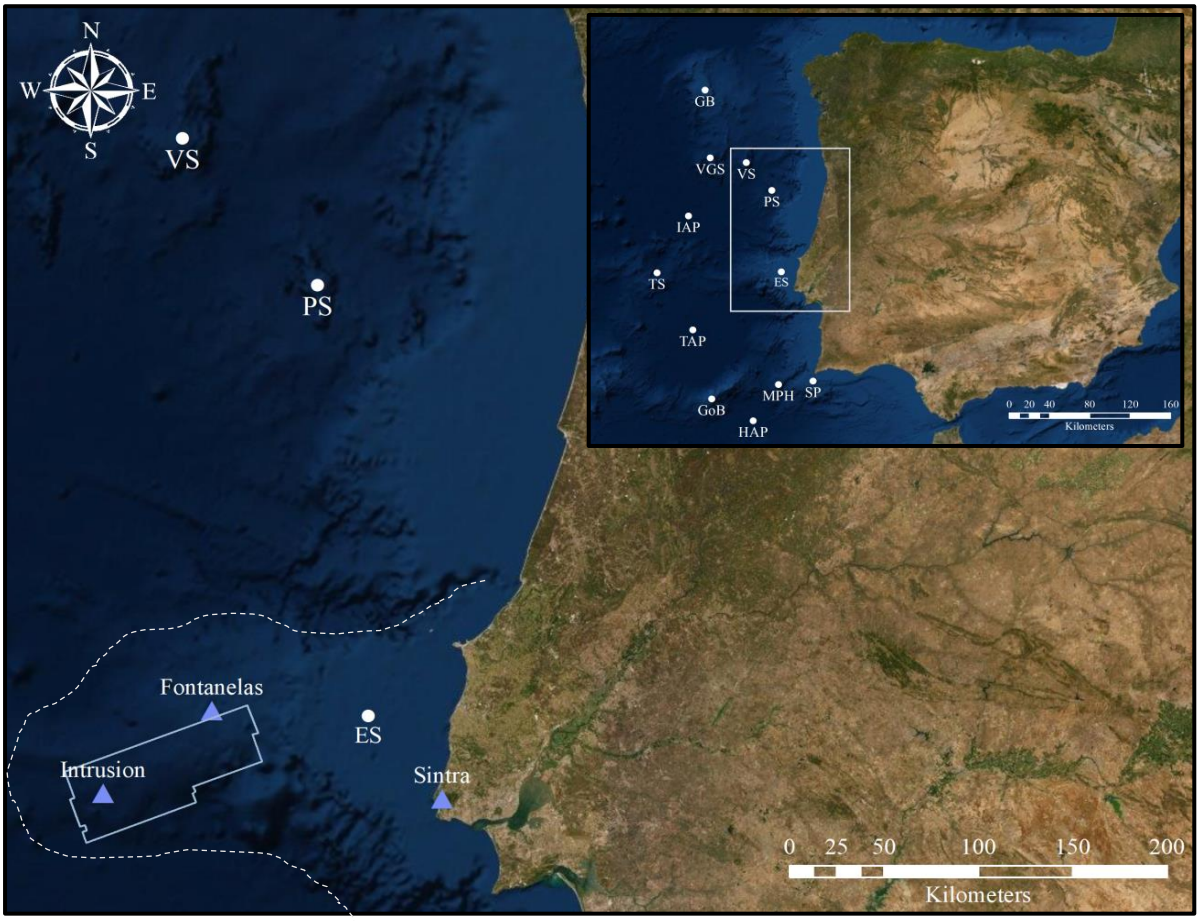

Figure 1.4. Geographical setting of the study area. The SW polygon represents the area of 3D seismic survey, which also includes the location of the intrusion and (partially) the Fontanelas volcano. The dashed white line represents the approximate outline of the Estremadura Spur. GB = Galicia Bank, VGS = Vasco da Gama Seamount, VS = Vigo Seamount, PS = Porto Seamount, IAP = Iberia Abyssal Plain, TS = Tore Seamount, ES = Estremadura Spur, TAP = Tagus Abyssal Plain, GoB = Gorringe Bank, HAP = Horseshoe Abyssal Plain, MPH = Marquês de Pombal High and SP = Sagres Plateau.

1.5. Objectives

The purpose of this study is to characterize the geometry and nature of the two major magmatic features on the Estremadura Spur (Figure 1.4), namely the Fontanelas volcano and the southwest intrusion, based on gravity and magnetic data modelling, supported and constrained by 3D seismic data. This thesis also intends to correlate this intrusion and the Late Cretaceous post-rift magmatic event, based on the seismic data evidence and the similarities between onshore and offshore analogues on the West Iberian Margin.

Considering the goals, it is possible to define a set of questions related to this study:

- What is the geometry and magmatic nature of the intrusion?
- Is it possible to correlate this intrusion with other magmatic events onshore/offshore the margin?
- Is the magmatism, along the West Iberia passive margin, more widespread than initially anticipated?
- What are the implications of magmatism for the evolution of the West Iberian margin?

1.6. Thesis outline

The work developed during this research was organized into seven chapters, in order to fully address the questions referred in the previous section. Under the framework of this thesis, the preliminary analysis and results were presented in the EGU General Assembly 2019[1].

Chapter 1, in which this section is included, introduces the reader to the main themes developed in this study, including the fundamental aspects associated with the geological context of the continental margins and the data and methodology applied in this work.

Chapter 2 focuses on the major geological events that occurred in the Iberian margin over time, including the description of the main lithostratigraphic units, geodynamics and tectonic evolution. It is also highlighted the most important magmatic events that occurred in the region, focusing on the Late Cretaceous cycle.

Chapter 3 provides a description and acquisition conditions of the different datasets used in this study, which include bathymetry and potential field data (2D) as well as seismic data (3D). It is also described the theoretical principles of the 2D modelling theory.

Chapter 4 introduce an initial data analysis, through the application of several signal enhancement techniques, addressing a theoretical overview of the potential field data and some necessary corrections.

Chapter 5 presents the results of the 2.5D modelling method, describing and justifying the density and susceptibility values obtained in both gravity and magnetic model.

In Chapter 6 an integrated discussion of the results is presented, including the nature and geometry of the magmatic targets, according to the density and magnetic susceptibility values obtained through the modelling process in chapter 5.

Chapter 7 presents the conclusions and some indications for future work concerning the topics developed throughout the thesis.

[1] Escada, C., Santos, F., Represas, P., Pereira, R., Mata, J., 2019. Post-rift magmatism on the central West Iberian Margin : New evidence from magnetic and gravimetric data inversion in the Estremadura Spur, in: EGU General Assembly. https://doi.org/10.1144/jgs2016-050

Chapter 2: Geological setting

2.1.West Iberian Margin

The evolution of the West Iberian Margin (WIM) begins during the Paleozoic, with the convergence and collision of the two major continents (Laurasia and Gondwana), which led to the formation of the supercontinent Pangea and gave rise to the Variscan Orogenic Belt (often referred as Hesperic Massif, Pinheiro et al., 1996). This accreted massif hosts Precambrian and Paleozoic rocks, which were intruded by large batholiths during and after the Variscan continent-continent collision (Pinheiro et al., 1996).

The pre-Mesozoic tectonic inheritance is associated with the basement of the WIM, a part of the Ibero-Armorican arc, which constitutes the main macrostructure in Western Europe formed during the Variscan Orogeny, namely from Middle Devonian to Carboniferous (Dias and Ribeiro, 1995). By the end of the Paleozoic, Iberia was part of Pangea, which comprised almost all the continental masses in one single super-continent (Terrinha et al., 2019). In Permian times, Late Variscan faulting developed after cratonization of the Variscan Orogen (Terrinha et al., 2019).

On the West Iberian Margin, the Mesozoic evolution was strongly controlled by the opening of the North and Central Atlantic Ocean and the westernmost segment of the Tethys, initiated by mid to late Triassic. The re-activation of inherited Late Variscan tectonic structures played an important role in the formation of sedimentary basins, both onshore and offshore (e.g. Pinheiro et al., 1996). The reactivated strike-slip faults, oriented ENE-WSW and SW, were the main extensional faults, controlling the multi-phased rifting in West Iberia (Alves et al., 2009; Pereira et al., 2017; Terrinha et al., 2019).

The Mesozoic evolution on the WIM comprises four distinct rifting episodes that control the geometry and deposition of the different basins (e.g. Pereira and Alves, 2011): 1) Late Triassic (Norian) to Early Jurassic (Hettangian), 2) Early Jurassic (Sinemurian) to late Middle Jurassic, 3) Late Jurassic (Oxfordian) to earliest Cretaceous and 4) Early Cretaceous (Berriasian-Aptian). These rifting events led to the deposition of distinct megasequences, exposed in outcrops and observed on seismic reflection data, both onshore and offshore (e.g. Alves et al., 2009; Pereira and Alves, 2011; Rasmussen et al., 1998).

West Iberia is a North striking passive margin with multiple Mesozoic basins (Figure 2.1; Alves et al., 2009). Two first-order transcurrent zones, the Messejana-Plasencia Fault and the Nazaré Fault, controlled the Mesozoic rifting phases (Groupe Galice, 1979), and subdivide the WIM into three distinct segments (e.g. Alves et al., 2009; Pereira et al., 2017), namely: 1) at the South, the Algarve and Cadiz Basins, 2) in SW Iberia, the Alentejo Basin and 3) in NW Iberia, the Peniche, Lusitanian, Porto and Galicia Basins (Figure 2.1). Additionally, the Aveiro and Tagus strike-slip faults also play a significant role in margin segmentation and controlling the deposition of individual sub-basins (e.g. Alves et al., 2009).

In the Late Triassic, the continental extensional regime led to the initial rifting of Iberia and the onset of the first rifting episode (e.g. Pereira and Alves, 2011). Iberia was located at the triple junction of the Variscan suture zone, between Laurasia, Gondwana and the western end of the Tethys Ocean, creating the necessary conditions for crustal stretching and thinning around Iberia (Terrinha et al., 2019). This geodynamic context allowed the formation of intra-continental rifts, and its associated sedimentary basins, on the SW and West Iberia. This Late Triassic to earliest Jurassic rifting event is

characterised by the deposition of continental red beds and evaporites (Figure 2.2; Azerêdo et al., 2003).

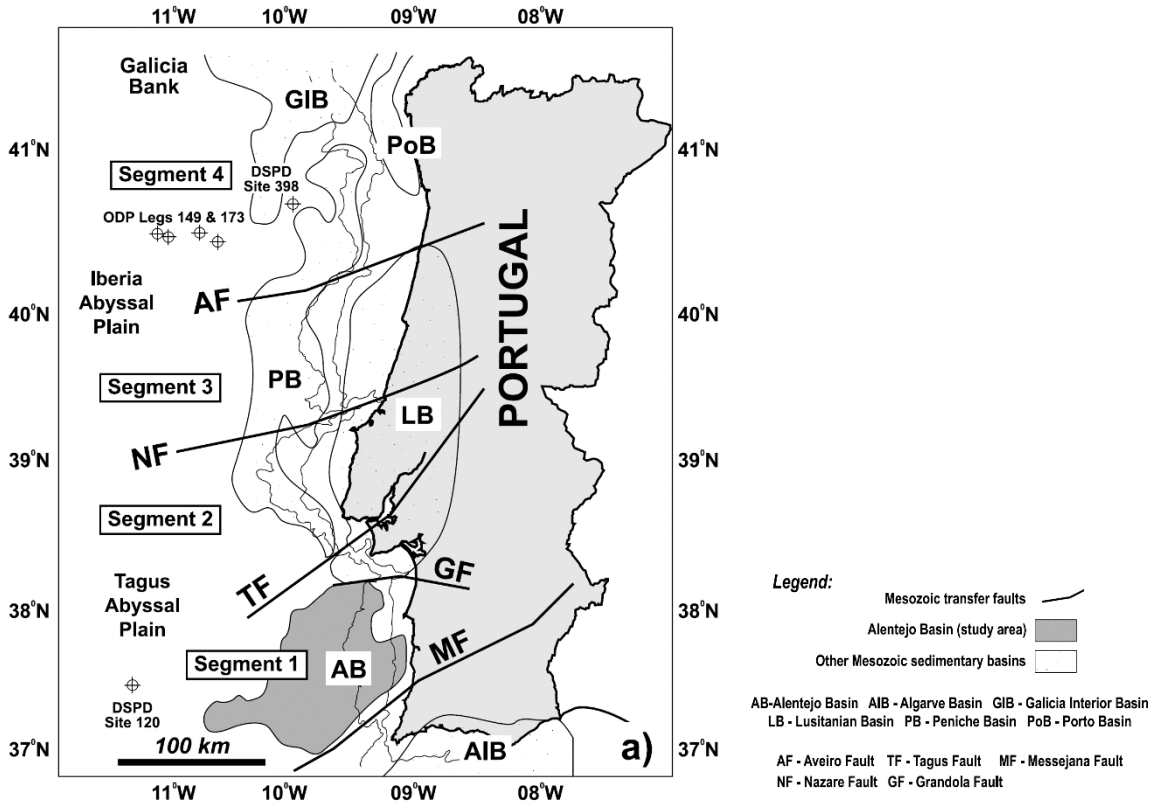

Figure 2.1. Map of the West Iberia continental margin showing the Mesozoic basins and the major transfer faults. From: Alves et al. (2009).

In the Jurassic, the beginning of the sinistral oblique movement of West Africa with respect to Eurasia triggered the propagation of the Tethys Ocean towards the North Atlantic rifts (Terrinha et al., 2019). The onset of the second rift phase is marked by widespread magmatism on the Central Atlantic Magmatic Province (CAMP; Martins et al., 2008) and subsequent formation of a dominantly carbonate platform that records the progressive increase of marine conditions throughout the WIM, with the deposition of carbonated lithotypes, including limestones and dolomites (Figure 2.2; Azerêdo et al., 2003).

From the Late Triassic to the latest Jurassic-Early Cretaceous, SW Iberia evolved as an hyper-extended continental rift margin, until the generation of oceanic crust in the Tagus Abyssal Plain, after continental breakup (Manatschal and Bernoulli, 1998; Mauffret et al., 1989).

The oceanic spreading was diachronous throughout the Iberian margin, with the first event of continental breakup on the SWIM likely by the end of the Jurassic (Figure 2.3a; Mauffret et al., 1989; Pereira and Alves, 2011), followed by formation of oceanic crust and continental mantle exhumation of the hyper-extended crust in NW Iberia from Barremian to Aptian (ca. 128 to 110 Ma; Wilson et al., 2001), and ultimately, in the northern Iberia during the Late Cretaceous.

The opening of the Bay of Biscay started between 130-118 Ma and ended 80 Ma ago, as the result of the continued movement of the oceanic spreading towards the north, giving rise to SE motion and anti-clockwise 35º rotation of Iberia (Miranda et al., 2009). After complete breakup (Aptian-Albian, 112 Ma; Figure 2.3b), West Iberia underwent a period of relative tectonic quiescence in the Late

Cretaceous (Figure 2.3c) and progressive development of the drift phase (e.g. Pereira and Alves, 2012).

The Cretaceous sedimentary sequence records syn- and post-rift tectonic environments (e.g. Groupe Galice, 1979), despite the relative sea-level variations influence in the facies distribution, the Cretaceous is characterized by a generalized low rate of subsidence and deposition. (Proença Cunha and Pena dos Reis, 1995). In the Aptian-Albian boundary there was an expansion of the sedimentation area accompanied with the deposition of coarse siliciclastic sediments, followed by a later development of marine carbonates influenced by the long-term Albian-Cenomanian transgression (Proença Cunha and Pena dos Reis, 1995).

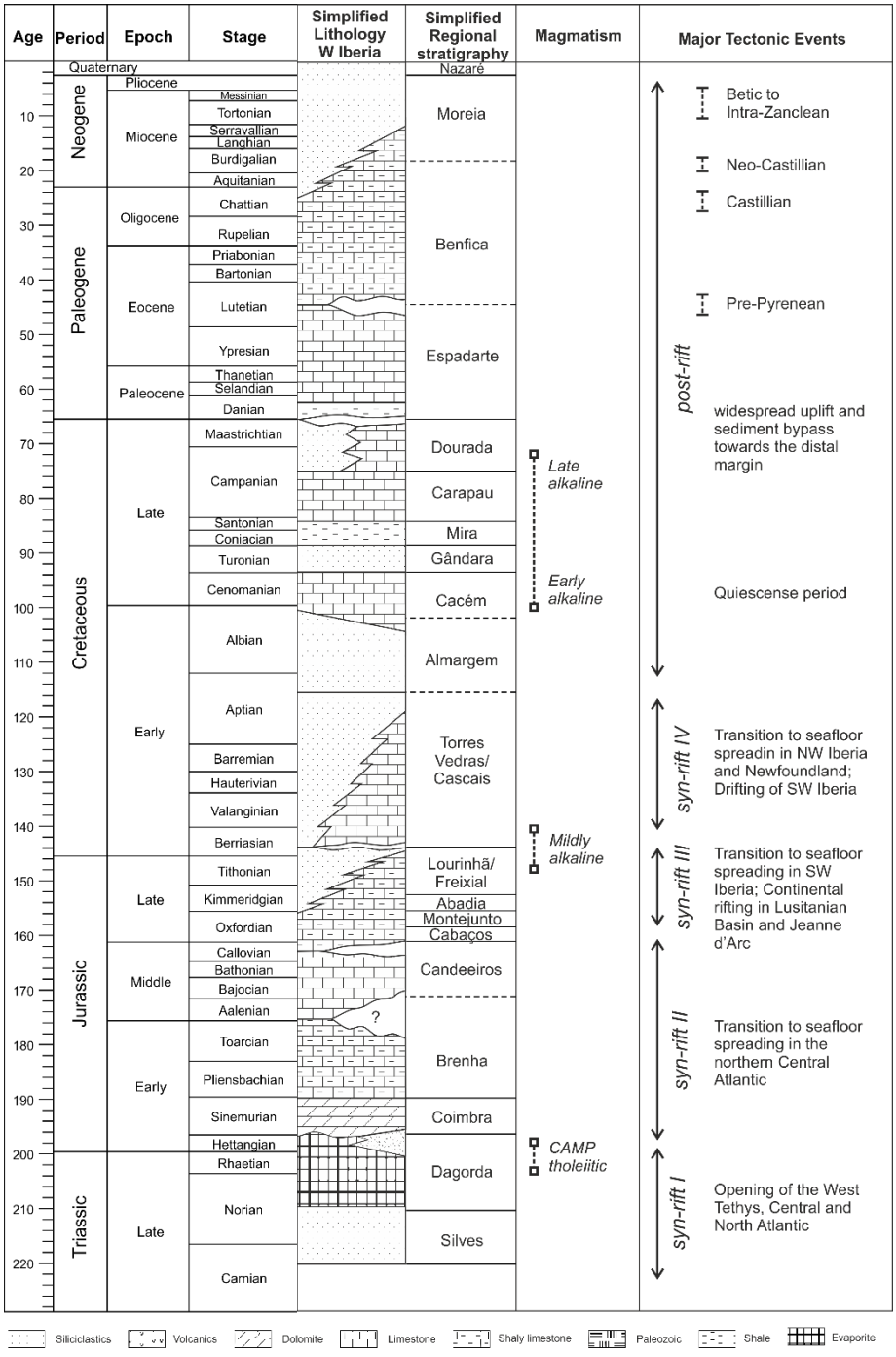

Figure 2.2. Lithostratigraphic record, magmatic episodes and major tectonic events of the West Iberian margin. Adapted from Pereira et al. (2017).

The beginning of the late Campanian, in the Lusitanian Basin, was marked by diapiric events and reactivation of the Nazaré-Lousã fault. Subsequently, the upper Campanian-Maastrichtian is recorded by the deposition of quartz sandstones grading to sandy dolostones and, occasionally, sandy limestones (Proença Cunha and Pena dos Reis, 1995).

The Cenozoic was marked by multiple compressional and tectonic inversion episodes (the Pyrenean and Alpine orogenies; Pinheiro et al., 1996). The convergence between Africa and Eurasia plates began in the Late Cretaceous, leading to collision 35 Ma ago. This compressive post-rift tectonic phase strongly affected the Tagus Abyssal Plain and the Estremadura Spur during the Miocene (e.g. Mougenot, 1989).

The two main compressional episodes, which affected the West Iberia Margin since the rifting ended, occurred during the Eocene and Miocene (Figure 2.3d), although inversion still occurs in recent periods (e.g. Duarte et al., 2013).

Figure 2.3. Paleogeographic reconstruction of the North Atlantic realm during the a) Late Jurassic (150 Ma), b) Aptian-Albian boundary (112 Ma), c) Late Cretaceous (70 Ma) and d) Miocene (13 Ma). From Hay et al. (1999).

The effects of this inversion include folding and reactivation of old Variscan structures, some of which had been reactivated during the rifting episodes (e.g. Pinheiro et al., 1996; Pereira and Alves, 2011).

The onset of rapid collision and subduction between the Iberia, Eurasia and Africa plates resulted in the tectonic inversion of structures formed during the Mesozoic extensional periods (Miranda et al., 2009).

The building of the Pyrenean and Betic orogens and the internal deformation associated with the Iberia microplate controlled the formation and evolution of the Tertiary basins (Proença Cunha and Pena dos Reis, 1995). Extensional structures dominated the western Iberian passive margin, during the Paleogene to middle Tortonian times, until the late Tortonian-Quaternary compressional events (Betic orogeny) leading to the structural inversion of the Lusitanian basin (Proença Cunha and Pena dos Reis, 1995).

In Pliocene times the compressive phase and consequent tectonic inversion are related to the counter-clockwise rotation of Africa with respect to Iberia, changing from frontal to oblique collision (Neres et al., 2018).

2.2. Late Cretaceous magmatism

The West Iberian Margin was the locus of several magmatic cycles during the Mesozoic, occurring both in the Hesperic Massif (Central Iberian Zone) and in the Lusitanian Basin (Pinheiro et al., 1996). However, magmatism is mainly located to the south sector of the Nazaré Fault (e.g. Martins et al., 2008; Mata et al., 2015; Miranda et al., 2009; Pereira et al., 2017). The Mesozoic magmatic activity in the WIM is scattered and the volume of magma produced in these occurrences is insignificant compared with the volcanism that preceded and accompanied continental rifting (Pinheiro et al., 1996) and contrasting with other magma-poor margins (Franke, 2012).

During the Mesozoic, the WIM was punctuated by three phases of magmatic activity (e.g. Martins et al., 2008; Mata et al., 2015; Miranda et al., 2009): 1) Triassic- Jurassic tholeiitic cycle (200-198 Ma), 2) Jurassic-Cretaceous mildly alkaline cycle (148-140 Ma) and 3) Late Cretaceous alkaline cycle (94-69 Ma). The two first magmatic phases are associated with the Late Triassic and Late Jurassic rifting events, respectively, thus being syn-rift magmatic events, whereas the Late Cretaceous magmatic event occurred in a post-rift tectonic setting (Figure 2.2; Pinheiro et al., 1996).

The first Mesozoic magmatic event is represented in the SW Iberia and is characterized by tholeiitic basalts, which are considered as part of the Central Atlantic Magmatic Province, as well as dolerite-basaltic Messejana dykes with Late Triassic ages, related to the last phases of the Variscan orogeny in Iberia and the initial extensional phases of Pangea (e.g. Martins et al., 2008; Pinheiro et al., 1996; Verati et al., 2007).

The Late Jurassic–Early Cretaceous magmatic cycle was contemporaneous with a period of significant extension and lithospheric thinning in West Iberia (e.g. Pereira et al., 2017; Wilson, 1988). Evidence of magmatic features occurs mainly in the Lusitanian Basin, close to the onshore expression of the Nazaré Fault Zone, as transitional (mildly alkaline) dolerite sills and dykes associated to halokynesis (Mata et al., 2015). Ages from these intrusive rocks date the event at 148-140 Ma, evidencing a period of magmatic activity in response to a renewed rift phase.

The most voluminous and widespread magmatic event of the WIM occurred in the Late Cretaceous (third magmatic cycle) and is subdivided into two alkaline pulses that reveal the role of sub-

lithospheric mantle sourcing, which contrast with more sub-continental magmas from the previous magmatic cycles (Martins et al., 2010). The first pulse, occurred between 94-88 Ma, during the opening of the Bay of Biscay and consequent rotation of Iberia, mainly as sills, such as the Foz da Fonte (Neres et al., 2014, 2012) and Paço de Ilhas (Neres et al., 2012), around the Lisbon area. The second pulse (75-72 Ma) occurred in the southernmost part of Portugal (Algarve Basin) extending to Lisbon, and include both intrusive, such as the Sintra (Terrinha et al., 2017, 2003), Sines (Ribeiro et al., 2013) and Monchique massifs, and extrusive complexes. The latter event is coeval with the first pulses of tectonic inversion due to the onset of rapid convergence between the African and Iberian plates (Miranda et al., 2009).(Meyer et al., 2017)

Evidence of these two pulses includes (Grange et al., 2010; Martins et al., 2010; Miranda et al., 2009): 1) sills and dykes around Lisbon region and 2) the Lisbon Volcanic Complex (72.6 ± 3.1 Ma), the Sintra (~ 79 Ma), Sines (75.4 ± 0.6 Ma) and Monchique Igneous Massifs (72.7 ± 2.7 Ma). Neres et al. (2018), recently described an intrusion beneath the Guadalquivir-Portimão Banks emplaced in the lower and upper crust of the Algarve Basin. Additional magmatism also occur on the Madeira-Tore Rise (Merle et al., 2018, 2009), although in a distinct geodynamic setting than those observed onshore West Iberia (Pereira et al., 2017).

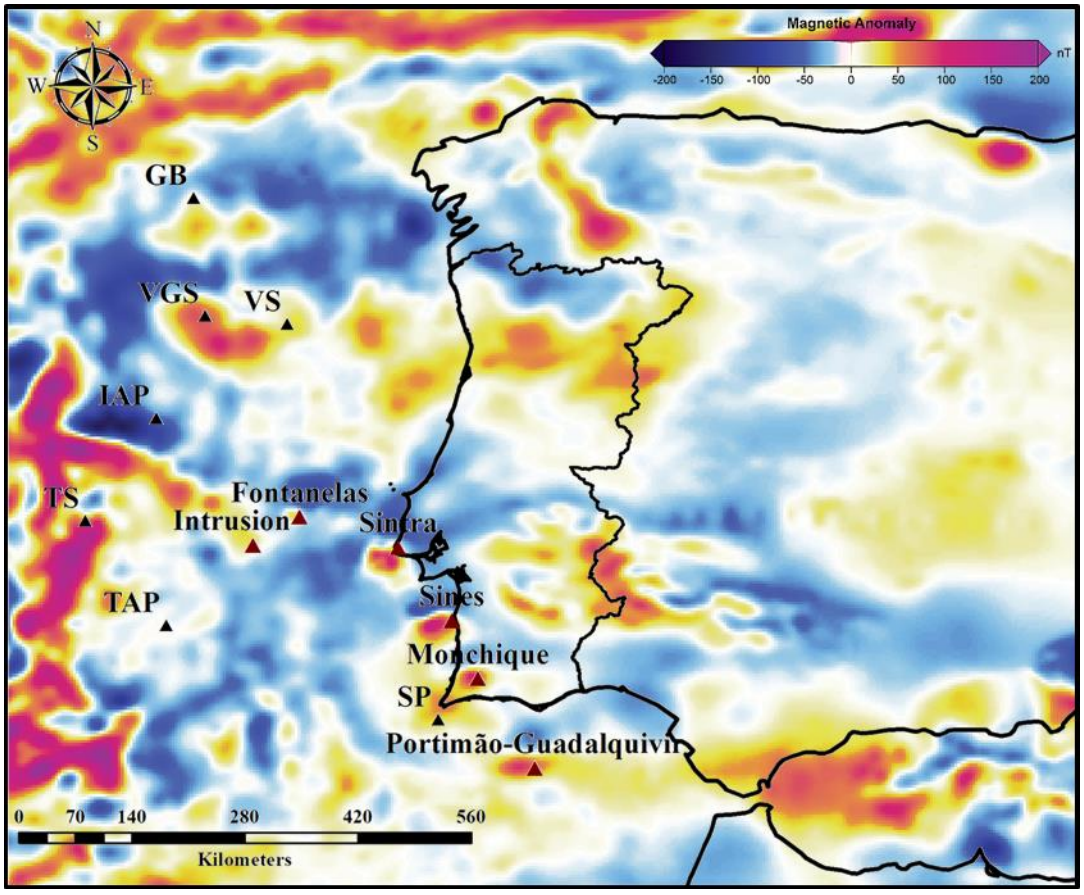

Figure 2.4. Regional magnetic anomaly map (Meyer et al., 2017). The onshore magnetic anomalies correspond to the Sintra-Sines-Monchique massifs, whereas the offshore magnetic anomalies are the Portimão-Guadalquivir Banks, the Fontanelas Seamount and the intrusion. The two latter magnetic anomalies are the main targets of this study. The bathymetry features are GB = Galicia Bank, VGS = Vasco da Gama Seamount, VS = Vigo Seamount, IAP = Iberia Abyssal Plain, TS = Tore Seamount, TAP = Tagus Abyssal Plain and SP = Sagres Plateau.

The Sintra-Sines-Monchique complexes (Figure 2.4) are the most enigmatic events of the Late Cretaceous magmatic episode in the West Iberia Margin. These three igneous alkaline complexes intersect in different crustal contexts (Neres et al., 2018): the Monchique massif, is emplaced within unrifted basement, whereas the Sintra and Sines complexes are emplaced within the Lusitanian and Alentejo rift basins, respectively, developed during the opening of the Atlantic Ocean (Miranda et al., 2009).

The age distribution and the alignment of the Sintra, Sines and Monchique massifs (Figure 2.4) of West Iberia Cretaceous magmatism, led several authors to speculate about its origin, for example, Miranda et al. (2009) suggest the emplacement of deeply anchored mantle plumes and actively upwelling interacting with mid-ocean ridges and other major structures.

The last Mesozoic magmatic phase took place in a post-rift setting, 30 Ma after the beginning of oceanization in the Tagus Abyssal Plain, during the 35º anti-clockwise rotation of Iberia, the initiation of the alpine compression (partially coeval with the Pyrenean continental collision in Northern Iberia) and the onset of tectonic inversion on the Mesozoic basin (Miranda et al., 2009).

The target magmatic features (Figure 2.4) in this study are within the Estremadura Spur, an E-W underwater promontory located between Cabo Carvoeiro and Cabo da Roca (Badagola et al., 2006). This important physiographic feature of the West Iberia Margin stands out from the continental margin and is interpreted as an uplifted block of continental crust up to 100 km wide (Pereira et al., 2017). The Estremadura Spur and the Tore Seamounts separate the Iberia Abyssal Plain to the north and the Tagus Abyssal Plain to the south. The Nazaré Fault Zone limits the spur to the north and separates two distinct crustal domains (Pereira et al., 2017). Focused deformation on the Estremadura Spur includes folding and reverse faulting, which reveals the tectonic stresses that still prevail until the present (Pereira et al., 2017).

The Estremadura Spur (Figure 1.4) is punctuated with evidence of several intrusive bodies, including a volcano with more than 3000 meters high, the Fontanelas Seamount (Miranda et al., 2009; Pereira et al., 2017; Figure 2.4). According to Miranda et al. (2009), the Fontanelas volcano can be assigned to Late Cretaceous age based on its geochemical signature. Thus, being related to other anomalies of the same age in the region, namely the onshore alkaline magmatic bodies, such as the Sintra (Terrinha et al., 2017, 2003), Sines (Ribeiro et al., 2013) and Monchique massifs, the Foz da Fonte (Neres et al., 2014, 2012) and Paço de Ilhas (Neres et al., 2012) sills and the Lisbon Volcanic Complex.

Chapter 3: Data and methodology

The characterization of the magmatic under study (Fontanelas Seamount and the intrusion located SW from the latter, Figure 1.4) was accomplished through potential field and seismic data available on the region. The seismic data is very important for this type of studies because it provides a strong structural constraint for the potential field data modelling, thus reducing non-unicity issues inherent to these methods. Despite the processing and interpretation of the seismic data is not included in the scope of this study.

The datasets were acquired in two separate campaigns offshore Portugal with different acquisition conditions that must be addressed separately. The potential field data were acquired during a 2D seismic marine campaign in 2008, whereas the seismic data were acquired in a 3D marine campaign in 2010. In both marine campaigns, several datasets were acquired, including seismic, potential field data (gravity and magnetic) and bathymetry. The reports on the data processing were prepared for Petrobras and the acquisition contractor was Austin Exploration Inc.

Concerning the methodology, in this section more emphasis will be given to the 2D modelling theory, while the following will focus on signal enhancement techniques, including a brief explanation about some corrections applied to the potential field data.

The coordinate system chosen to georeferenced the bathymetry and potential field data was the ED50 Portugal Datum, International Spheroid on an UTM projection. All grids have 1500 meters grid spacing and the interpolation was made using the kriging technique.

3.1. Bathymetry and potential field dataset

The 2008 2D campaign had a total survey kilometrage of 9498: the magnetic kilometrage was 9397 whereas the gravity kilometrage was 9498. The distance between sites (along the lines) is, approximately, 4 meters in the x-direction (latitude) and 25 meters in the y-direction (longitude), while the distance between lines is, on average, 3 km. However, the distances between the southern lines (over the Estremadura Spur) are much smaller than the distance between the lines in the northern region (Figure 3.1).

The gravity and magnetic data were acquired during a seismic campaign, in which the main goal was the acquisition of seismic data. Thus, considering that acquisition conditions (such as spacing and size of the acquisition area) have not been defined taking into account a study of potential field data the processing and analysis of the data may be more limited.

3.1.1. Bathymetry data

The bathymetry data were acquired with a hydrographic echo-sounder (Simrad EA500) and stored as negative numbers (Figure 3.1), where the zero corresponds to the sea level. Some bathymetry values are interpolated due to the deep water setting over which the survey was undertaken, and the (presumed) inability of the fathometer[2] to achieve such depths. The presence of these values within the

[2] Fathom (nautical length measurement used for depth) + meter: depth finder that uses sound waves to determine the depth of water.

bathymetry dataset prevented a network adjustment procedure to be accomplished. Despite this, the bathymetric data did not pose any problems and a good quality grid was produced (Figure 3.1). An offset correction was applied to the bathymetric data as the fathometer was located 6.86 meters ahead of the Navigation Reference Point (NPR).

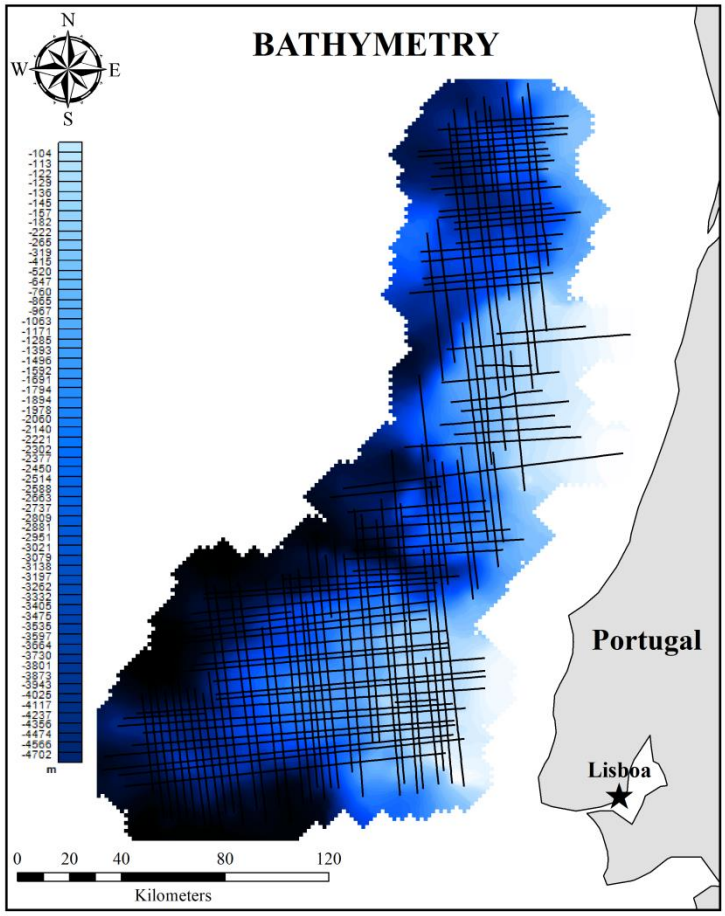

Figure 3.1. Bathymetric map of the region, with the survey acquisition lines.

3.1.2. Gravity data

The sensor used to measure the gravity data was a LaCoste & Romberg 'S' Gravity Sensor (S-28). The counter units of the gravity data were converted to mGal using the S-28 calibration table. As in bathymetry data, an offset correction properly made, since the gravity meter was located 6.1 meters ahead of the NRP.

Marine data are measured aboard of a ship, for this reason it is necessary to apply the Eötvös correction in order to cancel the effect of the moving vehicle, since it can compromise the precision of the entire data (Thompson and LaCoste, 1960). In this case, the Eötvös correction was computed using position information from each navigation file. The values were filtered with a multiple-stage RC (resistor-capacitor) filter totalizing 300 seconds in order to match the filter applied to the gravity data during acquisition. Then, the raw gravity and Eötvös correction profiles were inspected for correlation with Eötvös events in both amplitude and time. The Eötvös correction was applied to the gravity values by a moving window cross-correlating algorithm allowing small lateral movements to compensate for phase imprecision and limited local scale changes, based on a minimum curvature principal. Finally, Eötvös-corrected gravity was advanced by the appropriate time interval (300 seconds) to compensate for the internal filter lag.

A latitude correction was also applied using the 1967 Gravity Formula. This correction is routinely applied to gravity data to compensate for the effect of the Earth's mass and rotation movement, which results in the increase of the gravitational field from the equator towards the poles. The data were tied to the IGSN71 network (from the Instituto Geográfico Português gravity station located at the Largo do Museu de Artilharia, Lisbon) using a Base Constant value of 972633.4 mGal.

The Bouguer correction was computed using a three-dimensional algorithm and the bathymetry dataset. Several Bouguer corrected gravity datasets were supplied for this study, computed with different correction densities (2.0, 2.1, 2.2, 2.3 and 2.4 g/cm^3). In each case, the Bouguer gravity was calculated summing free air gravity and the Bouguer correction. In the following chapter, the Bouguer correction will be addressed with more detail.

A network adjustment procedure was carried out to minimize mis-ties between all survey lines. This is a multi-stage operation that consists of a combination of DC shifts, gradient limited datum tilts (to replicate long-wavelength effects, such as tidal effects) and gradient limited datum bends (to replicate shorter-wavelength effects, such as swell in gravity or diurnal effects in magnetics).

The gravity data was subjected to a statistical quality assessment, by analysing the standard deviation of amplitudes with wavelengths shorter than 4.0 km. This procedure was applied line by line using a high-pass cosine tapered filter to Bouguer corrected data. The method relies on the existence of a continuous spectrum of noise throughout the dataset.

The gravity signal presents short-wavelength content associated with geological information plus the system noise, which may have a number of causes. In practice, before filtering, the latter term tends to dominate the shorter-wavelength part of the spectrum. Additionally, the geological content is broadly constant over the survey area, affecting multiple lines in an approximately equal way. Thus, a statistical analysis of amplitudes will allow lines to be ranked according to data quality as defined by the standard deviation of the data around the zero level. Following this statistical analysis of the gravity dataset, quality dependent filters were applied to the data, based on the standard deviation values generated from wavelengths shorter than 4.0 km: the better the line, the smaller is the standard deviation value and the shorter is the filters wavelength.

To assist in the removal of non-geological signal a depth-dependent variable cut-off filter was applied to the data. This was designed to remove short-wavelength signal apparently derived from sources in the water column (noise), which cannot, therefore, be of geological origin. In this case, the smaller the water depth, the shorter is the filter cut-off.

3.1.3. Magnetic data

The sensor used for the magnetic measurements was the SeaSPY marine magnetometer, which was towed behind the vessel. To compensate for the offset from the NRP, an offset correction from about 236.5 meters was applied. The International Geomagnetic Reference Field (IGRF 2005 model) updated to the epoch of the survey was subtracted from the offset corrected magnetic data.

There were serious time errors within the magnetic dataset, and it was necessary to perform several time corrections prior to merging the navigation data. These errors had an intermittent nature and affected more lines than initially known during the acquisition. However, if a problem was proven or suspected (due to poor levelling statistics) the line was not used.

The diurnal correction was not applied in the initial processing stage because, at the time, it was not possible to obtain diurnal correction data. However, magnetic observatory readings were obtained

from the observatory at Coimbra, Portugal. These values were subsequently subtracted from the IGRF corrected magnetic data.

Such as in gravity data, to assist in removing non-geological signal, a depth-dependent variable cut-off was applied, as well as a low pass cosine taper filter and a network adjustment.

3.2. Seismic data

The 3D seismic survey is located WNW of Lisbon, Portugal (polygon in Figure 1.4). The contractor was CGG Veritas and the vessel was the Geowave Endeavour. The survey was designed with 2096 full fold km^2 and ENE-WSW line direction. The shooting plan consists of two swaths[3].

The survey map is displayed in Figure 3.2. The distance between readings (inside the lines) is 2.67 meters in the x-direction (latitude) and 4.86 meters in the y-direction (longitude), while the distance between lines varies between 1 and 2 km.

Raw seismic data were recorded on the Sercel SEAL 24-bit seismic data acquisition system. The seismic energy source was towed at a depth of 7.0 (± 0.5) meters. The source fire-times were controlled and monitored by the Gunlink Marine Seismic Source Controller and the source air pressure was specified as 2000 (± 5%) psi, having been achieved for all valid shots.

The quality of the acquired seismic and navigation data were continuously monitored, both during acquisition ('online') and afterwards ('offline'). The online display continuously showed recorded data from two streamers (it cycles through all streamers and all channels) where, in addition to RMS noise levels assessment, a visual monitoring of irregularities was made.

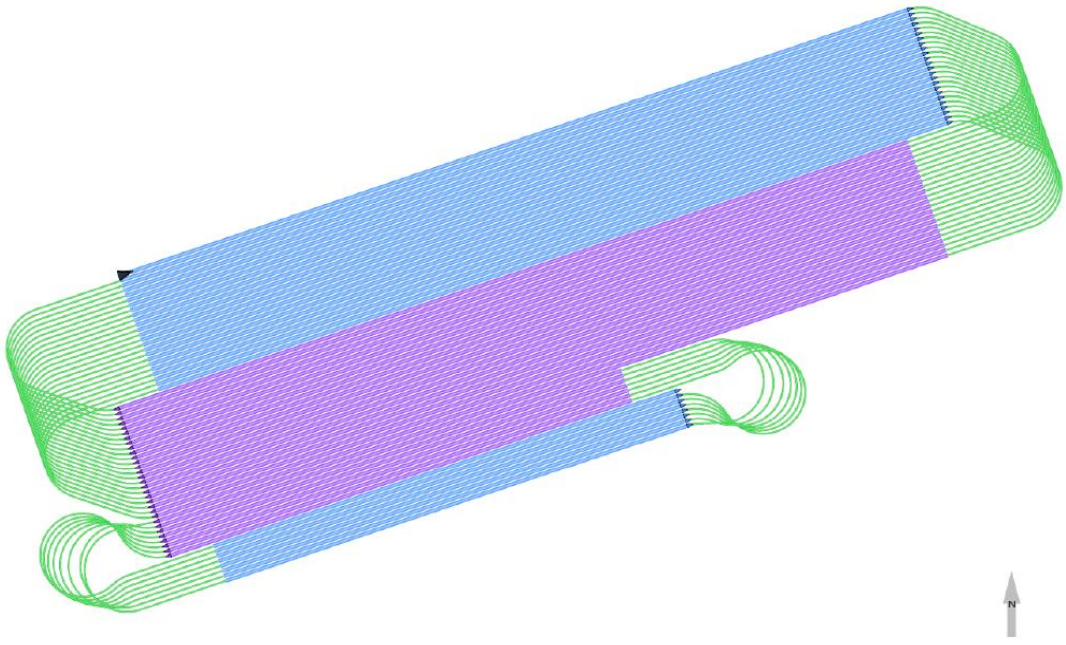

Figure 3.2. Survey design map of 3D seismic data acquisition, with the acquisition swaths indicated by blue and purple areas.

[3] The swath shooting is a common type of survey design in 3D seismic data acquisition. In swat shooting, the receiver lines are fixed and all the shots related to the swaths are recorded with the same set of fixed receiver lines (Singh et al., 2010).

Meanwhile, the vessel was continuously steered for maximum coverage and all navigational aids were monitored. The data processing and navigation analyse were performed in offline quality control.

The processing and interpretation of the seismic profiles is outside of the scope of this study. All the seismic profiles used in this thesis were already converted to depth and had applied a Pre-Stack Depth Migration (PSDM). In this case, the seismic profiles were interpreted by Ricardo Pereira[4].

3.3. Methodology

The geophysical study consists of an initial regional analysis of the potential field datasets, involving data enhancement techniques, followed by qualitative interpretation of the resulting maps and, finally, gravity and magnetic 2D forward modelling.

In data enhancement technique the anomaly is analysed and processed with the aim to enhance certain source's characteristics, in order to facilitate the interpretation (Blakely, 1995). The ones used in this work will be addressed in the next chapter. The forward method begins with the development of an initial model based on the available prior information. The response produced by the model is calculated and compared with the observed data. To improve the fit between both the calculated and observed anomalies the model parameters need to be adjusted (Blakely, 1995). This three-step iterative process (Figure 3.3) of models response calculation, data comparison and model parameters adjustment is repeated until the calculated and observed data are sufficiently similar (Blakely, 1995), i.e. the fit is acceptable, and the geological model is realistic.

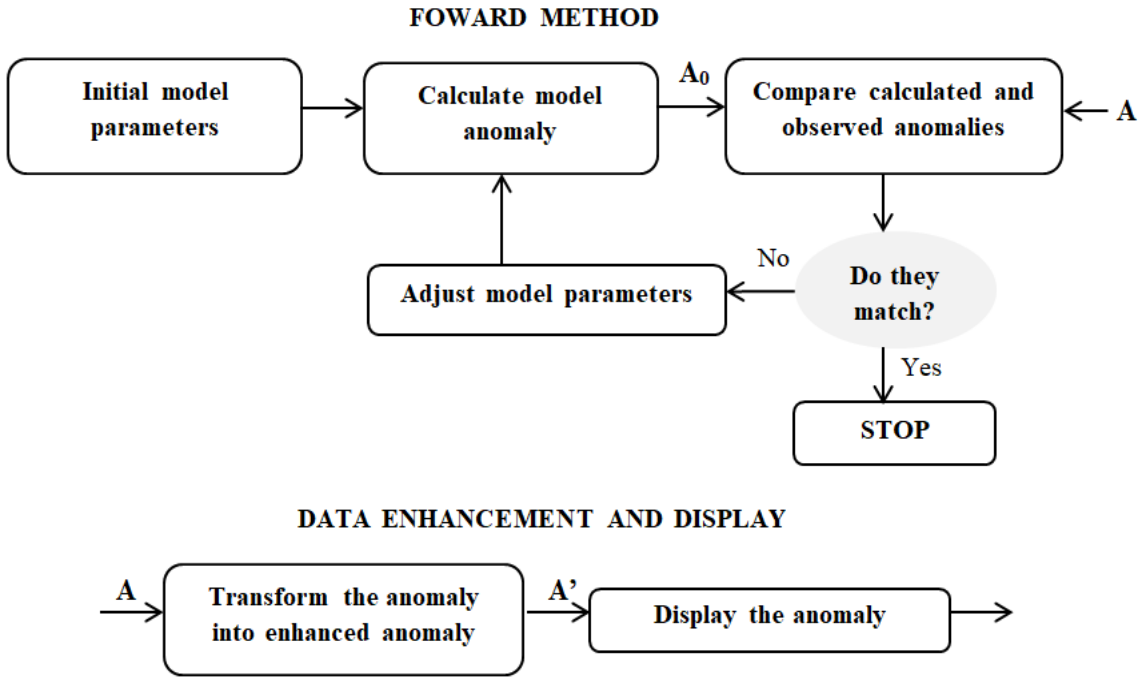

Figure 3.3. Two categories of techniques to interpret potential field data: forward and data enhancement. A is the measured anomaly, A_0 is the calculated anomaly and A' is the transformed measured anomaly. Adapted from Blakely (1995).

[4] Institute Dom Luis (IDL), Faculty of Sciences University of Lisbon (Campo Grande, Portugal); Partex Oil & Gas, R. Ivone Silva 6, 1st floor, 1050-124, Lisbon (Portugal).

3.3.1. Software

Two programmes were used in order to analyse, process and display the geophysical data: Oasis Montaj and ArcMap.

Oasis Montaj was developed by the Geosoft Inc., a company founded in Canada, focused on natural resources exploration and related earth sciences disciplines, providing software for mapping and modelling the Earth's subsurface and subsea. More specifically, Oasis Montaj allows the visualization, analysis and modelling of geophysical data, aiding in its interpretation. In this study, Oasis Montaj was used for data import and gridding. Two extensions of this program were also used: 1) Geophysical Interpretation extension (namely, the MAGMAP geophysical filtering) for an integrated data analyse and enhancement and 2) Geophysical Modelling extension for gravity and magnetic modelling (GM-SYS profile modelling).

ArcMap is a geospatial processing program and the principal module of the ArcGis (geographic information system – GIS, which allows to work with maps and geographic information), developed by ESRI. ArcMap was used to create all the maps and some figures featured in this study.

3.3.2. 2D modelling theory

The 2D modelling process can begin once the magnetic and gravity data are processed and the regional fields have been appropriately removed (Blakely, 1995). The goal of the 2D modelling procedure is to estimate one or more source parameters from observed data, in the case of this work, gravity and magnetic fields (Blakely, 1995). However, unconstrained modelling has usually limited usefulness in the interpretation of gravity and magnetic anomalies due to the non-unique nature of potential field data, considering that several earth models can produce the same gravity/magnetic response. The only way to minimize this obstacle in the modelling process, reducing its ambiguity and obtaining meaningful geological solutions, is to add constraints by incorporating all geological and/or geophysical available information known from the study area (e.g. geologic mapping, borehole, seismic profiles and previous potential field studies).

As mentioned above, the modelling was performed using the Oasis Montaj Geophysical Modelling extension, more specifically the GM-SYS module, which allows the calculation of gravity and magnetic responses from a geological model created by the user. The next section is based on the GM-SYS user's guide from Northwest Geophysical Associates, Inc. (NGA, 2004).

The starting model is constituted by one block of air and another one of crustal rock, an optional topography/bathymetry and gravity or magnetic stations. The GM-SYS models are extended to 30.000 kilometres ("infinity") in the positive and negative x-direction, in order to eliminate edge effects. As a starting point for the initial model, it is possible to specify up to 6 horizons which divide the crustal rock block into horizontal layers. By convention, in GM-SYS models, the Z-axis is positive down, since it represents depth, so positions above sea-level have negative Z-values.

As referred above, the gravity and magnetic profiles are constituted by stations, which represent the locations of the gravity and magnetic measurements and where the gravity and magnetic response of the model will be calculated. These stations should be located in an area with density, magnetization and susceptibility equal to zero (outside of the source material).

The GM-SYS models are composed by blocks with different densities and magnetic properties, defined by surfaces. Each block has constant density and magnetic properties, as well as strike (y-direction) extent. It is possible to associate several parameters to a block: name (e.g. respective

geological unit or lithology), density, susceptibility, the magnitude, declination and inclination of the remanent magnetization and seismic velocity.

A GM-SYS model allows the input of additional external data, such as backdrop images, used as a visual aid to model construction, although it does not affect the computations performed by GM-SYS. In the case of this study, the seismic profile was imported as a backdrop image to constrain the model's structure.

To fit calculated to measured gravity values, GM-SYS allows the use of free air, residual or Bouguer gravity values for the measured values. In land gravity surveys, the calculated values include the contributions of the terrain above sea level. Therefore, if Bouguer anomaly is used to define the measured values, it is necessary to change the density of the "air block" (above the sea level) to the Bouguer correction density to convert the densities of all blocks above sea level to density contrasts relative to the Bouguer correction density. In marine surveys, this does not apply because above the sea level, where there is only air, so the density is zero.

Concerning the magnetic data, in order to properly calculate the magnetic response of the model, it is necessary to add the magnitude and direction of the local magnetic field that prevailed during the survey. Otherwise, the magnetic response cannot be calculated. Instead, the user may choose to apply RTP (reduction to pole), RTE (reduction to equator) to the measured magnetic values. If the used magnetic values are the RTP, the inclination and declination of the Earth's field must be set to 90º and 0º, respectively. For RTE data, the inclination is 0º and the declination is the correspondent value for the survey area and date.

The calculated data must fit the measured data, i.e. the calculated curve and the observed curve need to match within a predetermined error margin. To accomplish this fitting a constant or DC shift must be subtracted from the calculated values. Concerning the gravity data, this is necessary because the calculated value is an absolute calculation for the model extending to "infinity" in the ± x-direction and to some arbitrary depth, by default, 50 km. The gravity observed data is generally corrected for the reference geoid or other local datum. For the observed magnetic data, the IGRF is used, since the calculated values corresponds to the deviation from the ambient earth's field value. The DC shift can be applied in one of three ways: 1) automatically calculated in order to minimize the RMS error, 2) by selecting a point at which the calculated and observed curves will be forced to match or 3) the user may enter a DC Shift explicitly. In the case of this study it was applied an automatically calculation of the DC Shift in both gravity and magnetic modelling.

By default, GM-SYS uses the Gaussian (cgs) system of units for gravity and magnetic data. However, the user may choose to use the International System (SI) or micro-cgs (µcgs) units. In this study, cgs units were used for the gravity data, whereas SI units were used for the magnetic data.

The GM-SYS models are based on a 2.5D, flat-earth approach and may be visualized as a number of tabular prisms with the axes perpendicular to the profile (Figure 3.4). Changes can be made to the model in depth (z-direction) and in the direction of the profile (x-direction, perpendicular to the strike). In the strike direction (y-direction) the geometry is propagated to a very large distance (simulating infinity), though GM-SYS also allows the definition of a non-infinite length for any chosen block.

To calculate the gravity and magnetic responses the method is based on Talwani et al. (1959) and Talwani and Heirtzler (1964). The GM-SYS employ the algorithm described in Won and Bevis (1987), which compute the gravitational acceleration due to a polygon based on the Talwani et al. (1959) method.

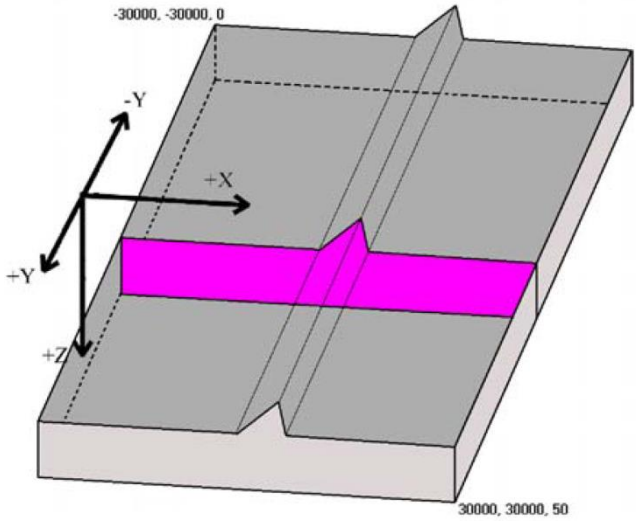

Figure 3.4. GM-SYS 2D model. The pink plane corresponds to the (x,z) plane where the modelling is performed. From: GM-SYS user's guide from Northwest Geophysical Associates, Inc. (NGA, 2004).

Won and Bevis (1987) algorithm is based on the Talwani et al. (1959) expressions for the vertical and horizontal components of the gravitational attraction due to a 2D body of arbitrary shape by approximating it to an *n*-sided polygon. In order to reduce the number of references to trigonometric functions and increase the computational efficiency, Won and Bevis (1987) reformulated these expressions as suggested by Grant and West (1965). To compute the magnetic anomaly caused by a polygon magnetized by an external field, the Poisson's relation was applied to the previous expressions of gravitational acceleration.

In 1959, Talwani, Worzel and Landisman first presented a useful way to approximate geologic structures by replacing its cross-sectional shape with simplified polygons (Blakely, 1995). Their algorithm is the most widely used in computer programs for 2D gravity modelling, being also a very useful technique in potential field interpretation. In this approach, any 2D body of arbitrary shape can be approximated to a polygon and any 2D density distribution can be modelled as an ensemble of juxtaposed constant density polygons (Won and Bevis, 1987).

Won and Bevis (1987) follow Talwani et al. (1959) by setting the station, where the gravity anomaly is calculated, at the origin of the coordinate system (Figure 3.5).

The vertical and horizontal components of the gravity anomaly are expressed as:

$$\Delta g_z = 2G\rho \sum_{i=1}^{n} Z_i \tag{3.1}$$

$$\Delta g_x = 2G\rho \sum_{i=1}^{n} X_i \tag{3.2}$$

Z_i and X_i are line integrals along the i^{th} side of the polygon, G is the gravitational constant and ρ is the density of the polygon.

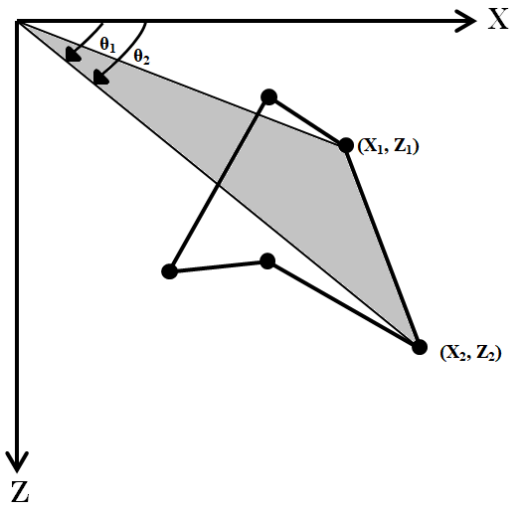

Figure 3.5. Geometrical convention used in the calculous of the x- and z-components expressions of the gravitational acceleration at the origin due to a polygon of density ρ. Adapted from Won and Bevis (1987).

Won and Bevis (1987) follow the Grant and West (1965) approach which reformulates the Z_i expression. Talwani et al. (1959) derive Z_i and X_i expressions making extensive references to trigonometric functions, whereas Grant and West (1965) approach makes more references to the vertices coordinates $\{x_i, z_i\}_{i=1,n}$, thus reducing the number of angular quantities involved in the computation (Won and Bevis, 1987).

To simplify, Won and Bevis (1987) eliminate the subscript i and numbered any two successive vertices (pair of vertices) as 1 and 2 and:

$$Z = A\left[(\theta_1 - \theta_2) + B ln\frac{r_2}{r_1}\right] \tag{3.3}$$

$$X = A\left[-(\theta_1 - \theta_2)B + ln\frac{r_2}{r_1}\right] \tag{3.4}$$

where

$$A = \frac{(x_2 - x_1)(x_1 z_2 - x_2 z_1)}{(x_2 - x_1)^2 + (z_2 - z_1)^2} \tag{3.5}$$

$$B = \frac{z_2 - z_1}{x_2 - x_1} \tag{3.6}$$

$$r_1^2 = x_1^2 + z_1^2 \tag{3.7}$$

$$r_2^2 = x_2^2 + z_2^2 \tag{3.8}$$

$(\theta_1 - \theta_2)$ is obtained by the calculation of θ_1 and θ_2 using the following relation:

$$\theta_j = \tan^{-1}\left(\frac{z_j}{x_j}\right) \text{ for } j = 1,2 \tag{3.9}$$

Won and Bevis (1987) routine only computes the vertical component of the gravity anomaly (Δg_z) but not the horizontal component (Δg_x), because only the first component is measured and modelled.

Talwani and Heirtzler (1964) presented a widely use and computationally effective method for computing the magnetic anomaly due to an infinite polygonal cylinder. Alternatively, Won and Bevis (1987) derive the expressions that define the magnetic anomaly caused by a polygonal cylinder from the previous expressions of the gravity anomaly using the Poisson's relation.

Won and Bevis (1987) assume the cylinder is magnetized exclusively by the earth's magnetic field, thus assuming the existence of induced magnetization and rejecting the presence of remanent magnetization.

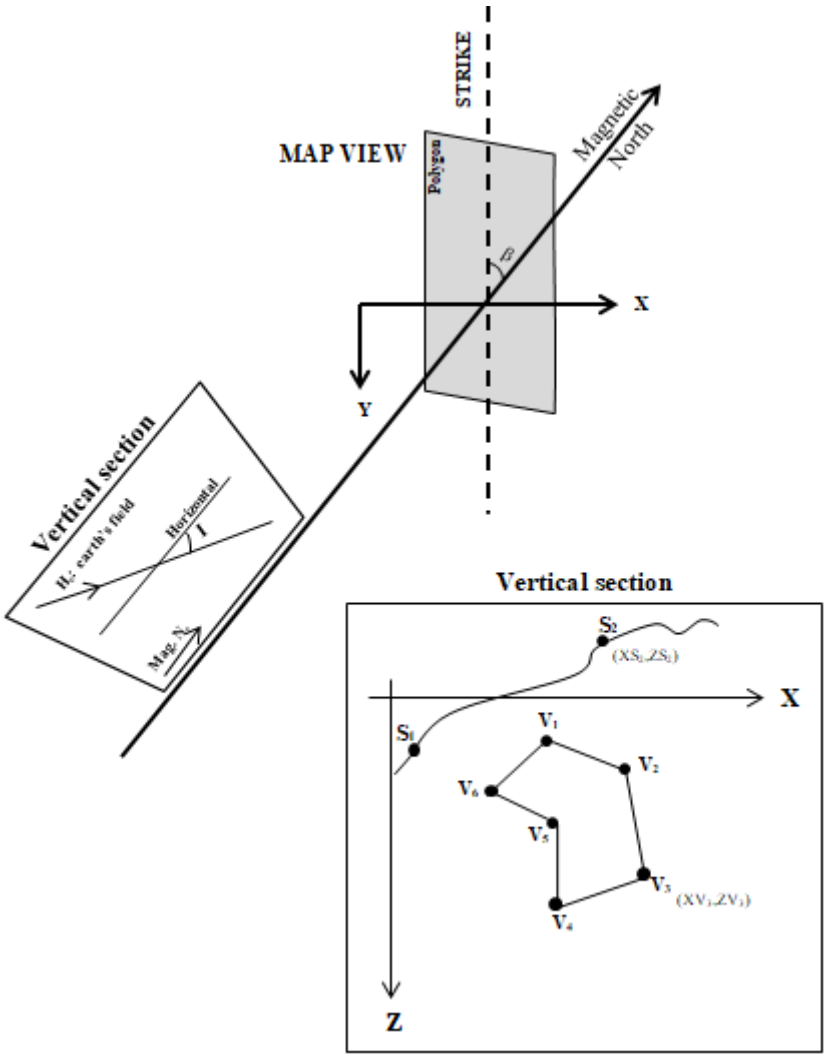

Figure 3.6. Geometrical conventions used in the calculous of the magnetic anomaly. The angles I and β represent the inclination of the Earth's magnetic field and the strike of the polygon, respectively. S_1 and S_2 are stations. In this example the polygon has six vertices. Adapted from Won and Bevis (1987).

The magnetic anomaly is defined as:

$$\Delta H = \frac{kH_e}{G\rho}\frac{\partial}{\partial a}\Delta g \tag{3.10}$$

Δg is the gravity anomaly, k is the polygon susceptibility, ρ is the polygon density, H_e is the scalar earth magnetic field strength and a is the direction of the induced magnetization.

The geometry and nomenclature for the magnetic anomaly are similar to those of previous gravity anomaly problem (Figure 3.6, Won and Bevis, 1987). However, unlike the gravity anomaly, the magnetic anomaly depends on the strike of the cylinder. Based on Figure 3.6, it is possible to show that:

$$\frac{\partial}{\partial a} = \sin I \frac{\partial}{\partial z} + \sin\beta \cos I \frac{\partial}{\partial x} \tag{3.11}$$

The vertical (ΔH_z) and horizontal (ΔH_x) components of the magnetic anomaly are derived from the (3.10) expression:

$$\Delta H_z = \frac{kH_e}{G\rho}\frac{\partial}{\partial a}\Delta g_z \tag{3.12}$$

$$\Delta H_x = \frac{kH_e}{G\rho}\frac{\partial}{\partial a}\Delta g_x \tag{3.13}$$

The expressions for the Δg_z and Δg_x are given by equations (3.1) and (3.2), respectively. Substituting these equations plus equation (3.11) into equations (3.12) and (3.13), the vertical and horizontal components become:

$$\Delta H_z = 2kH_e\left(\sin I \frac{\partial Z}{\partial z} + \sin\beta \cos I \frac{\partial Z}{\partial x}\right) \tag{3.14}$$

$$\Delta H_x = 2kH_e\left(\sin I \frac{\partial X}{\partial z} + \sin\beta \cos I \frac{\partial X}{\partial x}\right) \tag{3.15}$$

Once the ΔH_z and ΔH_x are known, the scalar total magnetic anomaly field ΔH is computed as:

$$\Delta H = \Delta H_z \sin I + \Delta H_x \sin\beta \cos I \tag{3.16}$$

The Won and Bevis (1987) algorithm computes the x-component, the z-component and the total magnetic anomaly field due to an infinite polygonal cylinder striking parallel to the y-axis and magnetized by an external magnetic field (Figure 3.6). These three components depend upon the: 1) relative locations of the polygon and the stations in the (x, z) plane, 2) magnetic susceptibility of the cylinder, 3) inclination of the Earth's magnetic field, 4) total field strength of the Earth's magnetic field, and 5) polygon strike. The strike corresponds to the angle from the magnetic north to the negative y-axis, measured in the horizontal plan (Figure 3.6). If the Earth's magnetic field has a ± 90º of inclination the strike is irrelevant and can be set as any value. Any number or sequence of stations can be chosen to compute the anomalies.

Chapter 4: Regional qualitative analysis of potential field data

The data analysis is an important stage of the research in order to understand the qualitative nature (i.e. characteristics of the potential field variations in order to identify geophysical domains) associated with the data. This is possible through the application of several enhancement techniques (spatial derivatives, analytical signal, etc.), and other methods, such as the Euler deconvolution, with the purpose of enhance and isolate the geological characteristics of interest: intrusion and Fontanelas volcano.

In this chapter, a theoretical introduction is presented focusing on gravity and magnetic data, some additional aspects behind the methods that were applied to perform the signal enhancement are also addressed. At the end of this chapter, a qualitative interpretation of the data is delivered and briefly discussed, considering some known geological features of the region. It is important to notice that the methods applied herein can provide quantitative information about the potential field data. However, the data interpretation carried out will only consider a qualitative point of view, aiming to constrain the key geological features that control the area of interest.

4.1. Gravity data

The theoretical concept associated with the gravity data is based on Newton's law of gravitational attraction which states that two objects are mutually attracted with a force that is dependent on the mass of the objects and the distance between them. More specifically, the magnitude of the force between two particles of masses m_1 and m_2 is directly proportional to the product of the two masses and inversely proportional to the square of the distance between the centres of mass:

$$\vec{F} = -G\left(\frac{m_1 m_2}{r^2}\right)\hat{r} \tag{4.1}$$

F is the force applied on m_2, $\hat{r}$ is the vector from the mass m_2 to mass m_1, r is the distance between m_1 and m_2 and G is the gravitational constant (6.67×10^{-11} $m^3.kg^{-1}.s^{-2}$). The minus signal reflects the attractive character associated with the force vector.

The acceleration of m_2 due to the presence of m_1 is the force F divided by the mass of m_2, i.e. the acceleration g is equal to the gravitational force due to m_1 per unit of mass attracted:

$$\vec{g} = -\left(G\frac{m_1}{r^2}\right)\hat{r} \tag{4.2}$$

Supposing that Earth is a homogeneous perfect sphere, and M_E is the mass of the Earth, g becomes the acceleration of gravity and is given by:

$$\vec{g} = -\left(G\frac{M_E}{R_E^2}\right)\hat{r} \tag{4.3}$$

Where R_E is the radius of the Earth and the vector $\hat{r}$ is pointing towards its centre. The numerical value of g at the Earth's surface is approximately 9.80 m/s^2. However, because the Earth is not a perfect sphere, this value is not constant all over the Earth's surface. There are several factors that influence it, such as the latitude and elevation of the measurement point, as well as the density of the

rocks that constitutes the underground. The objective of using gravity data is directly related with variations of density associated with the geology.

The cgs unit of acceleration is often called Gal where 1 cm/s^2 = 1 Gal, in honour of Galileo Galilei, who made the first measurement of the acceleration of gravity. However, the geophysical literature often reports the results in units of mGal (1 mGal = 10^{-3} Gal = 10^{-5} m/s^2).

The observed gravity data is the sum of several gravity components, most of which do not correspond to the density variations due to geology. In order to isolate the geological anomalies from all the other signals it is necessary to perform several corrections to the observed gravity data. However, this last quantity represents only a small part of the total gravity. Anomalies caused by crustal density variations are usually less than 100 mGal, which corresponds to less than 0.01% of observed gravity (Blakely, 1995).

4.1.1. Theoretical or normal gravity

The theoretical or normal gravity is the calculated earth's surface gravity by a mathematical model which considers a simple, regular ellipsoidal earth. Thus, the theoretical gravity corresponds to the vertical component of the attraction applied by the reference ellipsoid (equipotential surface of a uniformly dense earth).

The International Gravity Formula currently in use was accepted by the International Association of Geodesy (IAG) in 1980. The mathematical formula defining the theoretical gravity in mGal units is:

$$g_0 = 978032.67714 \frac{1 + 0.00193185138639 sin^2\lambda}{\sqrt{1 - 0.00669437999013 sin^2\lambda}} \tag{4.4}$$

4.1.2. Free air anomaly

The free air is a correction that accounts for the elevation of the measurement point above the reference ellipsoid, without accounting for the masses between these two surfaces. Assuming a spherical earth, the free air correction is:

$$g_{FA} = -\frac{2G}{R}h \tag{4.5}$$

where R is the radius of the earth at sea level, G is the gravitational constant and h is the height above or below the reference surface.

It is important to notice there is a difference between correction and anomaly. Generally, a correction is applied to the measured/observed value (although, it can also be applied to the theoretical value) and the anomaly is the difference between the measured value and the corrected theoretical value, thus: $\Delta g = g_{obs} \pm correction$. Consequently, the free air anomaly is:

$$\Delta g_{FA} = g_{obs} - g_0 - g_{FA} \tag{4.6}$$

The free air anomaly is equivalent to what would be observed if all the topographic masses were condensed onto the geoid (Blakely, 1995), which corresponds to the equipotential surface of the earth's gravitational field that best fits the average sea level. In marine acquisitions, the free air anomaly is the observed gravity (g_{obs}) minus the normal gravity (g_0) because there is a little or no

difference between the geoid and the measurement surface, once it matches the sea level. Thus, in this case, the free air correction (g_{FA}) is zero (Figure 4.1).

4.1.3. Bouguer anomaly

The Bouguer anomaly is named after Pierre Bouguer, a French mathematician, which led, among others, the first Ecuador expedition in which the first careful observations of the shape of the earth were made (Blakely, 1995). The Bouguer correction accounts for the attraction of material between the measurement and reference surfaces, which was ignored in the free air calculation. This correction assumes the presence of an infinite slab of uniform density and thickness with infinite horizontal extent lying between both surfaces:

$$g_B = 2\pi G\rho h \tag{4.7}$$

G is the gravitational constant, ρ is the density of the infinite plate and *h* is the thickness of the slab. At any reading point, *h* is equivalent to its high above sea level.

The Bouguer anomaly is given by:

$$\Delta g_B = g_{obs} - g_0 - g_{FA} - g_B - g_t \tag{4.8}$$

In onshore acquisitions, another correction is usually added to the Bouguer anomaly called the terrain correction, g_t, which accounts for the gravitational attraction of the adjacent topography. It is important to notice that the Bouguer anomaly reflects the density contrast between the anomalous masses and the chosen density to calculate the anomaly.

In the case of marine surveys, the Bouguer anomaly must consider the water column density (ρ_{sw}) and subtract it from the slab's density (ρ_{sf}):

$$g_B = 2\pi G(\rho_{sf} - \rho_{sw})z \tag{4.9}$$

where *z* is the thickness of the virtual slab which, in this case and for each reading point, is equivalent to the bathymetric depth. In this study, a density of 1.03 g/cm^3 was used for the water column and the correction density used to calculate the Bouguer anomaly was 2.3 g/cm^3 (Figure 4.2), because after visual analysis, it was the one that showed less topographical effects and better enhanced the features of interest.

4.1.4. Regional – Residual

The anomaly values correspond to the overlap of several anomalies due to density variations associated with the presence of distinct anomalous masses of different sizes and at different depths. The effect of deeper and larger geological structures is called the regional field, characterised by long-wavelength, large-scale variations. The gravity field after near-surface noise (from very shallow structures) and regional removal is called the residual, which presumably represents the effects of the geological bodies of interest.

In gravity data processing, it is important to perform a regional-residual separation with the aim to enhance the relevant geological anomalies. There are several methods to perform this separation, which include: graphical methods, polynomial adjustment, wavelength filtering and upward continuation filtering. In this case, a polynomial surface adjustment and a Gaussian filter were applied.

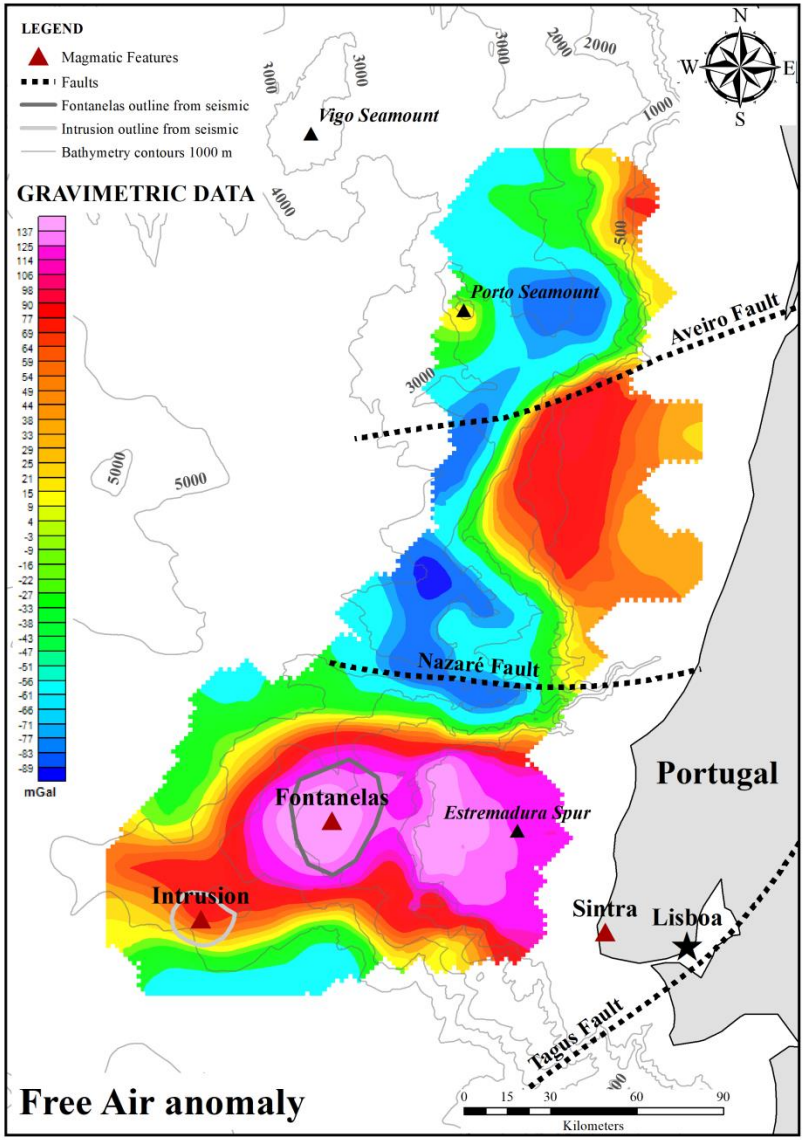

Figure 4.1. Free air anomaly map.

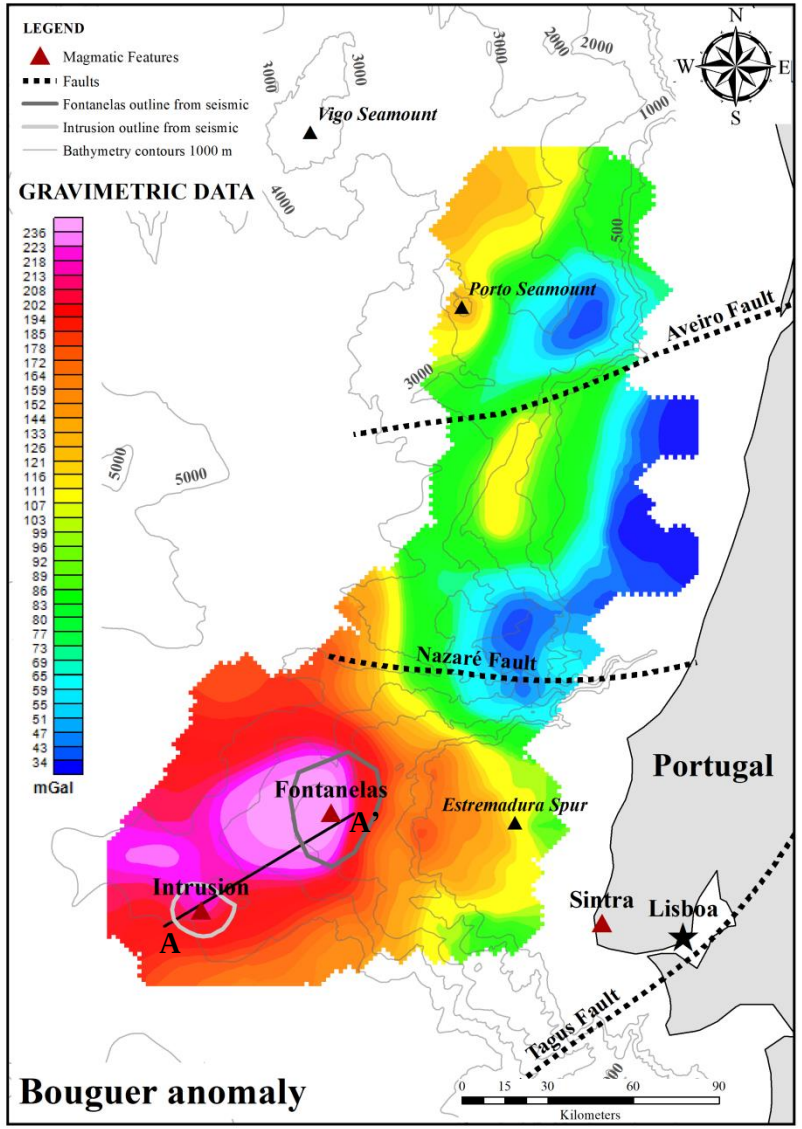

Figure 4.2. Bouguer anomaly map. The A-A' line represents the location of the 2D modelling profile.

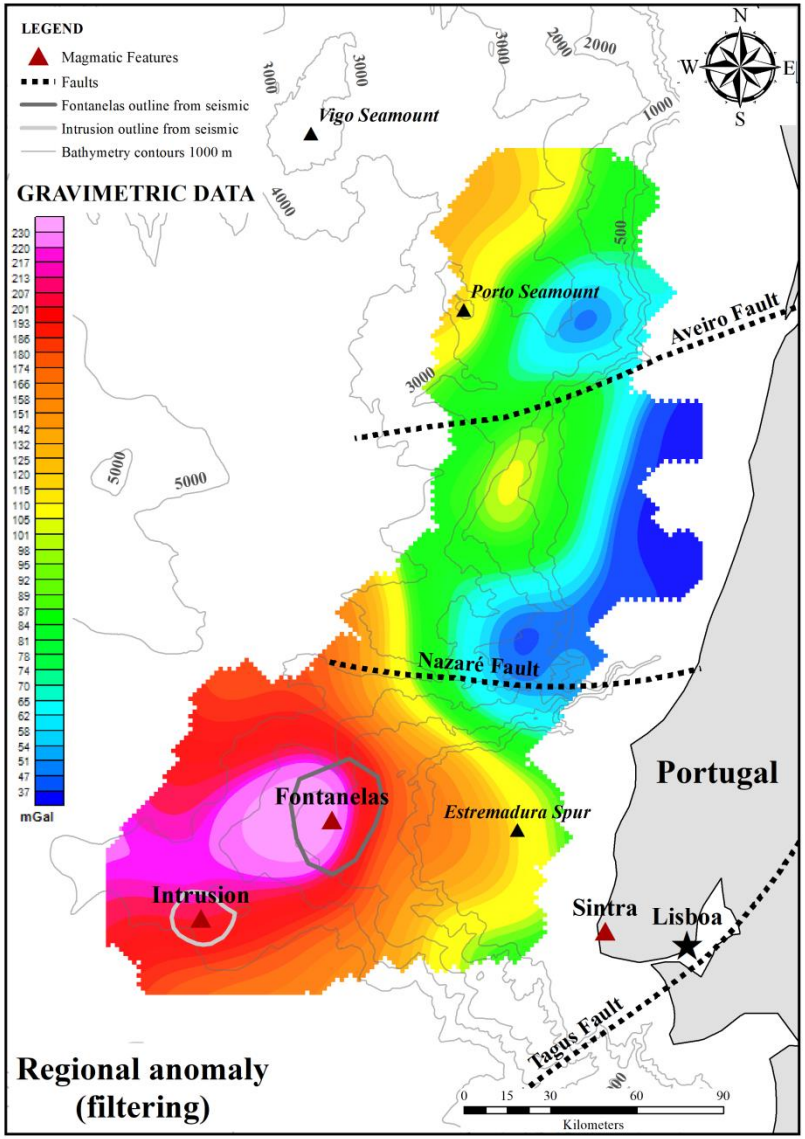

Figure 4.3. Regional anomaly map calculated through the filtering technique.

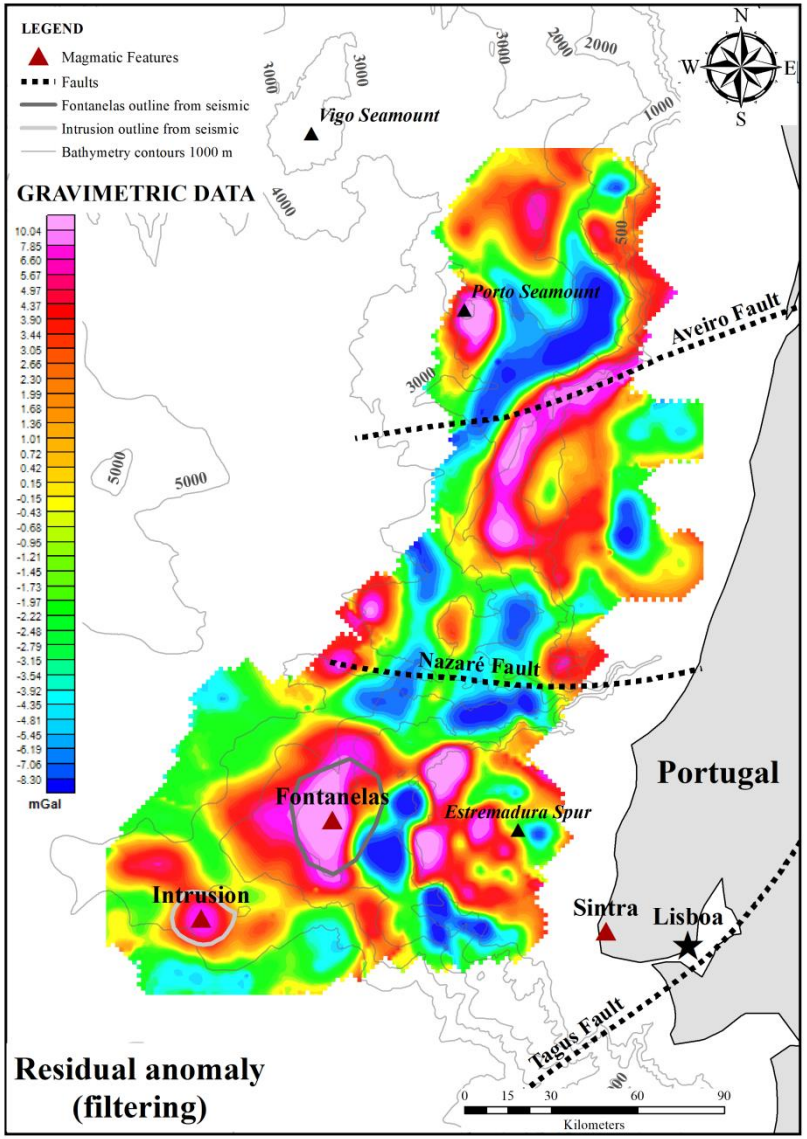

Figure 4.4. Residual anomaly map calculated through the filtering technique.

The polynomial method consists in adjusting a polynomial surface to the field which will represent the regional field, and then the calculated regional anomaly is subtracted from the Bouguer anomaly to obtain the residual anomaly. The Gaussian regional-residual filter, which is often used for low-pass or high-pass applications (Geosoft, 2013) was applied with a filter standard deviation of 0.02.

These two approaches produce different results. Considering that one of the goals of the data analysis is to individualize the two target magmatic features, the residual anomaly grid resulting from the Gaussian filtering technique (Figure 4.4) yields a better result compared with the residual anomaly obtained with the 1st order polynomial surface removal (Annex 1), once the regional field is more complex than a plane (1st order surface).

4.2. Magnetic data

The geomagnetic field is the earth's magnetic field. More than 90 per cent of this field is generated by internal sources (Robert L. Mcpherron, 2019) and a small part is originated outside the earth. The internal sources of the geomagnetic field are located mainly in two regions (Blakely, 1995): the outer core (core field or main field) and the crust (crust field). A variety of mechanisms have been proposed in order to explain the generation of the main field and currently the geomagnetic dynamo theory is the most accepted.

The crustal magnetisation is the second major source of the internal magnetic field (Robert L. Mcpherron, 2019), due to the capability of the rocks (as a consequence of the magnetic minerals that constitute those rocks) to acquire a magnetisation in the presence of an external magnetic field, causing detectable anomalies. This type of magnetisation is called the induced magnetisation, and if the rock is placed in a field-free environment, the induced magnetisation is zero (Blakely, 1995). The induced magnetisation aligns with the direction of the Earth's field H and is proportional to the rock's susceptibility χ (the higher is the magnetic susceptibility, the stronger is the induced field):

$$M_i = \chi \vec{H} \tag{4.10}$$

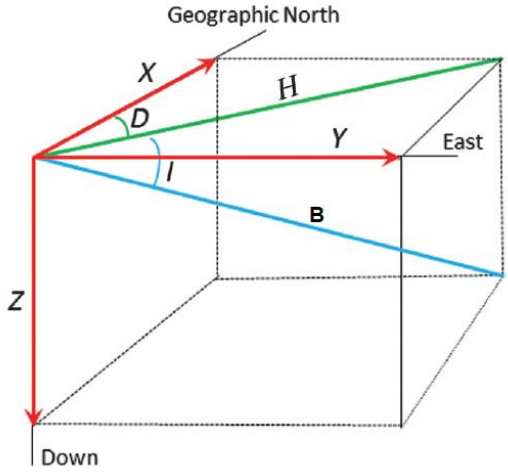

Figure 4.5. Concepts and relationships of the magnetic field components. From: Li and Pilkington (2016).

Other magnetic materials, under certain circumstances, for instance, during the formation process of the rock, the magnetic minerals can preserve magnetisation, even in the absence of an external field. This type of magnetisation is called remanent magnetisation (M_r). In crustal materials, remanent magnetisation depends not only of the crystallochemistry features of the rocks but also of their geologic, tectonic and thermal history (Blakely, 1995). The total magnetisation is the vector sum of the induced and remanent components of magnetisation (Blakely, 1995): $\vec{M} = \vec{M}_i + \vec{M}_r$.

At the earth's surface the geomagnetic field can be described using three orthogonal components and typically *x* increases to the north, *y* to east and *z* down (Figure 4.5). These three components are often written as B_x, B_y and B_z, where *B* (Figure 4.5) is the magnetic induction that, in geophysical studies is often expressed, in SI units, as nanotesla (Blakely, 1995). The magnetic field can be described by its total intensity as:

$$T = \sqrt{B_x^2 + B_y^2 + B_z^2} \tag{4.11}$$

and two angles: inclination *I* and declination *D* (Figure 4.5). The inclination is the vertical angle between the vector and the horizontal plane (Blakely, 1995):

$$I = arctan \frac{B_z}{\sqrt{B_x^2 + B_y^2}} \tag{4.12}$$

The declination is the angle between geographic north and magnetic north:

$$D = arcsin \frac{B_y}{\sqrt{B_x^2 + B_y^2}} \tag{4.13}$$

By convention, the inclination is positive when the vector is inclined below the horizontal plane and negative when above this plane. On the other hand, the declination is positive to the east of the magnetic meridian (direction of the horizontal component of the Earth's magnetic field) and negative to the west of this meridian.

In ship magnetic surveys, magnetometers generally measure the magnitude of the total magnetic field and do not consider the direction of the vector neither distinguishes between the three spatial components of the magnetic field.

To the total magnetic field, the IGRF model calculated for the date of the survey is subtracted. The IGRF model is the empirical mathematical representation of the geomagnetic field, which intends to reflect the main (core) field without external sources.

Considering $\vec{T}$ as the total magnetic field at any point and $\vec{F}$ the regional field (Figure 4.6) at the same point, the total magnetic field anomaly is (Blakely, 1995):

$$\Delta\vec{T} = \left|\vec{T}\right| - \left|\vec{F}\right| \tag{4.14}$$

If $\Delta\vec{F}$ is the perturbation of the regional field $\vec{F}$, the total field $\vec{T}$ is given by (Blakely, 1995):

$$\vec{T} = \vec{F} + \Delta\vec{F} \tag{4.15}$$

$\Delta\vec{F}$ is the component of interest because it represents the perturbation associated with the source of the anomaly.

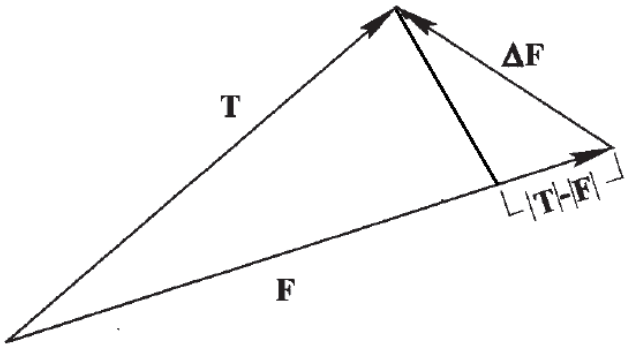

Figure 4.6. Vector representation of the total field anomaly. Adapted from Blakely (1995).

However, it is important to note that the total-field anomaly $\Delta\vec{T}$ is not equivalent to the magnitude of the anomaly field $\Delta\vec{F}$ because (Figure 4.6, Blakely, 1995):

$$\Delta\vec{T} = \left|\vec{F} + \Delta\vec{F}\right| - \left|\vec{F}\right| \neq \left|\Delta\vec{F}\right| \tag{4.16}$$

A visual study of the magnetic maps can be successful in a preliminary interpretation. In the case of the magnetic data provided for this study, it is visually clear (Annex 2) that the influence of the survey acquisition lines has an important effect on the anomalies distribution throughout the region. In order to improve the data and remove (as much as possible) this tendency, which does not represent geological information, a bandpass filter (used to pass or reject a certain wavelength interval from the data) was applied to remove the short-wavelength content (Figure 4.8). The wavelength interval (pass) applied to the data varied from a long-wavelength cut-off of 1000000 and a short-wavelength cut-off of 20000.

4.2.1. Dipolar field

The interpretation of magnetic data is often more challenging than the interpretation of gravity data because the magnetic anomalies are generally more complex, numerous and less persistent (Telford et al., 1990).

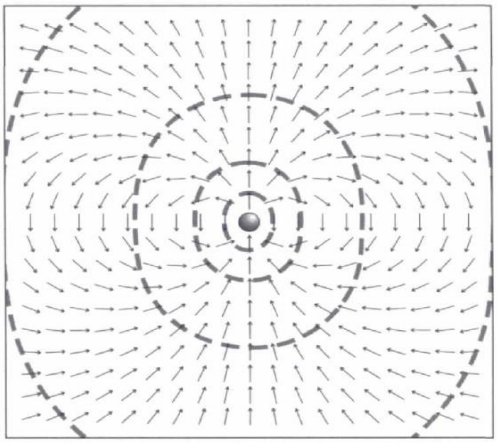

Figure 4.7. Magnetic field of a dipole (from Blakely, 1995).

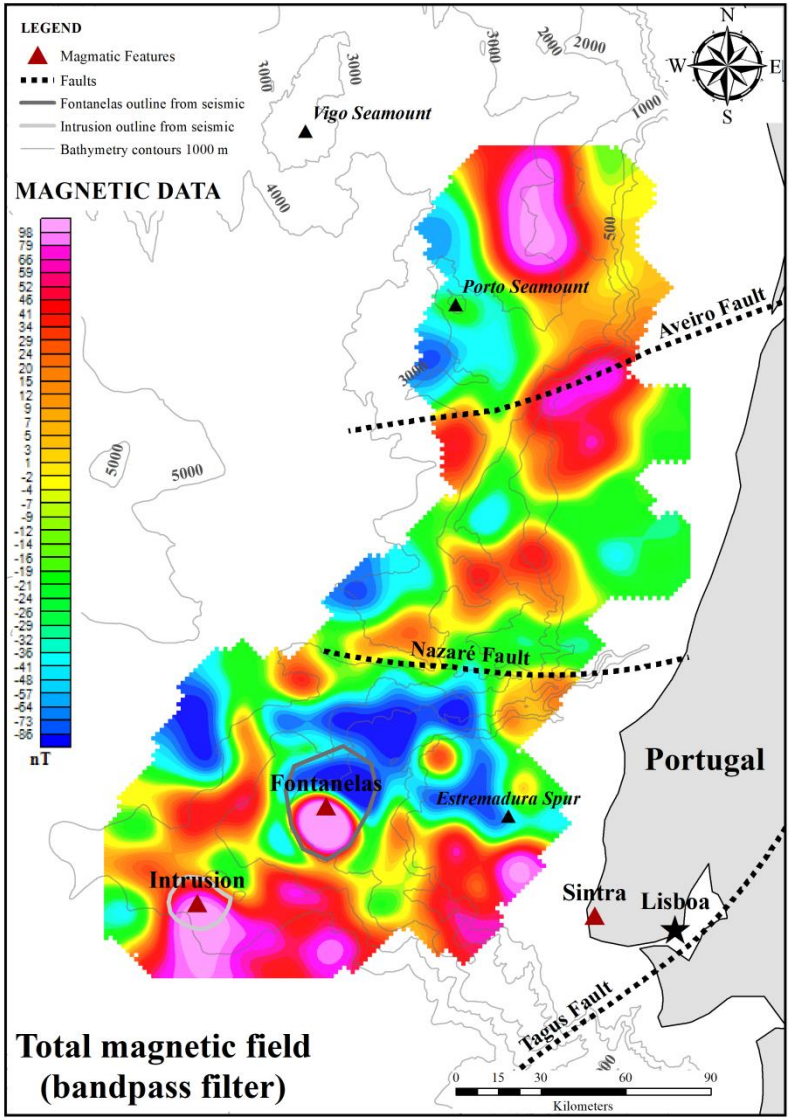

Figure 4.8. Total magnetic field map, with the bandpass filter applied.

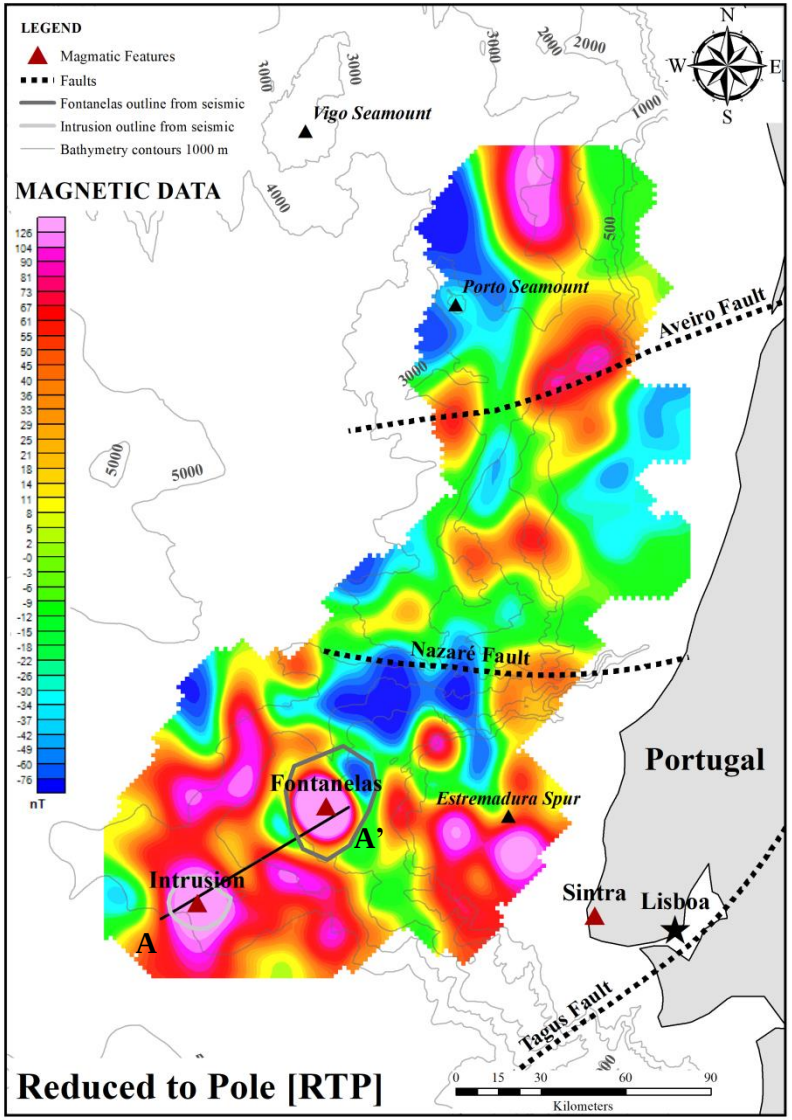

Figure 4.9. Reduced to pole magnetic map. The A-A' line represents the location of the 2D modelling profile.

Whereas the gravity map is typically dominated by regional effects, the magnetic map usually shows a multitude of local anomalies (Telford et al., 1990). This statement can be proven comparing the Bouguer anomaly (Figure 4.2) and total magnetic field (Figure 4.8) maps.

This difference is due to the: 1) dipolar character of the magnetic field against the monopolar character of the gravity field and 2) time dependence of the magnetic field contrasting with the mostly time-invariant gravity field (without accounting for minor or long-term changes due to redistribution of mass). The Earth's magnetic field varies in both direction and intensity (Blakely, 1995) over a wide spectrum of timescales: from small to great changes, the latter associated with the reversals of the geomagnetic field (Ravat, 2007).

The dominant component of the geomagnetic field is dipolar. The expression of the dipole in the Earth's surface is the presence of the geomagnetic poles (Figure 4.7). More specifically, the geomagnetic field is characterised by a dipolar and a nondipolar component, which are both linked to processes in the earth's core. However the nondipole field comprises only about 10 per cent of the main field, so considering the geomagnetic field as a dipolar field, with the dipole located at the Earth's centre, is a good first approximation (Blakely, 1995).

Dipolar magnetic anomalies are common in magnetic maps. Visually this effect can be identified in a total magnetic field map due to strong magnetic highs surrounded by weak magnetic lows (Bevan, 2017). This can be visualized in the total magnetic field map (Figure 4.8) associated with the Fontanelas anomaly.

4.2.2.Magnetic Pole Reduction

Positive gravity anomalies tend to be located over the respective body source, because it only depends on the mass of the geological entity, whereas magnetic anomalies can be sometimes shifted from its real position, distorted from its real shape and even phase-shifted (Blakely, 1995).

The morphology of a magnetic anomaly depends on several factors, such as the source's geometry, the direction of the Earth's magnetic field and the direction and magnitude of the remanent magnetisation. The dependence on the latitude at which the survey is performed is the most important factor that controls the main characteristics of the magnetic anomaly: in latitudes close to the Equator the shift and distortion of the magnetic anomalies are much more severe. At the South and North Poles, this effect is almost negligible because the magnetic field lines originated at these sites are near vertical.

These changes are caused by the inclination of the inducing field (Figure 4.10a). To overcome this complexity, in order to correlate the magnetic data with the geological features and other geophysical data, is necessary to perform a magnetic reduction to the pole, which transforms the anomaly as if it the inducing magnetic field was vertical. The reduction to pole (RTP) shifts the anomalies' location and shape resulting in a monopolar symmetrical anomaly overlying their respective geological source (Figure 4.10b). The RTP is formulated as:

$$L(\theta) = \frac{1}{(\sin(I) + i\cos(I) \cdot \cos(D - \theta))^2} \tag{4.17}$$

I is geomagnetic inclination and *D* is the geomagnetic declination.

There are several assumptions that have to be considered when applying the RTP: (1) the magnetisation is uniform throughout the area, which is only appropriate in small-scale surveys

(Blakely, 1995), (2) all magnetisation is parallel to the geomagnetic field and, consequently, (3) the remanent magnetisation is null or insignificant. In situations where these assumptions are not fully understood the magnetic pole reduction should be used carefully.

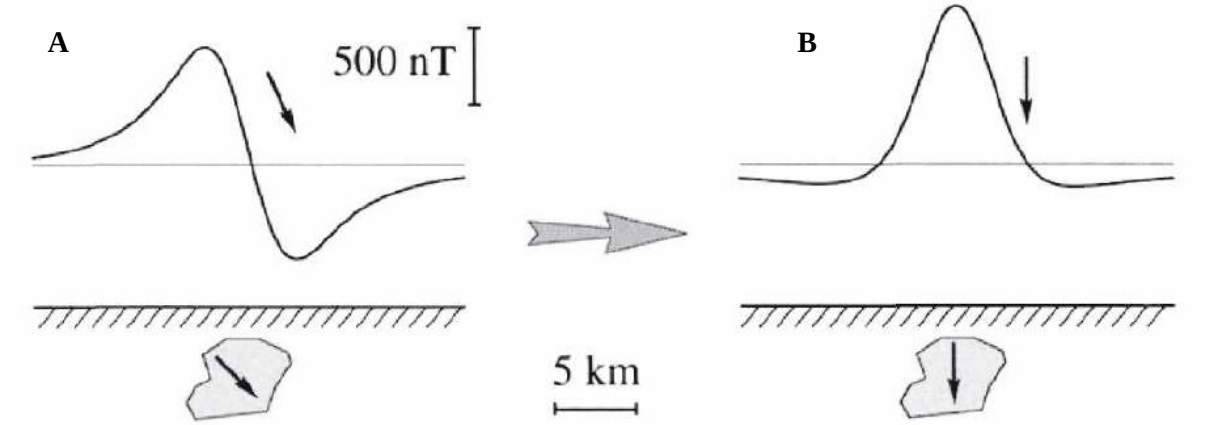

Figure 4.10. Magnetic anomaly **a)** before and **b)** after being reduced to pole (from Blakely, 1995).

4.3. Signal enhancement techniques

The signal enhancement is a preliminary approach, usually applied to the potential field data with the aim to reveal the main regional features and explore the potentiality of the gravity and magnetic (reduce to pole) data.

4.3.1. Horizontal and vertical derivatives

First derivative maps from magnetic and gravity data are very useful in identifying the source's anomaly edges and enhance shallow features, suppressing the deeper sources in the data (Geosoft, 2013). The first derivative is interpreted as the change rate (the reason why the first derivative is also called gradient) of one variable with respect to another. For example, variations in gravity and magnetic susceptibility with respect to horizontal or vertical distance.

The first vert derivatives enhance the small wavelength content in potential field data and are very helpful in detecting and interpreting abrupt changes in the gravity and magnetic signal, indicatory of faults and/or boundaries between different geological units. The derivatives are calculated in the wavenumber domain (Geosoft, 2013) as:

$$L(\omega) = (\omega i)^n \tag{4.18}$$

$$L(\omega) = \omega^n \tag{4.19}$$

The expression (4.18) corresponds to the first horizontal derivative, whereas the expression (4.19) corresponds to the first vertical derivative: where ω is the angular wavenumber in radians/ground unit and *n* the order of differentiation, which dictates the wavenumber component to enhance: greater the *n*, greater the higher-wavenumber components of the spectrum to enhance (Geosoft, 2013). After the calculation of the derivatives in the wavenumber domain is necessary to return to the spatial domain by applying the inverse transform.

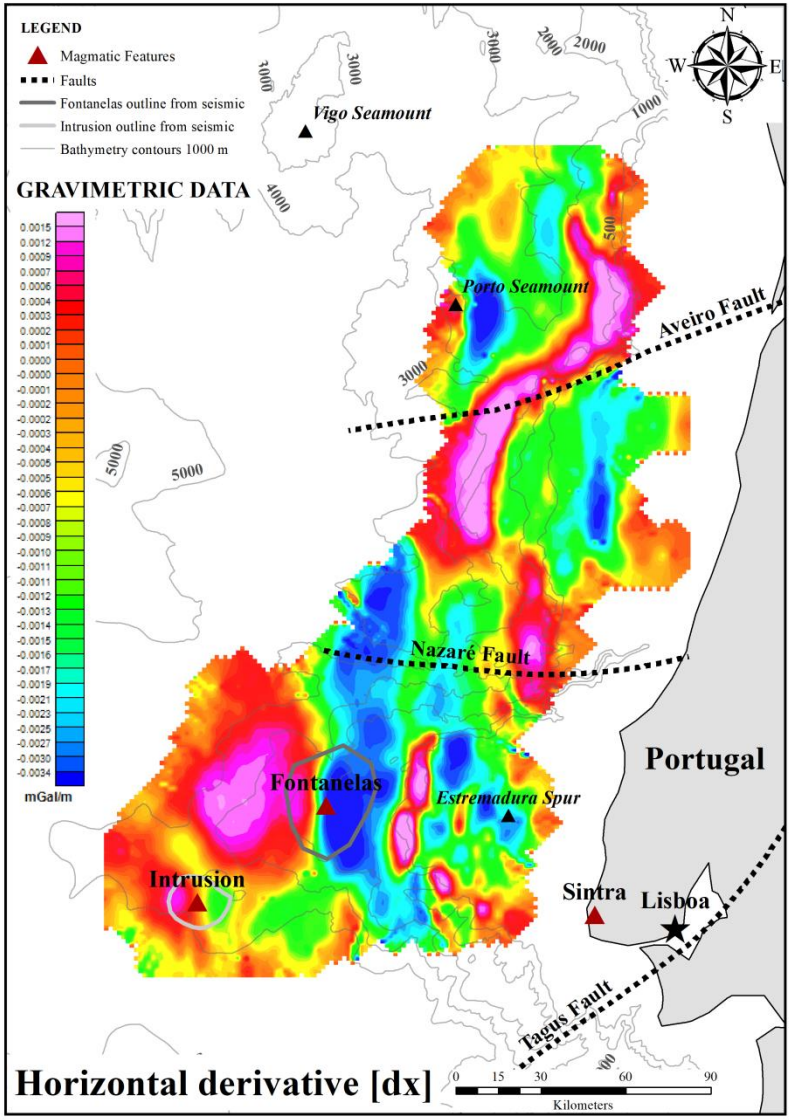

Figure 4.11. Horizontal derivative (x-direction) map of the gravity data.

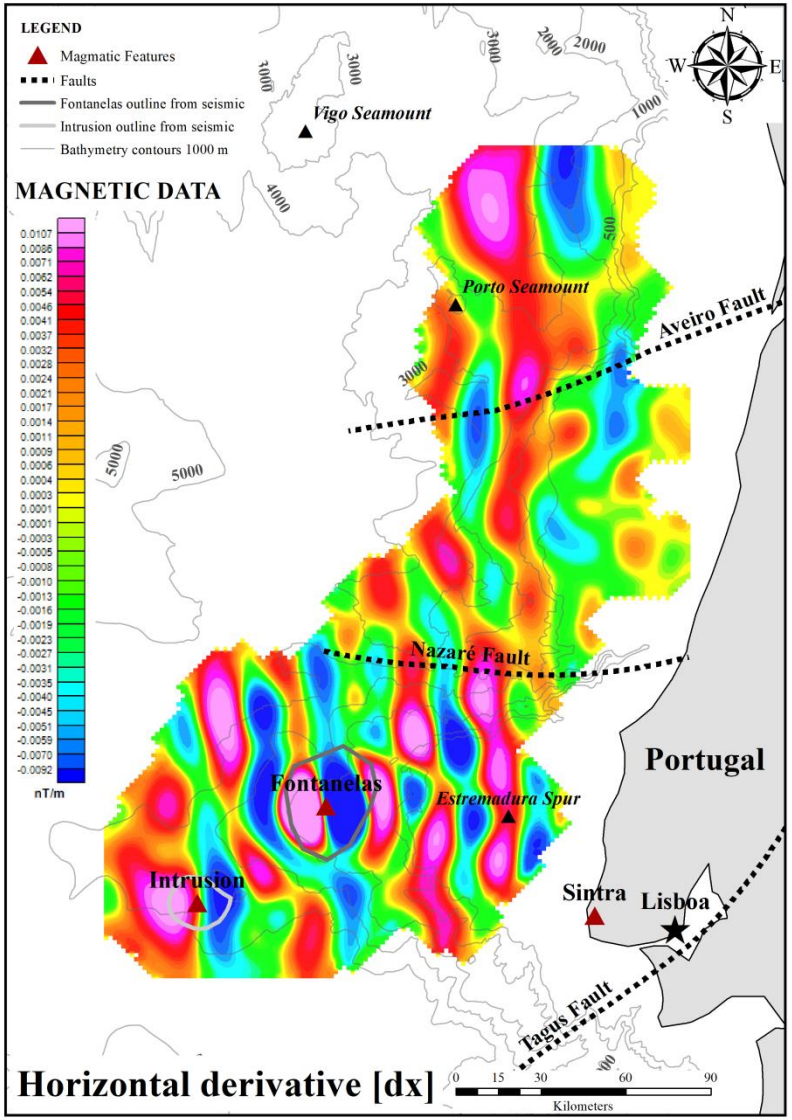

Figure 4.12. Horizontal derivative (x-direction) map of the magnetic data.

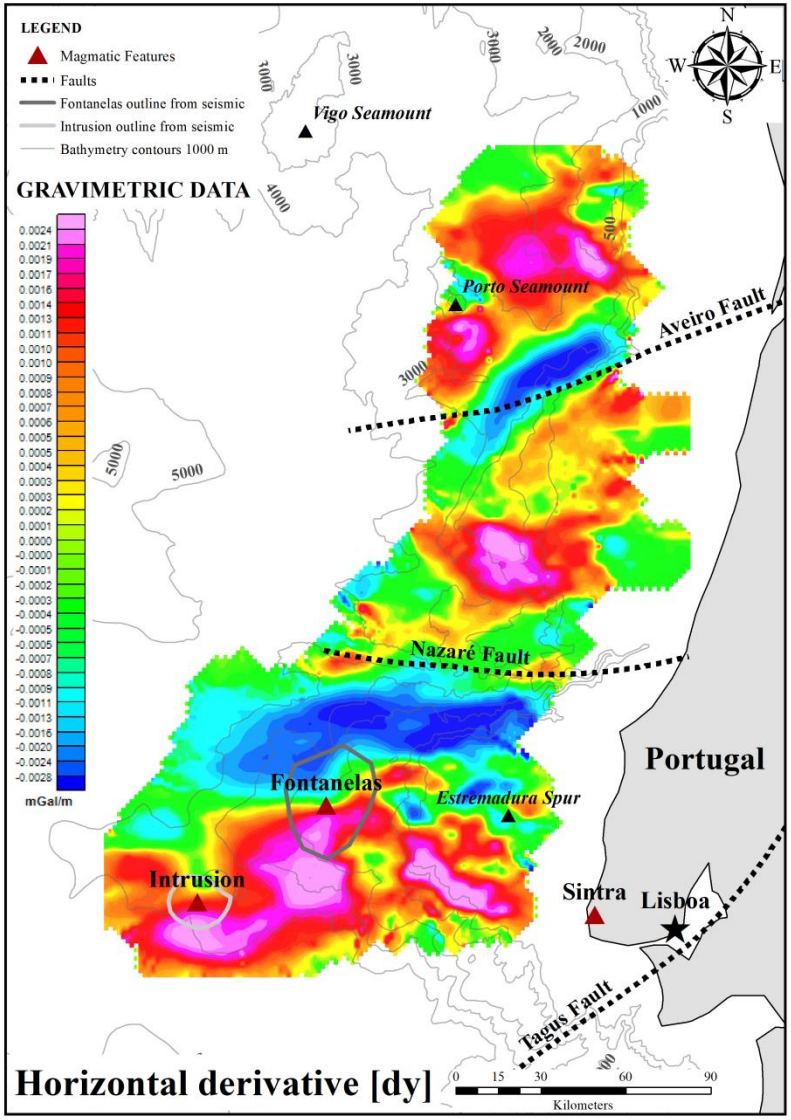

Figure 4.13. Horizontal derivative map (y-direction) of the gravity data.

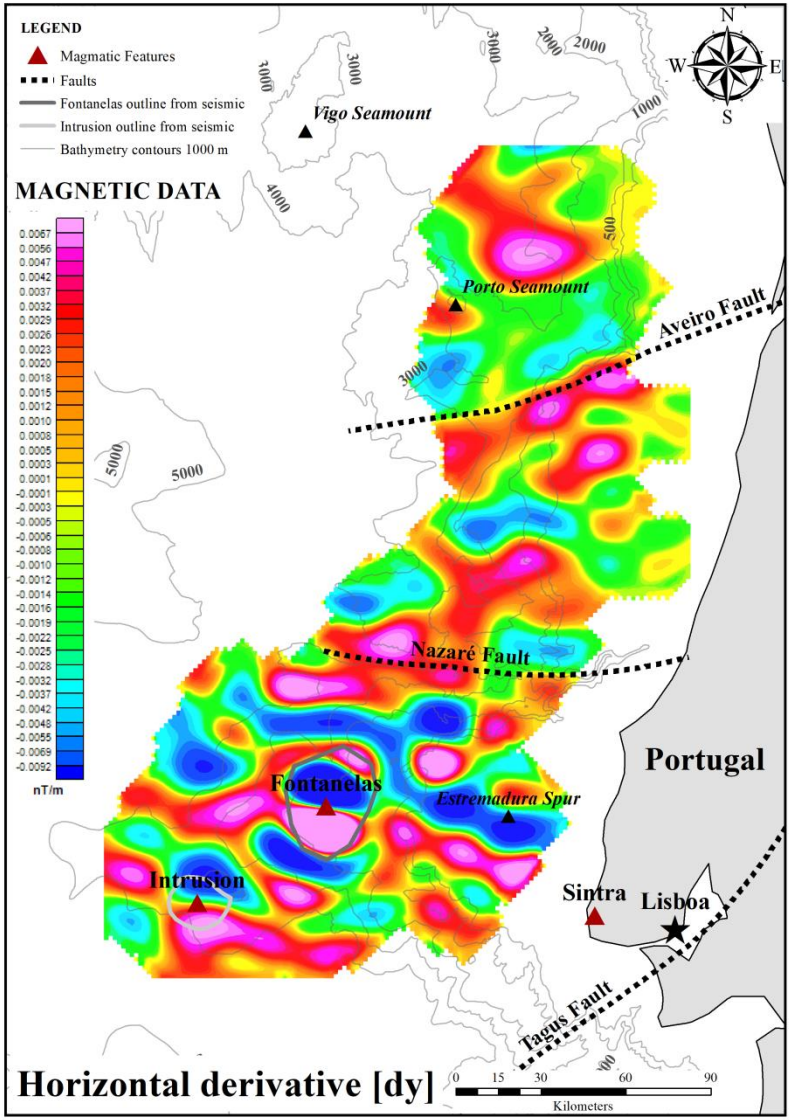

Figure 4.14. Horizontal derivative map (y-direction) of the magnetic data.

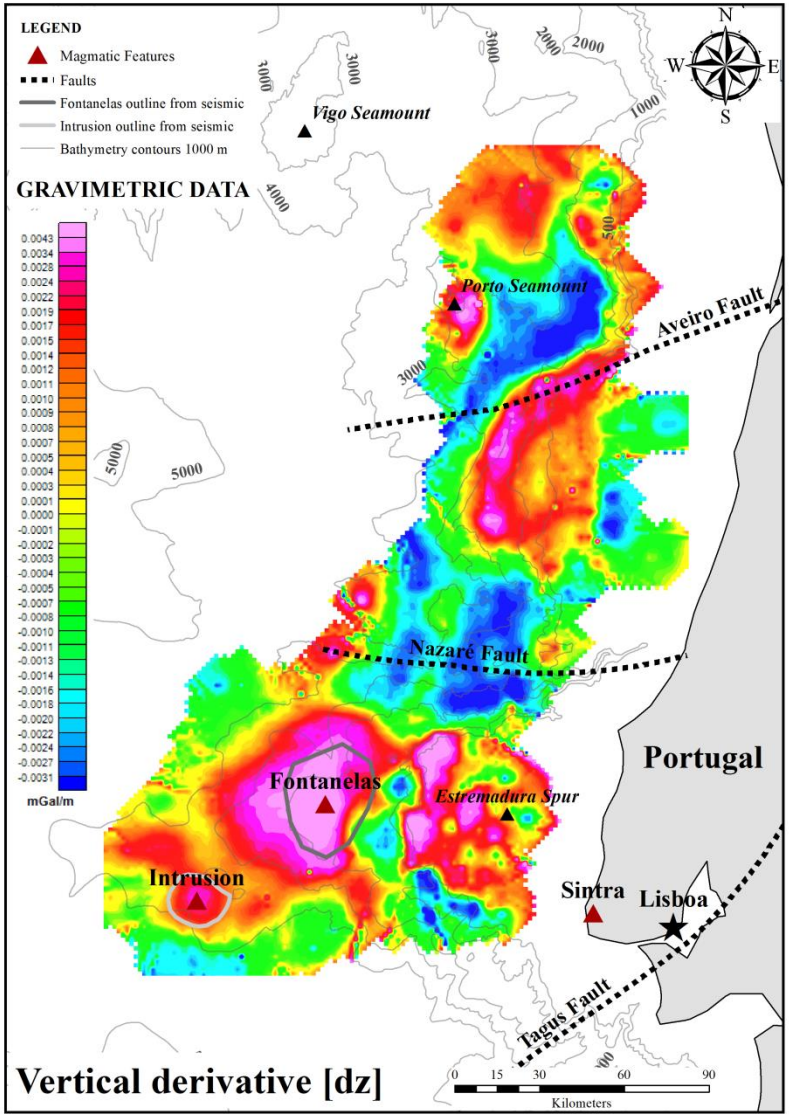

Figure 4.15. Vertical derivative map of gravity data.

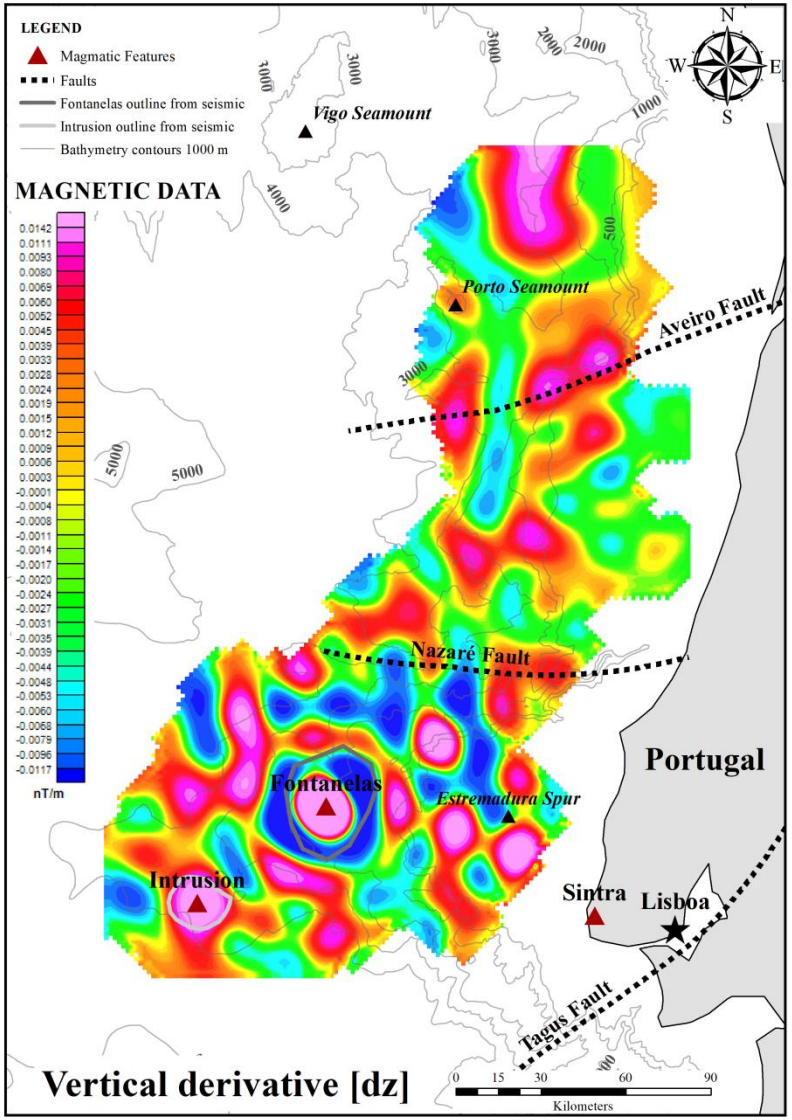

Figure 4.16. Vertical derivative map of magnetic data.

In magnetic data, it is important to be aware that an incorrect RTP transformation or the presence of remanent magnetisation will shift the maximum derivative values from the exact location of the contact (Salem et al., 2007).

Concerning the magnetic data, the horizontal derivatives maps, in the x (Figure 4.12) and y (Figure 4.14) directions, exhibit an N-S and E-W linear trend, respectively. Several approaches were applied to improve the data quality, however without success. It is thought that this effect is due to the acquisition conditions, because this tendency follows the survey lines. In the gravity data, it is possible to notice a slight trend in the horizontal derivative maps (Figure 4.11, Figure 4.13), however, it is not as strong as in the magnetic data. In the vertical derivative map, in both gravity (Figure 4.15) and magnetic (Figure 4.16) data this influence does not appear.

4.3.2.Analytic signal

The analytic signal is also known as the total gradient method since it involves the calculation of the horizontal and vertical derivatives of the potential field data. The amplitude of the analytic signal is defined as:

$$ASA = \sqrt{\left(\frac{\partial F}{\partial x}\right)^2 + \left(\frac{\partial F}{\partial y}\right)^2 + \left(\frac{\partial F}{\partial z}\right)^2} \tag{4.20}$$

Where F is the gravity or magnetic field and ∂x, ∂y and ∂z are the spatial orthogonal derivatives of the respective field.

The advantages of using the analytic signal in magnetic data are related to the fact that its magnitude is independent on the induced and remanent magnetisation. Therefore, it can be applied directly to the total magnetic field without performing the magnetic pole reduction.

This method generally produces gravity (Figure 4.17) and magnetic (Figure 4.18) anomaly maps that are very useful in locating the edges and boundaries of source bodies. The maximum values of the analytic signal occur over faults and contacts, coincident with magnetic and gravity signal contrasts.

4.3.3. Radial power spectrum

The examination of the power spectrum is an important method to understand the data in the wavenumber domain, which can be advantageous in several approaches, such as the residual-regional separation and when applying filtering techniques. In this case, it is introduced the radially averaged power spectrum, which corresponds to an average of power calculated in different directions for all grid elements at a certain wavenumber. The graphic plots the logarithm of the radial spectrum versus the wavenumber.

In the magnetic data, the power spectrum was applied to the reduced to pole grid, once this operation has no effect on the shape of the radially averaged spectrum (Ravat, 2007). The estimated source depth displayed in the lower graphics (Figure 4.19, Figure 4.20) is the average over five points.

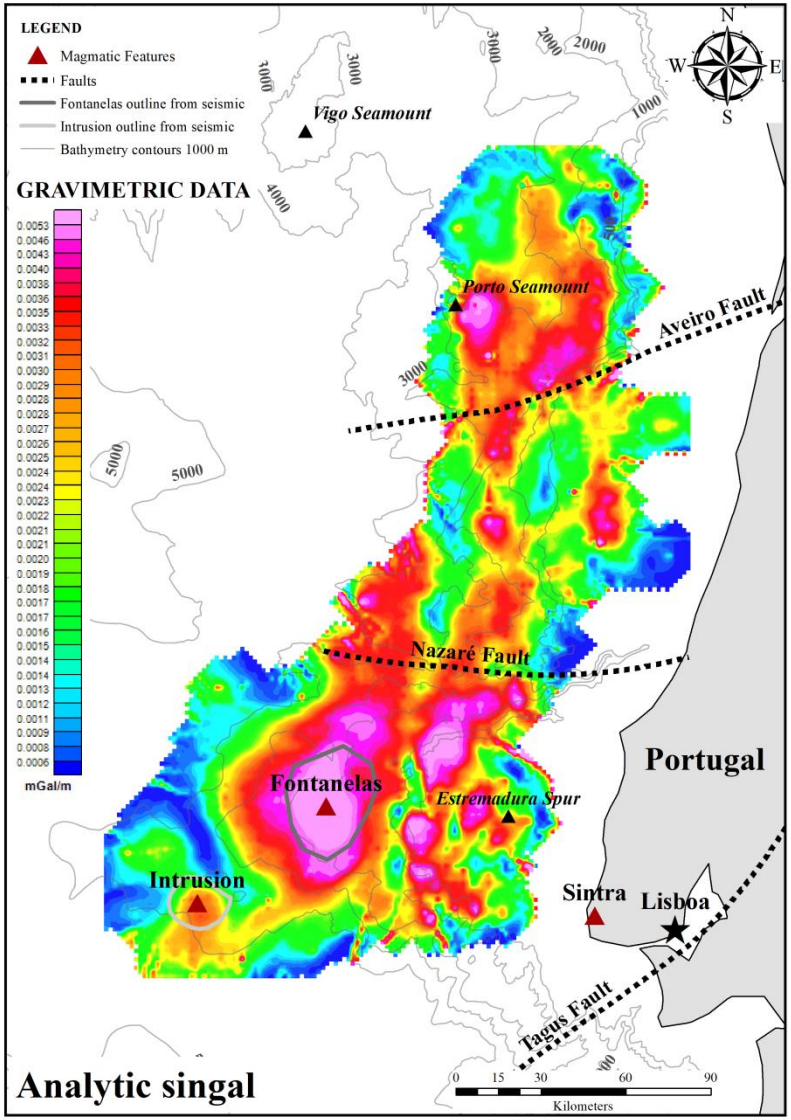

Figure 4.17. Analytic signal map of gravity data.

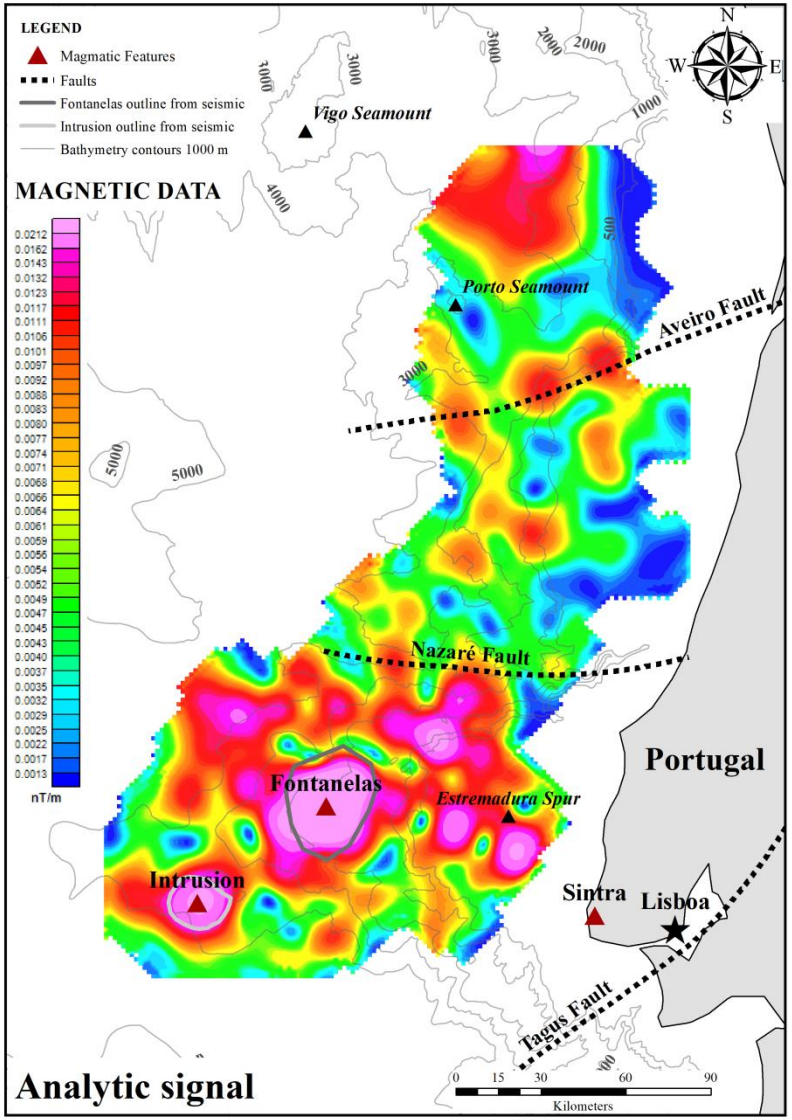

Figure 4.18. Analytic signal map of magnetic data.

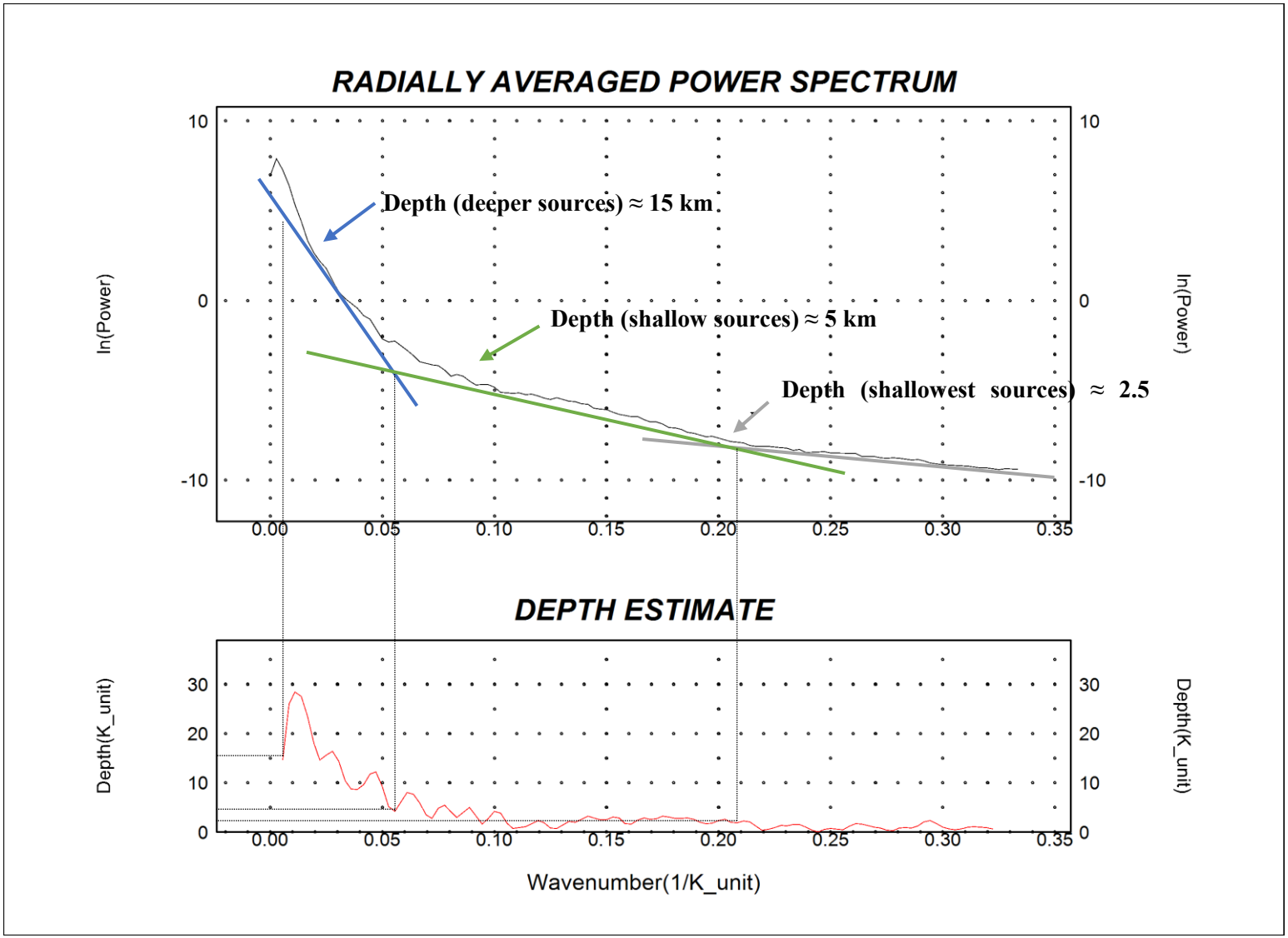

Figure 4.19. Radially averaged power spectrum (top) and depth estimate graphic (down) of the gravity data.

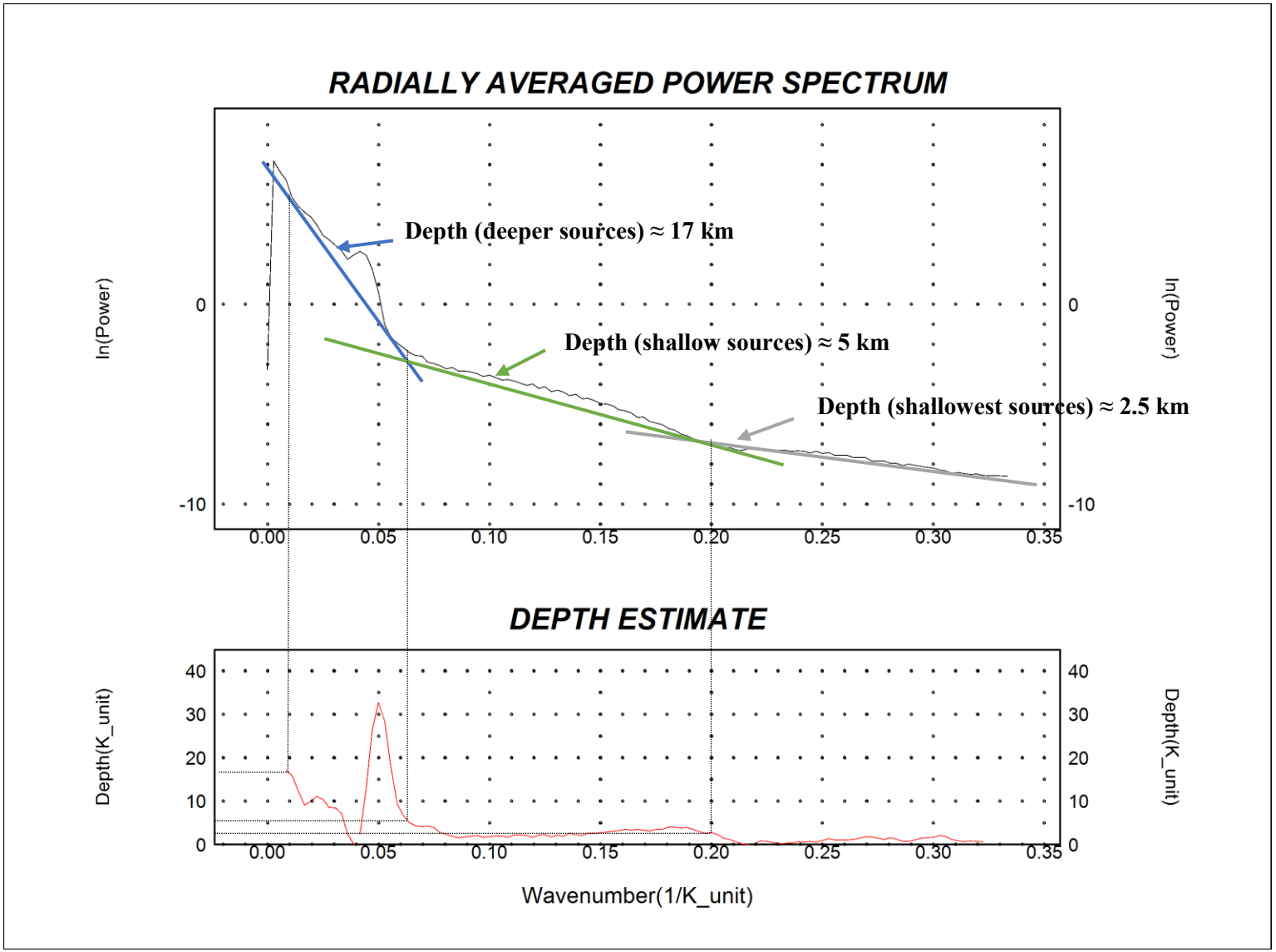

Figure 4.20. Radially averaged power spectrum (top) and depth estimate graphic (down) of the magnetic data.

The depth to an ensemble of sources is determined by the expression (Geosoft, 2015a):

$$z = \frac{-s}{4\pi} \quad (4.21)$$

Where *z* is the depth and *s* is the slope of the log energy spectrum.

From the power spectrum of the gravity (Figure 4.19) and magnetic data (Figure 4.20), it is possible to identify three major segments: a first segment characterised by the highest slope, an intermediate sector where the logarithm of the power decline more gradually and the last segment in which there is almost no variation. All these three segments can be related with the depth of source anomalies: the first is indicative of the deeper sources (regional field), the middle sector represents the geological sources of interest and the last sector corresponds to the shallowest sources associated with the data.

4.3.4. Upward continuation

Upward continuation is a filtering technique frequently applied to the gravity and magnetic field to attenuate the shorter-wavelength content from the data (shorter the wavelength, greater the attenuation (Blakely, 1995)) by adjusting the measured potential field as if the measurement surface was above its real position by a given distance.

This process of continuing the acquisition surface upward is an aid to the interpretation and has several advantages when applied to potential field data (Blakely, 1995): (1) attenuates the anomalies of shallower sources allowing the assessment of anomalies caused by deeper sources, (2) homogenize aerial measured surfaces performed at different altitudes so that different surveys can be compared between each other and (3) reduce shorter-wavelength data noise.

The upward continuation process is very useful where local, near-surface structures add considerable shorter-wavelength content to the data, such as volcanic rocks, which prevent the identification of the underlying structures (Blakely, 1995).

Upward continuation is often considered a clean filter once it produces almost no side effects that require the application of other filters or processes to correct (Geosoft, 2013). This filter is applied in the wavenumber domain (which later needs to be converted again to the space domain):

$$L(\omega) = e^{-h\omega} \quad (4.22)$$

Where h is continuation level, which corresponds to the distance in ground units, to continue upward relative to the measurement surface and ω is the angular wavenumber in radians/ground unit (Geosoft, 2013). The negative sign in the exponent indicates an upward continuation, away from the source of the field (Ravat, 2007).

The upward continuation map analyses of gravity data (Figure 4.21) allows noticing that this is very similar to the regional anomaly map (Figure 4.3) because in both the influence of shallower sources is reduced. Thus, in both gravity (Figure 4.21) and magnetic (Figure 4.22) data the upward continuation maps are a visualization of the deeper sources in the area of study.

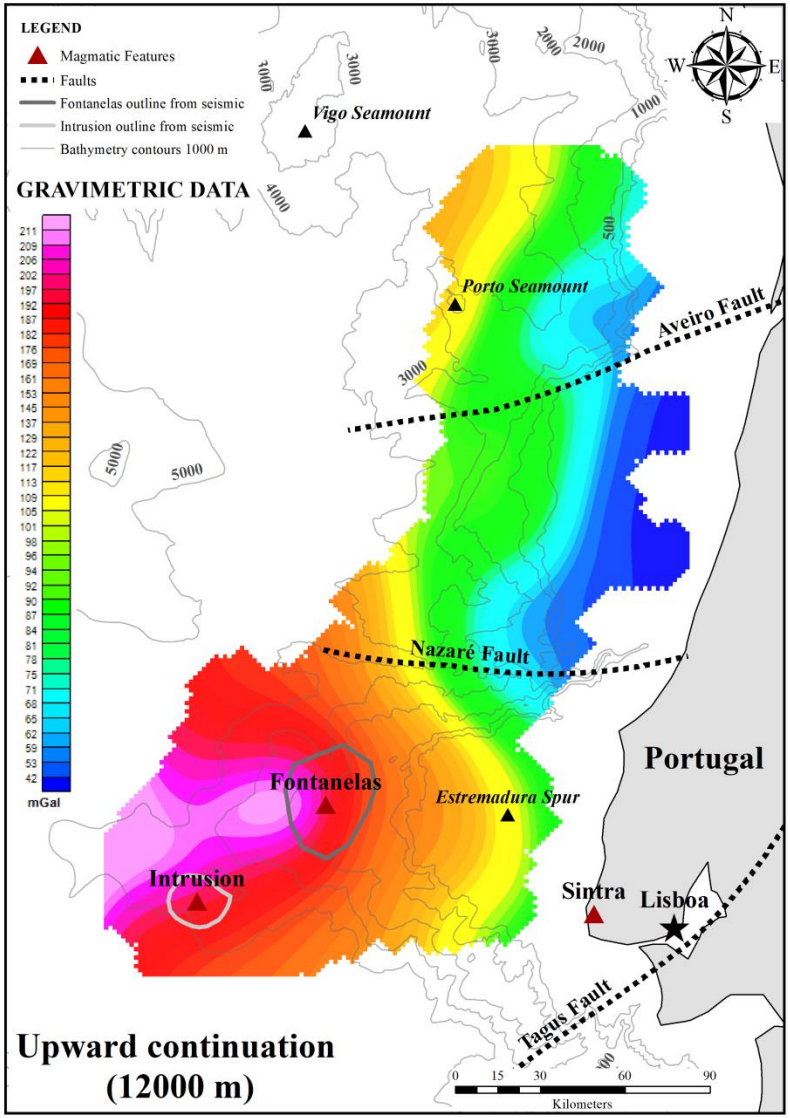

Figure 4.21. Upward continuation filter applied to gravity data (continuation height = 12000 m).

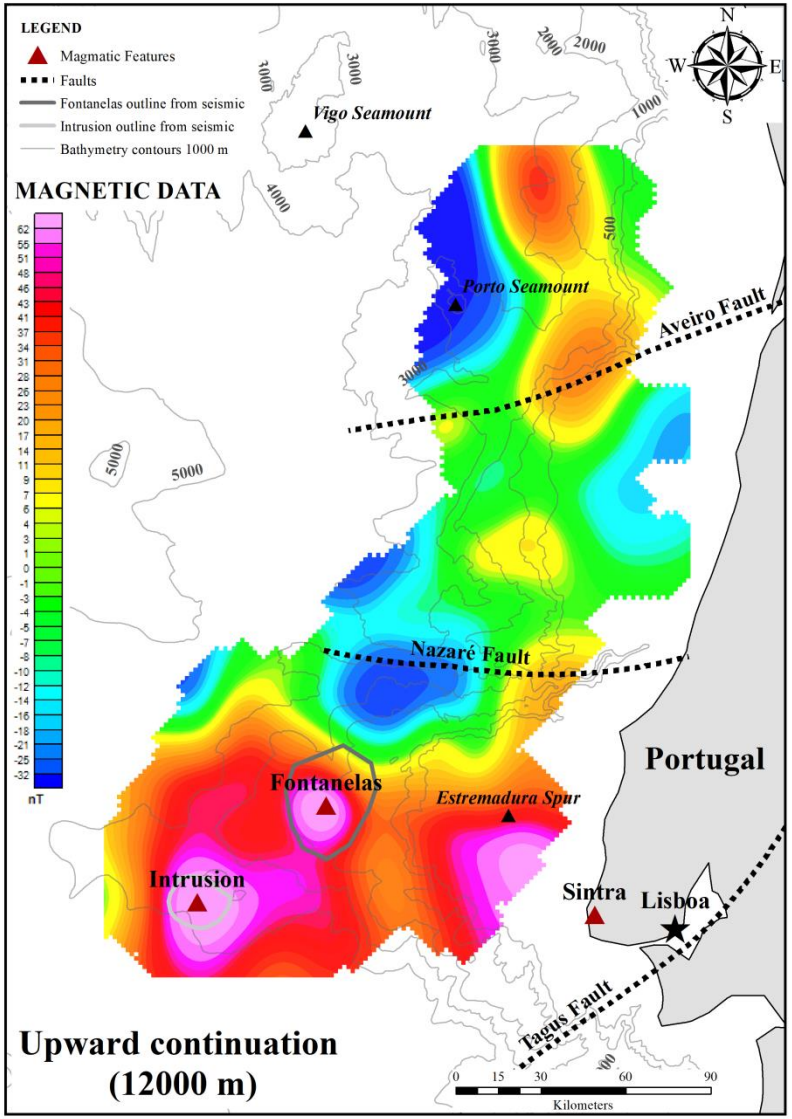

Figure 4.22. Upward continuation filter applied to magnetic data (continuation height = 12000 m).

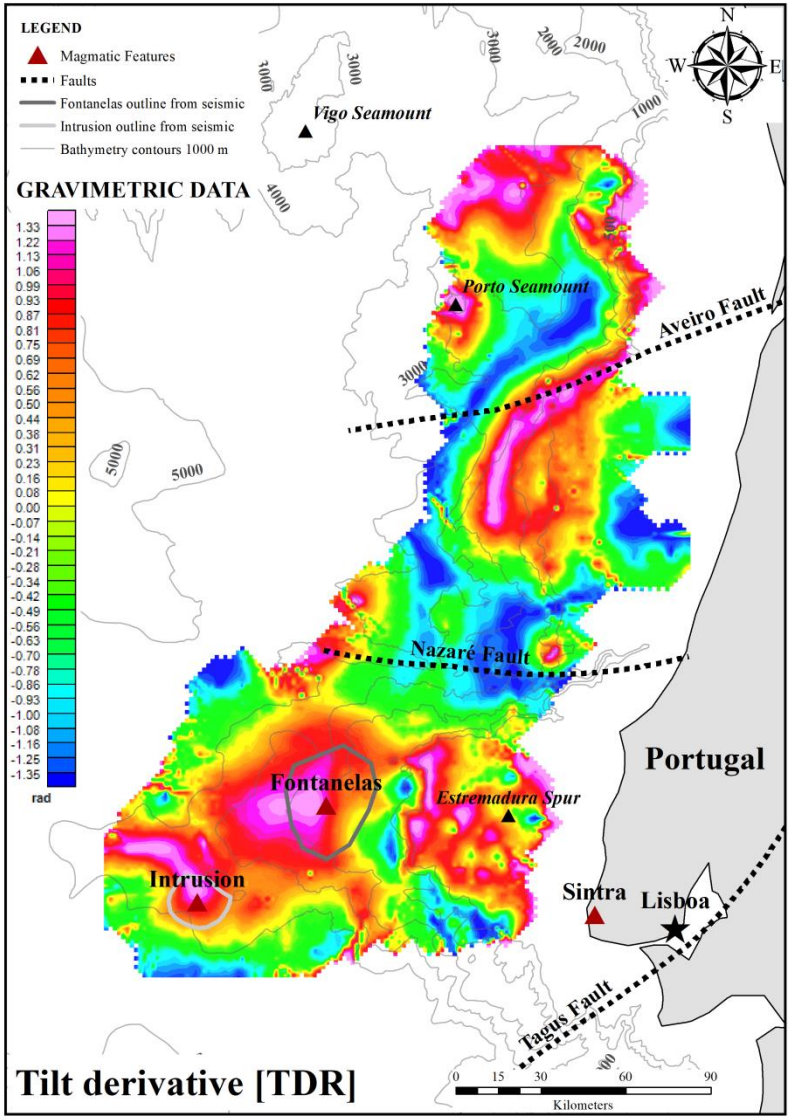

Figure 4.23. Tilt derivative map of gravity data.

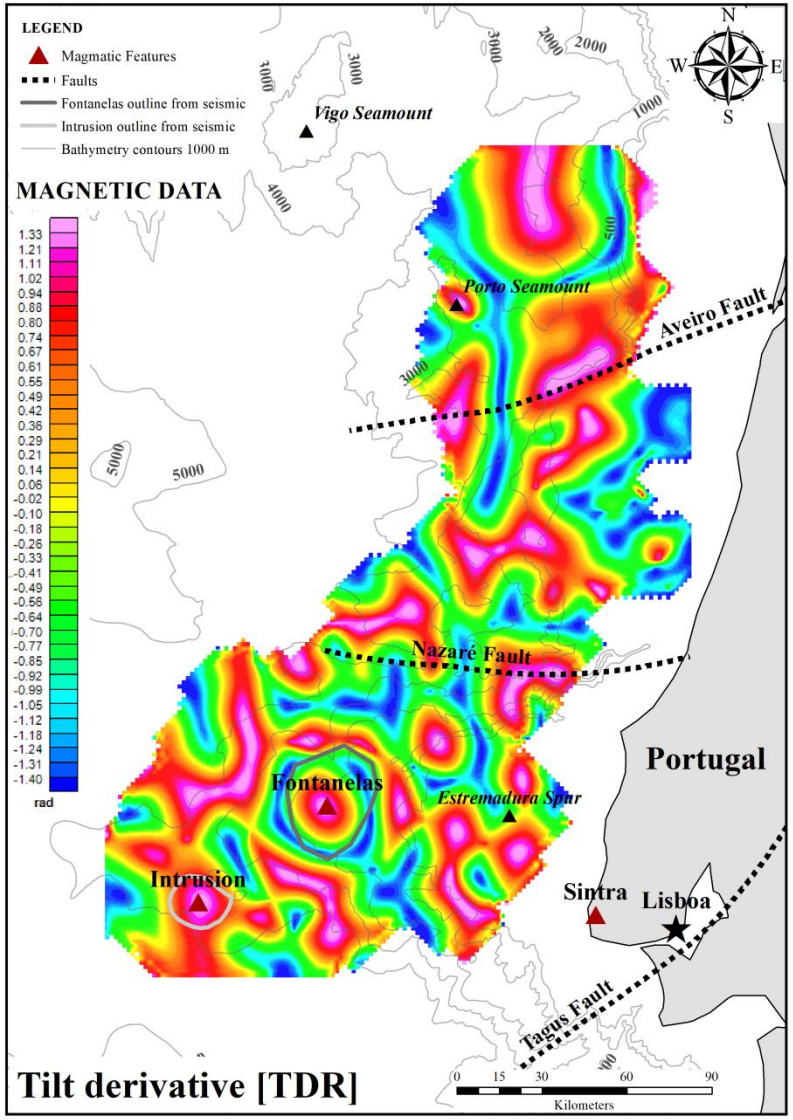

Figure 4.24. Tilt derivative map of magnetic data.

4.3.5.Tilt derivative

The tilt derivative (TDR) is another method to identify the shape and boundaries of the anomaly's sources. However, the tilt derivative is an advantageous method, especially with respect to magnetic data. Weak and strong magnetic bodies are treated in an equal way since the magnetisation dependence of the TDR is the same in both horizontal and vertical derivatives (Blakely et al., 2016). Although it strongly depends on the inclination of the magnetic field (Shahverdi et al., 2017). Other advantages include the ability to normalize a potential field map, discriminating between noise and signal (Verduzco et al., 2004). The tilt derivative is formulated as the ratio between the first vertical and total horizontal derivatives (x and y-direction) of the field intensity (Geosoft, 2015b):

$$TDR = \tan^{-1}\left(\frac{VDR}{THDR}\right) \tag{4.23}$$

Where VDR and THDR are the first vertical and total horizontal derivatives of the potential field *F*, respectively (Geosoft, 2015b):

$$VDR = \frac{dF}{dz} \tag{4.24}$$

$$THDR = \sqrt{\left(\frac{dTDR}{dx}\right)^2 + \left(\frac{dTDR}{dy}\right)^2} \tag{4.25}$$

The calculated tilt angles are within the range -90º to +90º from the horizontal, independently of the amplitude or wavelength of the magnetic field (Geosoft, 2015b). Concerning the magnetic data, the calculation of the tilt angle should be applied to a reduced to pole grid, to obtain a better estimation of the location of magnetic sources (Geosoft, 2015b).

The tilt derivative is useful in the interpretation of shallow basement structures and mineral exploration targets (Geosoft, 2015b). In TDR maps (Figure 4.23, Figure 4.24), the maxima of the tilt derivative should overlap the centre of the anomaly source and its zeros over the edges.

4.3.6. Euler deconvolution

The Euler method, also known as Euler deconvolution, named by Reid *et al.* (1990), is a widely applied procedure in both gravity and magnetic data. It provides a useful way to estimate the source body location and depth of an assemble of relatively simple bodies of ideal shapes, such as spheres or cylinders (Blakely, 1995). Though in more realistic and typical cases, when the bodies are more complex, the method has some limitations, once it is necessary to assume/test a priori geometries for the sources, i.e. the method need geological information input.

This procedure is reliant on the geological model, so it is imperative to think about the geological problem being investigated and is also wise to remove any effects on the data that are already well understood, such as regional anomalies (Reid et al., 2014).

This interdependence between the method and the geological model is assured by the Structural Index (SI). This parameter specifies the source body geometry (Table 4.1) and needs to be chosen carefully otherwise the results may not be the expected: an SI too high could lead to overestimated depth solutions (Reid et al., 2014). Intermediate SI values (such as 0.5, frequently used in regional

interpretations of contact and faults) are also common, although the Euler's deconvolutions solutions are only approximations.

Table 4.1. Structural Index (SI) applied in Euler's deconvolution as a geological constraint. Adapted from (Reid et al., 2014).

Geological model	Magnetic Structural Index	Gravity Structural Index
Point, sphere	3	2
Line, cylinder	2	1
Thin sill or dyke	1	0
Contact of infinite depth extent*	0	N/A

*Special case developed by Reid *et al.* (1990) for the magnetic data.

For both gravity and magnetic data, the SI was chosen based on the geological information from the seismic profile, essentially structures that led to contrast zones, i.e. sills, dykes, faults, among others.

This deconvolution technique solves Euler's homogeneous equation, whose application to potential field data was first proposed by Thompson (1982):

$$(x - x_0)\frac{\partial F}{\partial x} + (y - y_0)\frac{\partial F}{\partial y} + (z - z_0)\frac{\partial F}{\partial z} = N(R - F) \tag{4.26}$$

Where (x_0, y_0, z_0) is the position of a gravity/magnetic source whose field F is detected at (x, y, z), R is the regional field of F and N (degree of homogeneity) is equivalent to the structural index (SI), which measures the rate of change with the distance of the field. Thus, Euler's deconvolution formulation requires not only the anomalies but also the spatial gradients (Reid et al., 2014).

This procedure operates on a data subset extracted using a moving window, in which the Euler's equation is solved (Gubbins and Herrero-Bervera, 2007). The choice of window size must account for the desired resolution, a stable numerical solution and the appropriate depth of investigation (Reid et al., 2014). It is also important to consider that the window should only represent the effects of a single source and also needs to be significantly greater than the line or grid spacing (Reid et al., 2014).

The method does not depend on the direction or magnitude of induced or remanent magnetisation, thus it is not necessary to apply to the RTP magnetic data (Reid et al., 1990). However it appears to work better on data after applying the magnetic pole reduction (Gubbins and Herrero-Bervera, 2007).

The Euler deconvolution maps (Figure 4.25, Figure 4.26) display the depth Euler solutions. However, considering the low confidence level in the values of depth solutions, the results will only be interpreted qualitatively, and not quantitatively.

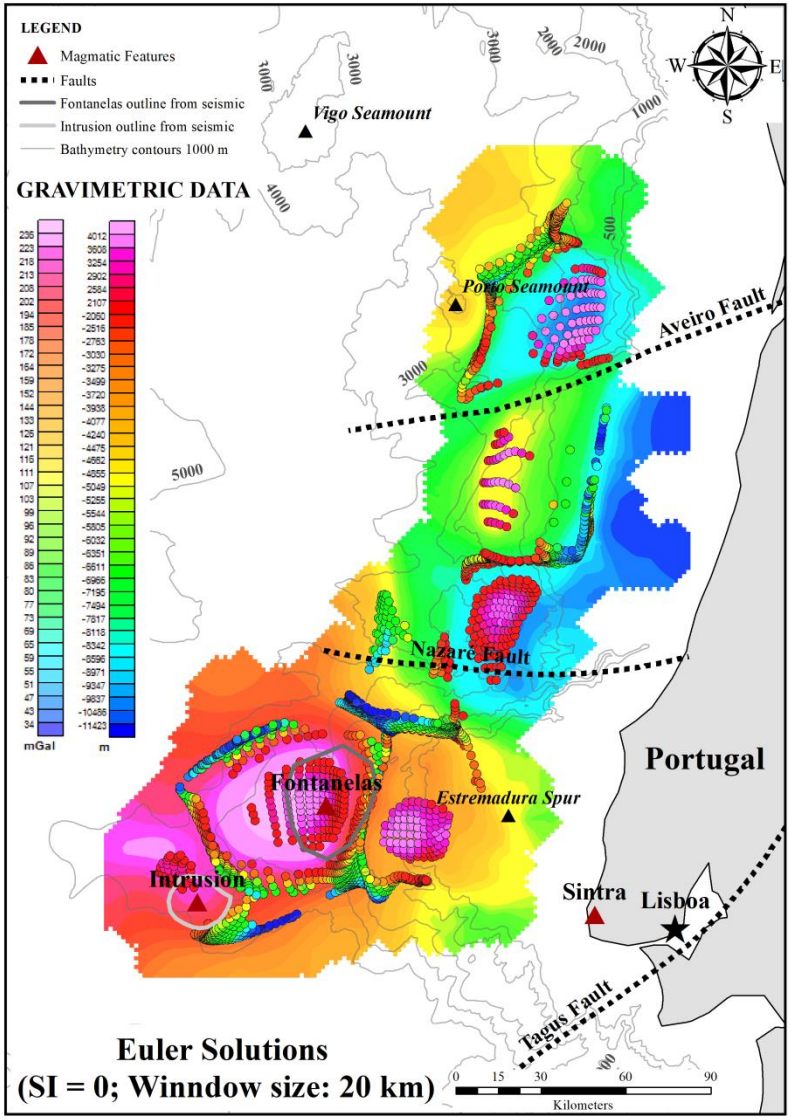

Figure 4.25. Euler solutions map of the gravity data, using a structural index of 0 (equivalent to sills and dykes structures) and a window size of 20 km.

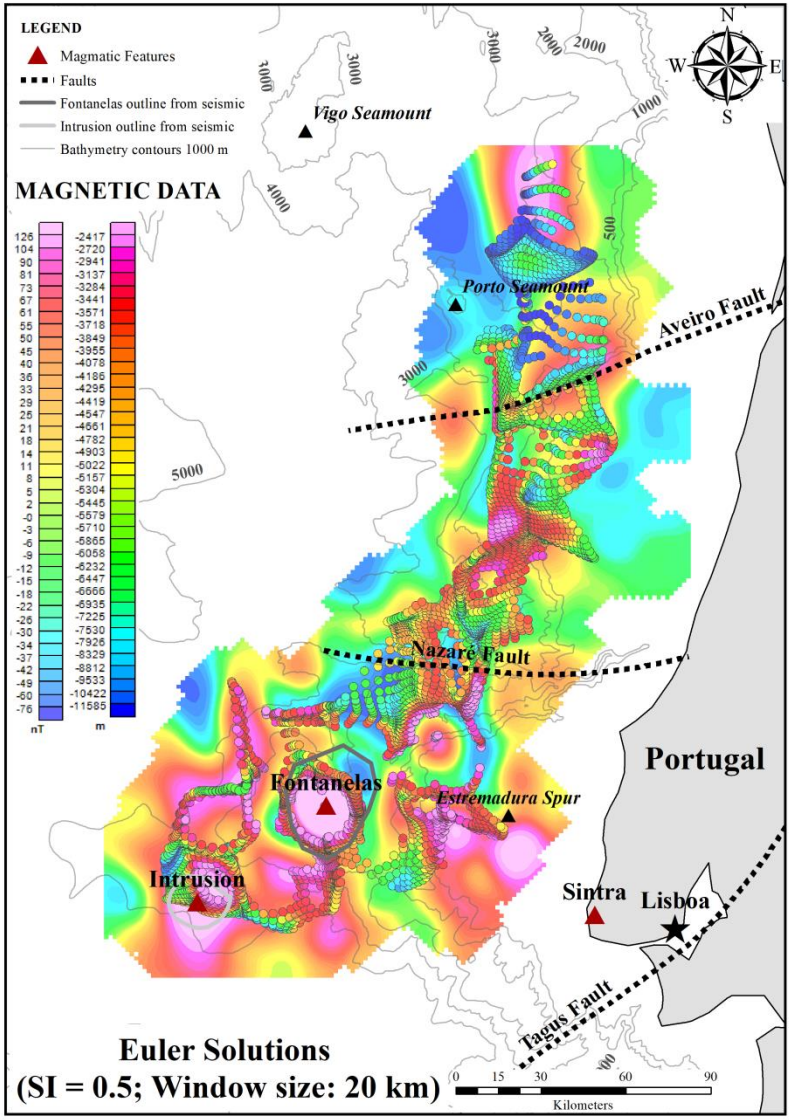

Figure 4.26. Euler solutions map of the magnetic data, using a structural index of 0.5 (equivalent to contrast zones, e.g. faults) and a window size of 20 km.

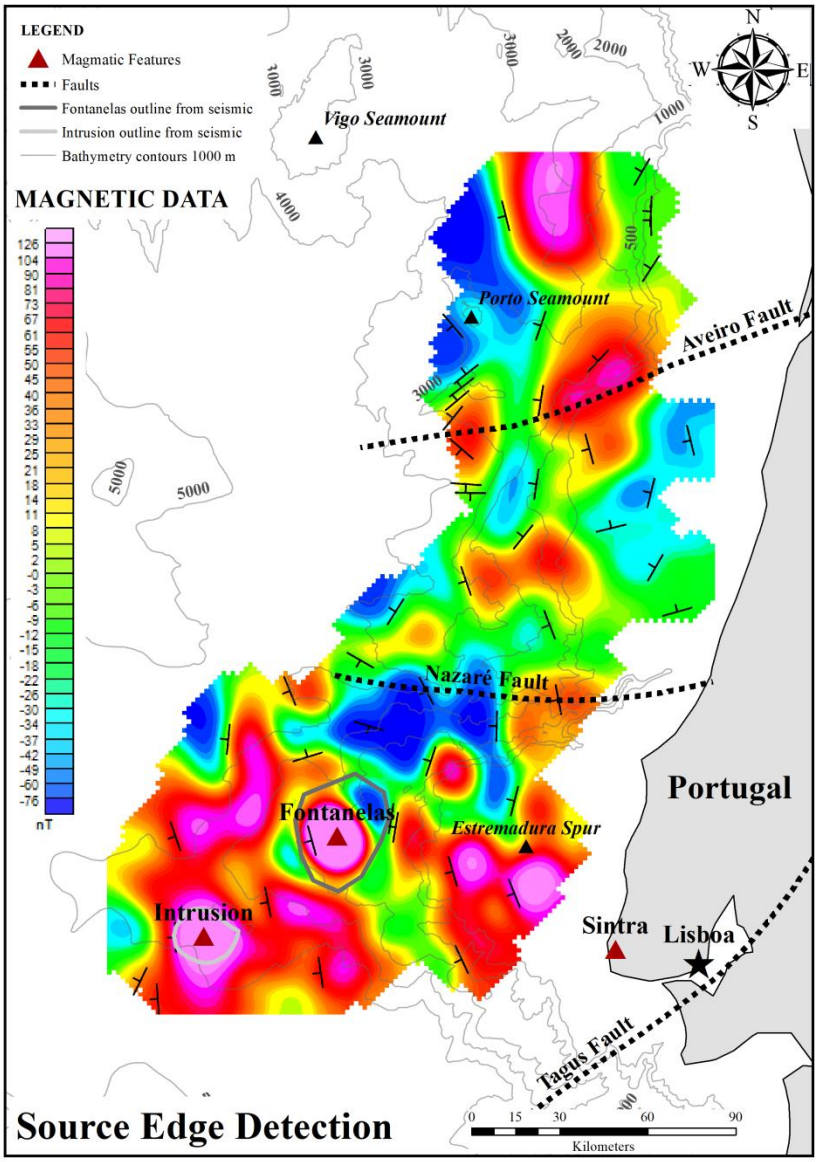

Figure 4.27. Source Edge Detection (SED) map of the magnetic data.

4.3.7.Source edge detection

There are several methods to detect and interpret the edge of the source bodies, many of them have already been mentioned above: analytic signal, tilt angle derivative, Euler deconvolution, among others.

The Oasis Montaj (Geosoft Inc.) program provides a GX (Geosoft eXecutable) that is also used to locate the approximate edges of source bodies from magnetic or gravity data, called Source Edge Detection (SED). This operation requires two input grids: (1) the reduced to pole for magnetic anomalies or Bouguer gravity or its residual grid for gravity anomalies and (2) the total horizontal derivative of the above-mentioned grid.

The SED uses the Blakely and Simpson (1986) method to find localised peaks in a grid. For each grid cell to be considered, the SED compares its value with the eight surrounding grid cells in four directions (x, y and both diagonals).

The source edge detection map (Figure 4.27) was performed only for the magnetic data and is displayed as symbols, which indicate the direction and inclination of the source bodies' edges.

4.4. Qualitative interpretation

The aim of qualitative interpretation is to characterise main regional geological features that are present on the West Iberia and, more significantly, the evidence of magmatism in the Estremadura Spur. This will be achieved through the correlation of geological and geophysical information through the analysis of the resulting maps from the signal enhancement techniques. The patterns and magnitude of the parameters will be considered in the identification of contrast regions (correspondent to geological domains) and the major tectonic structures in the region.

The main geological features that are possible to identify in the region include: 1) bathymetric features such as the Porto seamount and the Estremadura Spur, 2) the Aveiro, Nazaré and Tagus Fault Zones and 3) the two magmatic targets, namely the Fontanelas volcano and a buried magmatic intrusion. Considering that this is the first study to focus on this intrusion, it was decided to name it as Estremadura Spur Intrusion (ESI). Henceforward, the intrusion will be referred to as Estremadura Spur Intrusion or ESI.

The Estremadura Spur is fault bounded positive relief in the continental crust that stands out on the physiography of the continental platform of the West Iberian Margin. This is visually clear in the gravity data maps, namely the free air anomaly (Figure 4.1) Bouguer anomaly (Figure 4.2), regional anomaly (Figure 4.3) and upward continuation (Figure 4.21) maps, where the acceleration of gravity values are much higher in the Estremadura Spur zone.

The Fontanelas volcano is an enigmatic feature in the Estremadura Spur that reveals itself on bathymetry data (Miranda, 2010), which in fact is the outcropping expression of a buried volcanic edifice with more than 2500 m high (Pereira et al., 2017). Considering that volcano as an important bathymetric feature on the seafloor, and expressed as a major anomaly in the gravity maps, it controls almost all the gravity signal associated with the Estremadura Spur as it is evident in the Bouguer anomaly map (Figure 4.2). However, when the residual anomaly (Figure 4.4) is calculated this feature appears much more spatially constrained. Concerning the magnetic data, more specifically the RTP map (Figure 4.9), Fontanelas volcano presents itself as a positive anomaly with elliptical shape with the major axis approximately oriented NW-SE. In the horizontal derivative maps (Figure 4.11 to Figure 4.14), the outline of the volcano is also well defined, since it is in the transition between high and low gradient zones.

The Estremadura Spur Intrusion, one of the major targets of this study is unclear in the Bouguer and regional anomaly maps likely due to the strong regional signal and the sedimentary cover (1500-2000 m thick), which masks the overall signal. ESI only becomes clearly identifiable when the regional-residual separation is performed, specifically in the residual anomaly map (Figure 4.4). This magmatic feature stands out with an excellent match with the intrusion outline obtained from 3D seismic data interpretation. The analytic signal (Figure 4.17, Figure 4.18) and vertical derivative (Figure 4.15, Figure 4.16) maps also delimit the anomaly caused by the intrusion with outstanding precision. This also occurs in the tilt derivative maps, especially in the TDR magnetic map (Figure 4.24).

The Nazaré Fault (NF) is a major crustal feature on the West Iberian Margin, trending broadly in an east-west direction, and separates two lithospheric domains with a distinct thickness (Pereira et al., 2017). The influence of this fault is detected in almost all maps. However, the NF is more noticeable in the analytic signal of the magnetic data (Figure 4.18) and the horizontal derivative in the *y*-direction map in both gravity (Figure 4.13) and magnetic (Figure 4.14) data. It separates sectors with different gradient values, especially the ∂y of gravity data, where the southern part of the fault has smaller

values (-0.0028 mGal/m to -0.0013 mGal/m) and the northern part is characterised by higher values (-0.0003 mGal/m to 0.0003 mGal/m).

Another important tectonic lineament is the Aveiro Fault, located in the northern sector of the WIM. This feature is well defined on the horizontal derivative ∂y of the magnetic map (Figure 4.14), from which the lineament corresponding to the position of the fault zone is evidenced by an alignment of magnetic anomalies end up close to the fault. The Source Edge Detection map (Figure 4.27) also shows evidence of the presence of the Aveiro Fault with apparent dips extracted from the map suggesting dipping to NW. However, on the south sector the inclination is approximate to SW, suggesting a complex geometry for this transcurrent fault.

The Porto Seamount can also be imaged on the free air anomaly (Figure 4.1), Bouguer anomaly (Figure 4.2), RTP (Figure 4.9) and the tilt derivative (Figure 4.17, Figure 4.18) maps, characterised by a small, circular high in the seafloor and also expressed on the bathymetric contours.

The Source Edge Detection map (Figure 4.27) performed only for the magnetic data reveals the presence of a structure broadly N-S oriented and inclined to SW, located between the two magmatic features: the Fontanelas volcano and the intrusion. This could correspond to a minor fault or some dyke/sill structure.

There is also a noteworthy structural feature, south of the Aveiro Faults that is evident in the Bouguer anomaly map (Figure 4.2) broadly oriented N-S. This feature is also recognized in other maps, such as the residual anomaly (Figure 4.4), RTP (Figure 4.9) maps and the analytic signal (Figure 4.17) and Euler solutions (Figure 4.25) maps of the gravity data. However, it does not match any clear geological or bathymetric feature.

Chapter 5: 2.5D modelling and quantitative interpretation of potential field data

Building on the regional analysis of the potential data through the application of several signal enhancement techniques, in this section a quantitative interpretation method (2.5D modelling) is presented in order to produce a physical model that allows characterising the evidences from 3D seismic imaging, which can match the regional geological context.

Modelling of potential field data can be performed either individually or jointly. For the purpose of better constraining the geological features to be modelled within the 3D seismic survey, individual gravity and magnetic models were created independently and later compared for consistency of results.

As referred in previous chapters, 2.5D modelling of potential field data needs to be constrained in order to produce meaningful geological results. Accordingly, the geometry/structure of the 2.5D model was constrained based on the interpretation of a random 3D seismic line, whereas the density and susceptibility were based on values from: 1) confidential reports, 2) published scientific literature and/or 3) rock's properties standard values.

In this chapter, the results of the gravity and magnetic data 2.5D modelling will be presented and interpreted, combining a comprehensive geophysical and geological approach.

5.1. 2.5D modelling results

In this section, it will be separately presented the results of 2.5D gravity and magnetic quantitative data modelling. This approach was achieved by modelling different scenarios with increasing level of complexity in order to obtain a satisfactory fit between the overall geological insights from a random 3D seismic reflection data and the outcome from the geophysical data modelling.

The modelling process started with the building of an initial model for gravity and magnetic data, assuming simple geometry and basic reference values. The main blocks were defined based on horizontal contrasts observed in the seismic profile. However, through the modelling process it was necessary to increase the complexity of the model by partitioning the major blocks, supported by the seismic information, namely variations in the seismic facies throughout the profile (Figure 1.1). These variations are explained by the existence of geological contrasts, mainly due to faults (vertical or high angle), which places different geological materials side by side with, consequently, different acoustic behaviour, giving rise to different seismic facies. The final model with the best fit is presented latter and briefly discussed.

The seismic interpretation (Figure 1.1b) also allows the classification of seismic units into geological units (Tertiary, Jurassic, Jurassic-Cretaceous, Fontanelas, and intrusion). The knowledge of these geological units is an important and indispensable aid to characterize the estimated age of the blocks and, consequently, its lithology.

5.1.1. Gravity data

Gravity modelling was carried out by using the Bouguer anomaly data (Figure 4.2), already corrected using a density of 2.3 g/cm^3. Therefore, in the modelling process, absolute values of density

were used as input. The air block was set to a zero density, while the water column block was defined with a 1.03 g/cm^3 density.

It is important to mention that the gravity models presented in this section, are a segment of an extended profile (Annexe 3) with the same orientation as the A-A' profile (Figure 4.2), though extended to the edges of the acquisition area. Therefore, the error associated with the fit of those model does not concern only the visible sector of the profile, but it encompasses the fit throughout the extended profile (Annexe 3).

Increasing the extension of the original profile was necessary because, during the initial stages of the modelling process, the fit between the anomalies at the edges of the profile was only accomplished if the densities in the westernmost and easternmost sectors were very high (*high density zone*, Figure 5.2) and very low (*low density zone*, Figure 5.2), respectively. The extended profile (Annexe 3) allowed understanding that, to the east, there is an abrupt decrease of the observed anomaly, confirming the necessity of using very low-density values in this sector. However, this was not possible to conclude for the high-density sector, because there is no data for the SW edge of the profile that may allow the determination of the reason for the high-density values.

Table 5.1. Chosen densities for each block of the initial gravity model (see Figure 5.1). The references mention the published scientific literature from where the density values were taken, and, in the case of the Fontanelas volcano and the Estremadura Spur Intrusion (intrusion), also include the studies that allowed defining its possible lithology. See annexe 4, for the table of densities adapted from Telford et al. (1990).

Block's name	Possible lithology	Density (g/cm^3)	References
Tertiary	Sedimentary	2.2	Confidential reports
Jurassic – Cretaceous	Sedimentary	2.4	Confidential reports
Jurassic	Limestone	2.55	Telford et al., 1990
Fontanelas volcano	Basalt	2.75	Miranda et al., 2010 Telford et al., 1990
Intrusion	Granite	2.65	Escada et al., 2019 Ramalho et al., 1993 Telford et al., 1990
Basement	Crystalline	2.7	Confidential reports

Based on the regional lithostratigraphy analogues, the Tertiary, J-K and Jurassic are predictably sedimentary blocks. For the initial gravity model (Figure 5.1) the densities for the Tertiary, Jurassic – Cretaceous (J-K) and basement blocks were set based on confidential reports (which includes well data information) undertaken on the region. The Jurassic was interpreted in the seismic profile as a syn-rift block (Figure 1.1) and, according to the lithostratigraphic table (Figure 2.2), it likely corresponds to a limestone. The density of the Fontanelas volcano was chosen based on published data by Miranda et al. (2010) that conclude that this magmatic feature is constituted dominantly by altered alkaline basalts.

Concerning the Estremadura Spur Intrusion (intrusion block, Table 5.1), as it is described here for the first time, there is no evidence of its geochemistry or nature. Although based on the earth's magnetic anomaly and seismic profiles, this offshore intrusion presents an area of approximately 280 km^2, elliptical shape broadly oriented W-E and intrudes Jurassic and Cretaceous depositional sequences (Escada et al., 2019). Its shape and areal extent are similar to the onshore Sintra massif (Ramalho et al., 1993; Terrinha et al., 2017, 2003). Consequently, its density was chosen based on the similarities with the Sintra massif, which is characterised by the predominance of granitic facies (Ramalho et al., 1993). Based on this information, and the range of density values for granites (Annexe 4), a density of 2.65 g/cm^3 was used in the initial gravity model (Figure 5.1).

2D Modeling (Simplest Model)

Gravimetric data

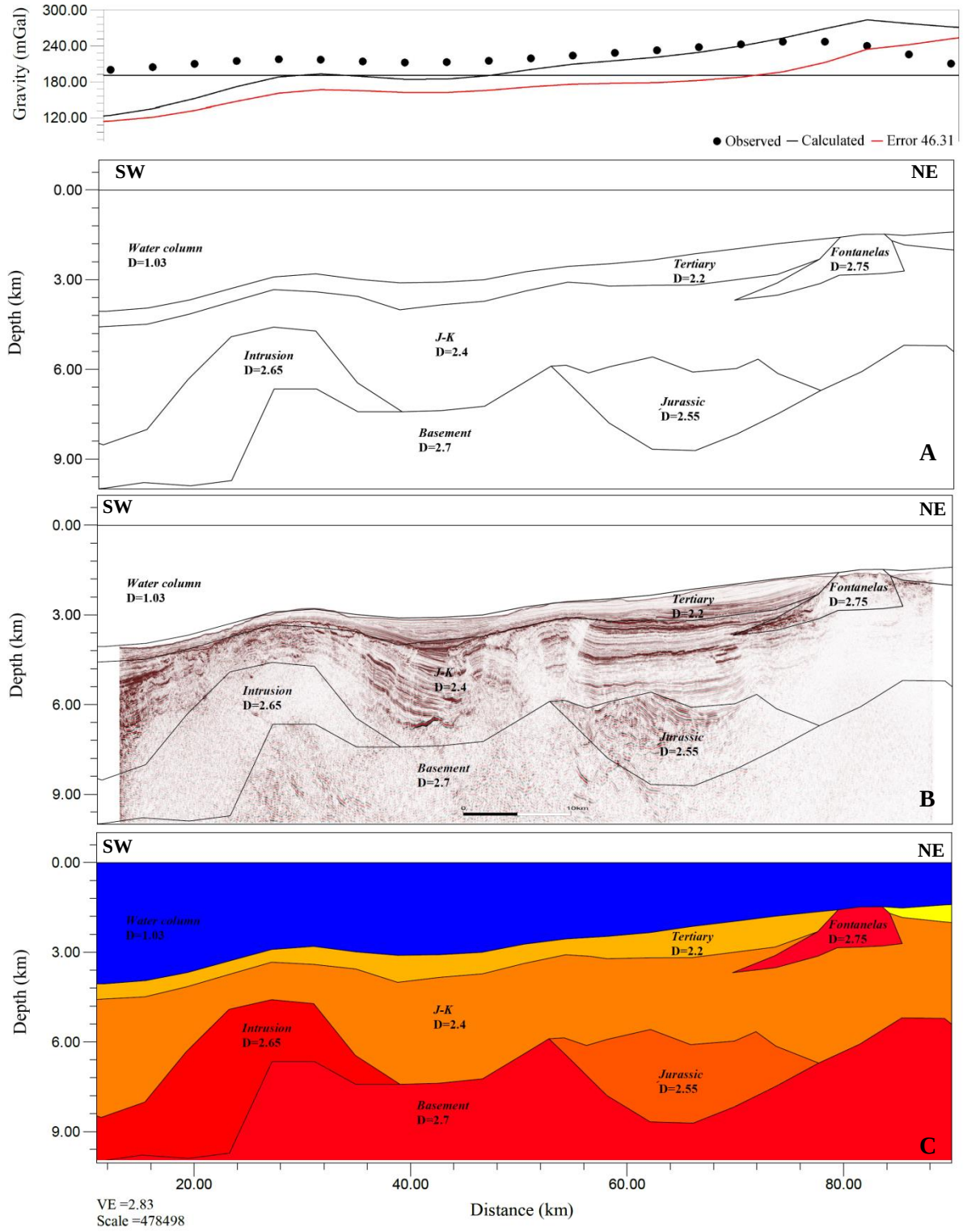

Figure 5.1. Initial gravity 2D model: A) panel with the density values and the structure of each block, B) panel with the seismic background image, the density values and structure of each block and C) the colour of each block it is in accordance with a density's colour scale. The location of the model profile (A-A') is presented in Figure 4.2, over the Bouguer anomaly map.

The chosen densities for the initial gravity model (Figure 5.1) are within the range [2.2, 2.75] g/cm^3 and are summarised in Table 5.1. In the initial model (Figure 5.1) the calculated anomaly over the Fontanelas volcano resulted in overestimated values, whereas, for the intrusion, the initial calculation was underestimated. The main objective of the subsequent 2.5D modelling is to interactively adjust these values until there is a satisfactory fit between the calculated and observed anomalies.

The results of the final 2D gravity modelling are presented in Figure 5.2. When comparing the initial and final models, the differences observed reflect the adjustments to both the structure and density of the depositional packages and igneous bodies. Nevertheless, the fit between the observed and calculated gravity anomalies is very good in the overall extent of the profile, highlighting the fact that the fit of both targets (intrusion and volcano) and background structures has been done with the same level of adjustment.

The range of density values in the final model is wider compared with the initial model, [2.0, 2.9] g/cm^3 and the main alterations concerning the density values are:

1) The density of the Tertiary and basement blocks decreased, in order to eliminate a generalized overestimation tendency of the calculated anomaly.
2) The density of the Fontanelas seamount in contact with the seawater decreased by 0.3 g/cm^3, as well as in its buried section, although, with a smaller decrease of 0.15 g/cm^3. Contrarily, the density of the intrusion increased by 0.5 g/cm^3.
3) In the J-K block, in addition to the blocks' partitioning, the overall density increased in most of the blocks, and especially, in the horizontal block with 2.75 g/cm^3 of density.
4) The lower (2.0 g/cm^3) and higher (2.9 g/cm^3) density values of the blocks correspond to the high- and low-density zones in the western and eastern sectors, respectively.

Table 5.2. Density values for each block of the 2D gravity model and its possible interpreted lithology.

Block's name	Density (g/cm^3)	Possible lithology
Tertiary	2.0	Sedimentary
J-K (1)	2.32	Sedimentary
J-K (2)	2.65	Sedimentary
J-K (3)	2.6	Sedimentary
J-K (4)	2.38	Sedimentary
J-K(5)	2.47	Sedimentary
High density zone	2.9	Sedimentary + magmatic
Low density zone	2.0	Sedimentary
Horizontal block	2.75	Sedimentary + magmatic
Jurassic	2.57	Limestone
Fontanelas	2.45	Altered basalt
Buried Fontanelas	2.6	Basalt
Intrusion	2.7	Granite or gabbro
Basement	2.6	Crystalline

Note: J-K blocks are numbered from NW to SE.

Based on the results from gravity modelling (Table 5.2) the Tertiary, J-K and low-density zone blocks are most likely to have a sedimentary nature. On the other hand, the high-density value (compared with the previous blocks) of the high-density zone and the horizontal blocks, may indicate a magmatic contribution. Concerning the high-density zone, this contribution is probably from the intrusion, and the magmatic nature of the horizontal block is possibly associated with the Fontanelas volcano, due to the proximity of both blocks with the respective magmatic targets.

2D Modeling

Gravimetric data

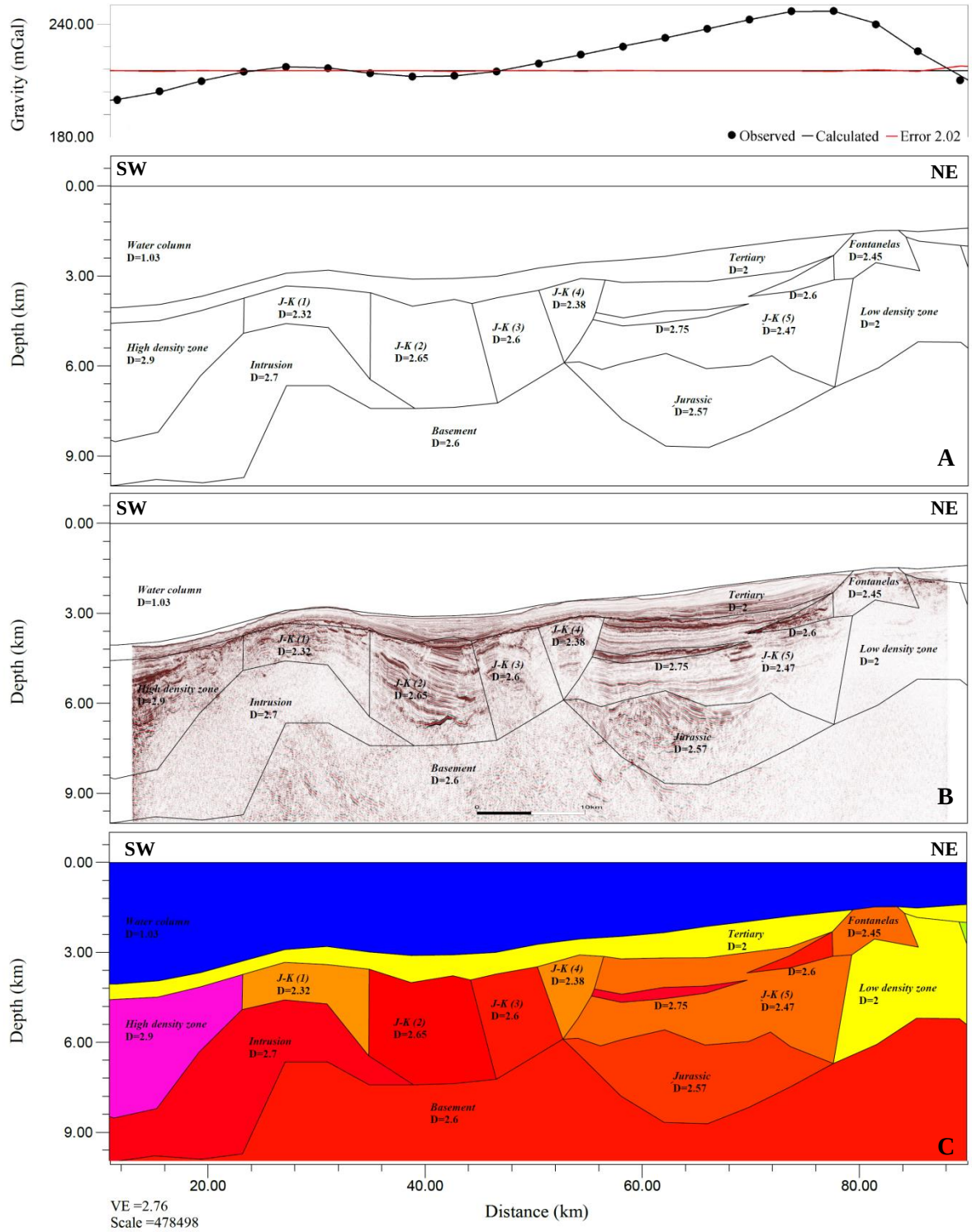

Figure 5.2. Final gravity 2D model: A) panel with the density values and the structure of each block, B) panel with the seismic background image, the density values and structure of each block and C) the colour of each block it is in accordance with a density's colour scale. The location of the model profile (A-A') is presented in Figure 4.2, over the Bouguer anomaly map.

The density of the Fontanelas volcano is smaller than the initial specified density, which can possibly indicate a change in its basaltic original composition, most likely associated with alteration, due to its direct contact with the seawater. Although its buried sector, also has a minor density, it is still pointing to a basaltic nature (Annexe 4). On the contrary, the Estremadura Spur Intrusion has a higher density value, compared with the density of the initial model, which increase the spectrum of possible lithologies that may be associated with this intrusion: granitic or gabbroic magmatic nature. The density values of each block, as well as its possible lithology, are summarised in Table 5.2.

5.1.2.Magnetic data

The modelling of magnetic data is more complex and less straightforward compared with the modelling of gravity data. The main reason it is the dependence of the magnetic anomaly on several factors, such as the inducing magnetization (proportional to susceptibility), remanent magnetization (related with its magnetic history), the characteristics of the magnetized material (i.e. the type and amount of magnetic minerals in the rocks) and the direction of the geomagnetic field. These factors ultimately influence the shape, amplitude and location of the anomaly. The dependence of magnetic data on the field's direction can be overcome by using the magnetic data reduced to pole since it corrects the shape of the anomaly and relocates it above the causative body. Thus, the 2D magnetic modelling was performed with RTP data (Figure 4.8). In the case of the magnetic data, both air and water blocks are associated with zero susceptibility.

As referred in previous chapters, the parameters of the Earth's magnetic field must be specified in order to calculate the magnetic response of the model. Considering RTP data were used, it was assumed an inducing field with a magnitude of 43765 A/m (calculated through the IGRF model), 90º of inclination (vertical, Figure 4.10) and 0º of declination.

Table 5.3. Chosen susceptibilities for each block of the initial magnetic model (see Figure 5.3). The references mention the published scientific literature from where the susceptibility values were taken, and, in the case of the Fontanelas volcano and the Estremadura Spur Intrusion (intrusion), also includes the studies that allowed defining its possible lithology. See annexe 5, for the table of susceptibilities adapted from Telford et al. (1990).

Block's name	Possible lithology	Susceptibility (SI)	References
Tertiary	Sedimentary	0	Confidential reports Telford et al., 1990
Jurassic – Cretaceous	Sedimentary	0	Confidential reports Telford et al., 1990
Jurassic	Limestone	0	Telford et al., 1990
Fontanelas volcano	Basalt	0.07	Miranda et al., 2010 Telford et al., 1990
Intrusion	Granite	0.025	Escada et al., 2019 Ramalho et al., 1993 Telford et al., 1990
Basement	Crystalline	0.01	Neres et al., 2018

As in the gravity model, the structure of the initial magnetic model (Figure 5.3) was defined as the simplest structural model based on the seismic profile interpretation, and the susceptibility values were based on the same assumptions made for the initial gravity model. Therefore, the Tertiary, J-K and Jurassic blocks are predictably sedimentary blocks and, consequently, it is expected to have very low susceptibility.

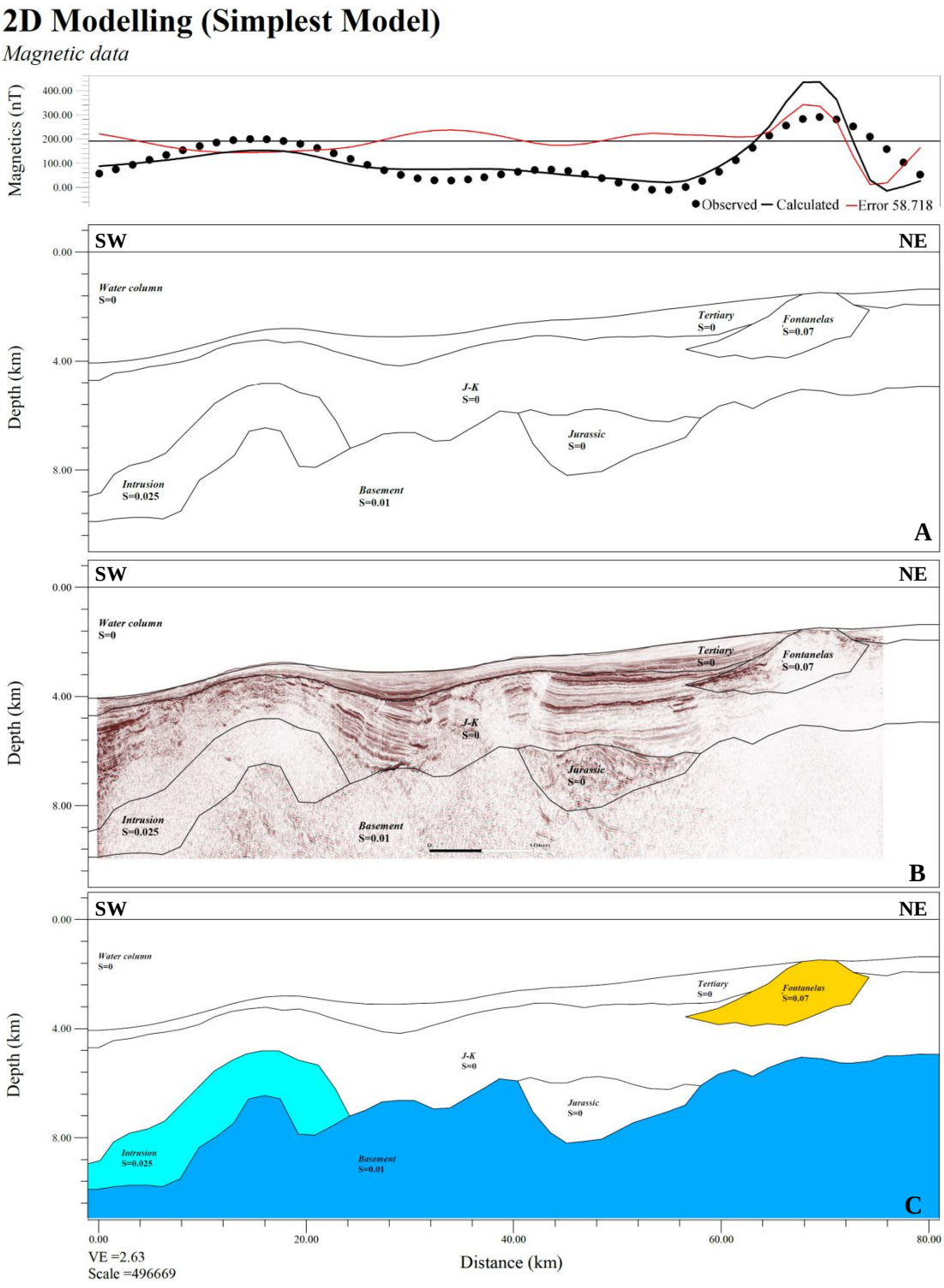

Figure 5.3. Initial magnetic 2D model: A) panel with the susceptibility values and the structure of each block, B) panel with the seismic background image, the susceptibility values and structure of each block and C) the colour of each block it is in accordance with susceptibility's colour scale. The location of the model profile (A-A') is presented in Figure 4.8, over the reduced to pole (RTP) magnetic map.

For the Fontanelas volcano and the Estremadura Spur Intrusion, it was considered a basaltic and granitic nature, with susceptibility values of 0.07 SI and 0.025 SI, respectively. Accordingly, for the initial magnetic model (Figure 5.3) the susceptibilities are within the range [0, 0.07] SI. This information is summarised in Table 5.3.

Similarly to the analysis for gravity modelling, the calculated anomaly over the Fontanelas volcano is overestimated relative to the observed anomaly, and the anomaly over the intrusion is underestimated (Figure 5.3).

The results of the final 2D magnetic modelling are presented in Figure 5.4. The fit between the calculated and observed anomalies in the final magnetic model is very good with an error of 2.958.

Comparing the initial and final models, besides the differences in the blocks' partitioning, as a natural consequence of the increased complexity as the modelling progresses, the range of susceptibility values is also wider [0, 0.08] SI. Except for the Tertiary and basement blocks, which susceptibility values remained equal, the main differences are:

1) The J-K susceptibility values range from 0 – 0.08 SI. However, the upper limit (0.08 SI) is considered an exception associated with the horizontal block. The same occurred in the gravity model, where this block exhibits a higher density compared with the overall J-K block. However, in the magnetic data, this horizontal block does not have a constant susceptibility throughout its extension: in the western zone, it presents a susceptibility of 0.08 SI, whereas in the eastern zone the value is 0.02 SI.
2) Concerning the Fontanelas and the intrusion, in the final magnetic model, the same susceptibility (0.05 SI) was achieved for both magmatic bodies. However, the buried sector of the Fontanelas has the expected susceptibility, equal to the initial model (0.07 SI).

Table 5.4. Susceptibility values for each block of the 2D magnetic model and its possible interpreted lithology.

Block's name	Susceptibility (SI)	Possible lithology
Tertiary	0	Sedimentary
J-K (1)	0.02 [(1)]	Sedimentary (+ Magmatic)
J-K (2)	0	Sedimentary
J-K (3)	0.001	Sedimentary
J-K (4)	0.011	Sedimentary
J-K (5)	0.001	Sedimentary
J-K (6)	0	Sediments
J-K (7)	0.01	Sedimentary
J-K (8)	0	Sedimentary
J-K (9)	0.038	Sedimentary (+ Magmatic)
Horizontal block (1)	0.08	Magmatic
Horizontal block (2)	0.02	Sedimentary (+ Magmatic)
Jurassic	0	Sedimentary
Unknown	0.03 [(2)]	Evaporites
Fontanelas	0.05	Altered basalt
Buried Fontanelas	0.07	Basalt
Intrusion	0.05	Granite, diorite or gabbro
Basement	0.01	Crystalline

Note: The J-K blocks are numbered from NW to SE.

[(1)] Block with remanent magnetization: (a) magnitude = 1, (b) inclination = -90º and (c) declination = 175º

[(2)] Block with remanent magnetization: (a) magnitude = 1, (b) inclination = -45º and (c) declination = 175º

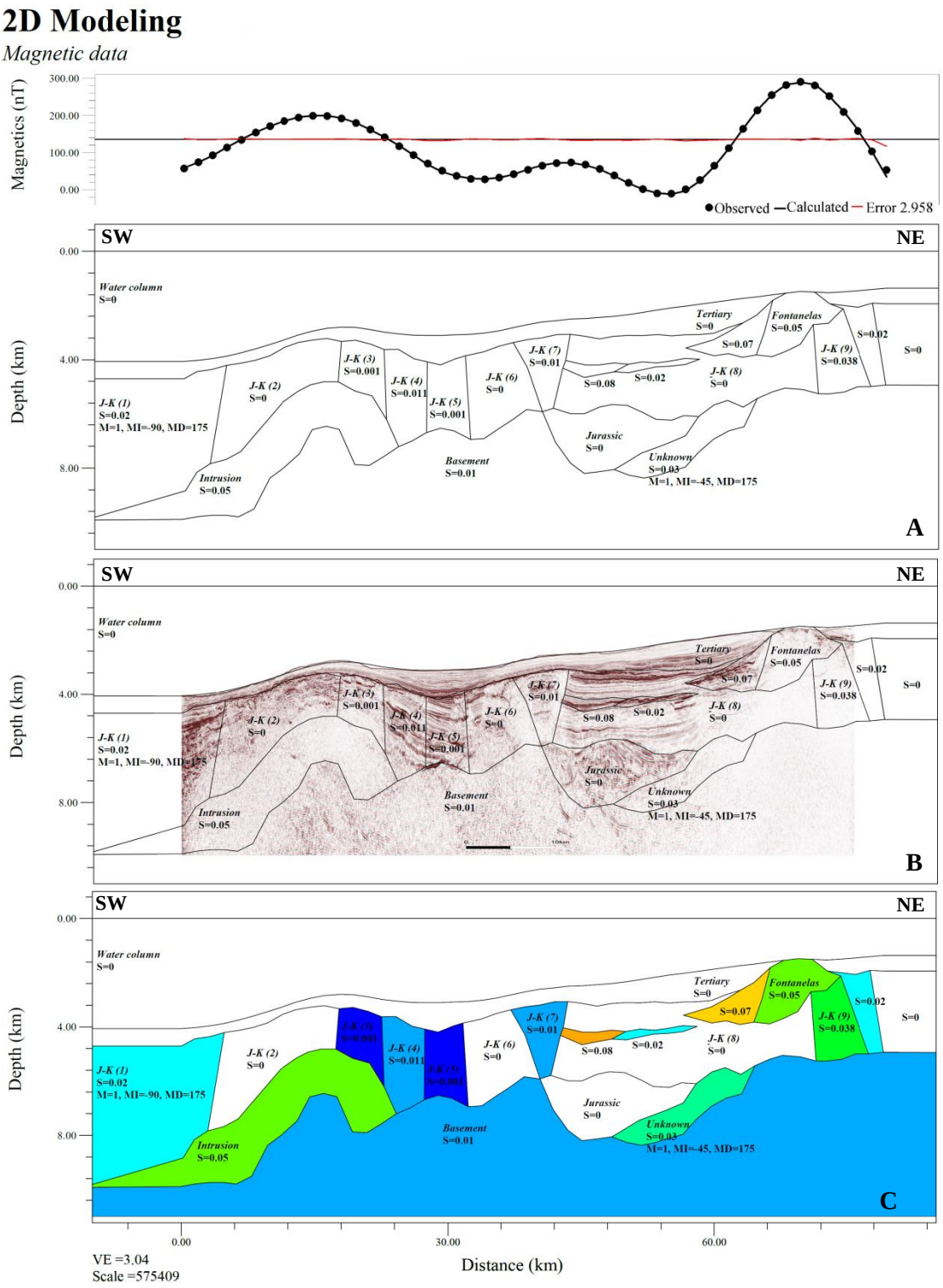

Figure 5.4. Final magnetic 2D model: A) panel with the susceptibility values and the structure of each block, B) panel with the seismic background image, the susceptibility values and structure of each block and C) the colour of each block it is in accordance with susceptibility's colour scale. The location of the model profile (A-A') is presented in Figure 4.8, over the reduced to pole (RTP) magnetic map.

In this study, it was considered the presence of remanent magnetization associated with the westernmost J-K block (J-K (1)) and in the block below the Jurassic's block (Figure 5.4). Adding a remanent magnetization to the model was necessary because, in the initial modelling iterations, the fit between the calculated and observed anomalies was only achieved with negative values of susceptibility. The presence of such values is unlikely to occur, although not impossible due to the presence of some minerals called diamagnetic (such as quartz and copper). However, in magnetic surveys, the diamagnetism is insignificant. Therefore, the high negativity values (~ -0.07 SI) obtained in the first modelling iterations were impossible. In these situations, negative values of susceptibility could be indicative of reversely magnetised material, where the remanent magnetization vector is opposed to the Earth's magnetic field. Based on this assumption, the declination parameter of the remanent magnetization vector was set to 175º. This angle corresponds to the opposite angle of the magnetic field declination at the time of the acquisition (2008), calculated with the IGRF model (-4º). Without other supporting evidences, the magnitude and inclination values were chosen to fit the data.

Based on the results from magnetic modelling, the Tertiary, the Jurassic and all the J-K, except J-K (1) and (9), blocks point to a sedimentary nature. The J-K (1) and (9) blocks, have a higher susceptibility, which can be explained by the addition of magmatic material. This is supported by the proximity of these blocks with the intrusion and the volcano, respectively. The horizontal block was subdivided into two blocks with very different susceptibilities. The horizontal block (1) is clearly magmatic, due to its very high susceptibility, however the horizontal block (2) has the same susceptibility of the J-K (2) block, which can also indicate the presence of magmatic material interlayered with sedimentary material.

The block below the Jurassic was only modelled with the magnetic data, and it is suspected to be an evaporitic unit, based on the chaotic nature of the reflections, noise and limited resolution of 3D seismic data on this interval.

Concerning the Fontanelas volcano, its lower susceptibility compared with the expected value, indicates the presence of an alteration possibly due to the seawater-rock contact. While the buried sector, has the expected susceptibility for basalt rocks, indicating that this could possibly be its original nature. The Estremadura Spur Intrusion (ESI) has a higher susceptibility value, which can correspond to a wide possibility of intrusive magmatic lithologies: granite, diorite or gabbro. The susceptibility values of each block, as well as its possible lithology, are summarised in Table 5.2.

5.2. Integrated quantitative interpretation of potential field models

In this section, a comprehensive interpretation of the gravity and magnetic 2.5D modelling results is presented, based on the overall geological context. The information that can be extracted from the seismic profile is already incorporated on both gravity and magnetic model's structure/geometry.

Concerning the Tertiary package, it is the most superficial unit and is defined by a low density (2.0 g/cm^3) and susceptibility (0 SI). These values are characteristic of a sedimentary rock, possibly with a low degree of consolidation, considering it was the last unit to be deposited. This information is confirmed by the seismic reflectors, which are sub-horizontal and subparallel. The Tertiary and the J-K blocks are separated by the Base Tertiary Unconformity (BTU).

The intermediate J-K block is the most complex block of the profile, being subdivided into minor blocks. Specifically, the low-density zone identified in the gravity model with a density of 2.0 g/cm^3 (Table 5.2). In the magnetic model, this block widely corresponds to the J-K (9) block with a susceptibility of 0.038 SI (Table 5.4). As previously referred, the density value indicates a sedimentary

nature, although its susceptibility is a high value in order to represent sedimentary rocks. However, this low-density value is associated with a low-density tendency in NE sector of the extended profile (Annexe 3), which suggests the presence of a sedimentary basin, confirmed by the regional maps of free air (Figure 4.1) and Bouguer (Figure 4.2) anomalies. On the other hand, being located over the Fontanelas volcano the higher susceptibility suggests the presence of feeding magmatic conducts, which was not detected by the gravity data modelling.

The high density and high susceptibility of the horizontal block is one of the most intriguing units, marked by high-amplitude reflectors. In this block, there are some reflectors which follow the subparallel tendency, however, there are others that cross the reflectors, including, one high-amplitude sub-vertical reflector underneath this horizontal block. The subparallel high-amplitude reflectors present in this block could have a sedimentary nature, possibly limestone interlayered with sandstone, due to the difference in amplitude between this block and the adjacent J-K block. The cutting reflectors probably have a magmatic nature, in the form of sills (tabular structures, where the horizontal dimension is longer than the vertical) or dykes (tabular structures, where the vertical direction is longer than the horizontal), such as the sub-vertical reflector present below the horizontal block. This sills and dykes complex could be linked to the Fontanelas volcano.

In both gravity (Figure 5.2) and magnetic (Figure 5.4) models, the Fontanelas volcano is subdivided into two sectors, one of which is in contact with the seawater. The first sector has a density of 2.45 g/cm^3 and susceptibility of 0.05 SI, while the buried sector has a higher density of 2.6 g/cm^3 and susceptibility of 0.07 SI.

As referred above, the nature of the Fontanelas volcano was assigned to an alkaline basalt by Miranda et al. (2010), however, these authors also reported substantial alteration characterised by vesicular basaltic rocks (mostly correspondent to pillow lavas fragments) with iron and manganese oxide caps. This alteration could justify the low density and susceptibility values associated with the water-rock contact zone, while the buried sector has the expected values for the Fontanelas volcano, confirming its original basaltic nature. Concerning its geometry, this volcano was modelled with an, approximately, triangular shape, with a more extensive southern flank, localized at greater depths, compared with the northern flank. The depth of the base of the volcano in the gravity model is between 3-3.8 km, while in the magnetic model is between 2.6-4 km.

Regarding the Estremadura Spur Intrusion, located at the southwest edge of the 2D model profile, the density (D=2.7 g/cm^3) and susceptibility (S=0.05) values are higher than initially considered (D=2.65 g/cm^3 and S=0.025). In both gravity and magnetic models, there was an underestimation of the calculated anomaly over the intrusion which predicted the increase of both parameters. Combining both gravity and magnetic modelling results, the intrusive nature of the ESI may be granitic or gabbroic. Concerning its geometry, it was initially thought to be a batholith, however, the final modelling results likely indicate a laccolith, due to its sheet-like structure, while the batholith usually has a “bubble shape”. The depth of the top of this intrusion is at 4.8 km, while the base of the northern flank is at 8 km deep, for both gravity and magnetic models. The depth of the southern flank cannot be determined because, from the 9 km onwards, seismic data no longer exist to determine with certainty the depth of the base of the southern flank.

Subsequently to this joint analyses and interpretation of both gravity and magnetic models, it is possible to establish the geological material which constitutes the major blocks: 1) Tertiary: low-consolidated sediments, 2) Jurassic – Cretaceous: sedimentary rocks punctuated with magmatic rocks, 3) Jurassic: chemical sedimentary rocks (limestone), 4) Basement: crystalline rocks, 5) Fontanelas volcano: basaltic rock, with some degree of alteration and 6) Estremadura Spur Intrusion: granite or gabbro.

Chapter 6: Discussion

In previous sections, a qualitative analysis of potential field data was performed based on signal enhancement techniques. This analysis focused on the interpretation of the main geological features of the region under study, namely the Fontanelas volcano and the Estremadura Spur Intrusion (ESI), which constitute the two targets of this study. Overall, the gravity and magnetic anomaly associated with the ESI produces a nearly circular shape, confirming its outline from the seismic data. Whereas the gravity anomaly of the Fontanelas volcano is more diffuse than the one from the ESI, the magnetic anomaly of the Fontanelas volcano it is much better defined by an approximately circular geometry. Both targets have a strong geophysical signal, being distinguished from other regional features, indicating its importance on the West Iberian Margin, but more significantly in the Estremadura Spur.

Subsequently, a more detailed analysis was performed through 2.5D modelling of the potential field data, over a random seismic line across the centre of the intrusion and the southern flank of the Fontanelas volcano. In this section, the results of this approach will be discussed in terms of the geometry and possible magmatic nature of the Fontanelas volcano and the Estremadura Spur Intrusion.

Table 6.1 shows the modelling results, namely the density and susceptibility values obtained for the Fontanelas volcano (seawater-rock contact zone and buried sector) and for the Estremadura Spur Intrusion, as well as the interpreted lithologies based on these values.

Table 6.1. Density and susceptibility values obtained through the 2.5D modelling of the potential field data, as well as the possible lithologies attributed to the targets.

Target	Density (g/cm^3)	Susceptibility (SI)	Interpreted lithology
Fontanelas contact zone	2.45	0.05	Altered basalt
Buried Fontanelas	2.6	0.07	Basalt
Estremadura Spur Intrusion	2.7	0.05	Granite or gabbro

The Fontanelas volcano is characterised by an overall triangular shape, with a longer and deeper southern flank, as it is possible to observe this in both gravity (Figure 5.2) and magnetic (Figure 5.4) models, presented in the previous section. According to the density and susceptibility values (Table 6.1) determined for its buried sector (not in contact with the seawater) this was interpreted as a basalt. The lower density and susceptibility associated with the seawater-Fontanelas contact zone was suspected to be a result of the alteration of the basaltic rock. This interpretation is supported by the results of Miranda et al. (2010).

Regarding the Estremadura Spur Intrusion, the conclusions are not as straightforward, because this study comprises the first description of this magmatic feature. According to its similarities with the Sintra massif and the interpretation of the seismic it was initially assumed a granitic nature and a batholith shape for the ESI. The final models show the geometry of the ESI as being more similar to a laccolith than a batholith. According to the density and susceptibility values, two possible lithologies were associated with the ESI: granite and gabbro (Table 6.1). The magmatic nature of the ESI will be discussed based on analogue magmatic features, namely the Sintra (Terrinha et al., 2003) and Sines (Ribeiro et al., 2013) outcropping massifs, the Foz da Fonte sill (Neres et al., 2014) and the offshore buried Guadalquivir-Portimão intrusion (Neres et al., 2018).

Table 6.2. Density, susceptibility and lithology for several igneous bodies offshore and onshore the Iberia. The density and susceptibility values for the Sintra and Sines massifs and the Foz da Fonte sill were obtained through rock sample measurements, whereas the Guadalquivir-Portimão Bank values are referent to modelling results. All these igneous bodies are related with the Late Cretaceous magmatic cycle.

Igneous bodies	Lithology	Density (g/cm^3)	Susceptibility (SI)	References
Sintra	Granites	2.55	0.000039	Terrinha et al. (2003)
Sintra	Gabbros	2.76	0.07208	Terrinha et al. (2003)
Sines	Gabbros	-	0.01-0.1	Ribeiro et al. (2013)
Sines	Mafic dykes and diorites	-	< 0.001	Ribeiro et al. (2013)
Foz da Fonte sill	Not identified	-	0.03 – 0.067	Neres et al. (2014)
Guadalquivir-Portimão Bank	Not identified	2.9	0.05	Neres et al. (2018)

Terrinha et al. (2003) conducted a gravity study and a magnetic susceptibility analysis on the Sintra massif (~ 82-75 Ma). The mean densities obtained for each of the facies associated with this magmatic body were 2.55 g/cm^3 for the granitic facies, 2.56 g/cm^3 for the syenitic facies and 2.76 g/cm^3 for the gabbroic facies. Concerning the magnetic susceptibility, the syenitic and granitic facies showed a mean susceptibility of 0.000039 SI, whereas the gabbroic facies were characterised by a mean susceptibility of 0.07208 SI.

Ribeiro et al. (2013) carried out a paleomagnetic analysis of the Sines massif (~ 76 Ma), obtaining the highest values of magnetic susceptibility, K=0.01-0.1 SI, for the gabbros and subvolcanic breccias, and the lowest ones, K < 0.01 SI, for the metasediments, mafic dykes and diorites.

In both studies, the gabbro yields to higher values of density and susceptibility, compared with the other analysed lithologies, including the Sintra granites (Terrinha et al., 2003). The density and susceptibility values for the Estremadura Spur Intrusion (Table 6.1) are comparable with the values obtained by Terrinha et al. (2003) and Ribeiro et al. (2013). Comparing the results of both studies with the values of the ESI it is possible to infer that its most likely magmatic nature is predominantly gabbroic. Although a gabbroic nature is interpreted as the dominant lithology for the Estremadura Spur Intrusion, one cannot exclude the possibility of the model reflecting a mixture of magmas with different nature, as it is found in the onshore analogues.

Neres et al. (2014) conducted a paleomagnetic study on the Foz da Fonte sill, obtaining values for bulk susceptibility varying from 0.03 SI and 0.067 SI. The susceptibility value for Estremadura Spur Intrusion is included in this interval of susceptibility values obtained for this Cretaceous sill.

Neres et al. (2018) introduced a new magnetic study of the Guadalquivir and Portimão Banks, including gravity and magnetic modelling and 3D inversion of magnetic data. The authors interpreted this bathymetric feature as an intrusion but made no conclusions about its magmatic nature. According to the similarity and alignment with the Sintra-Sines-Monchique onshore massifs, the authors suggest that this intrusion likely represents the southernmost expression of the Late Cretaceous magmatic event. This intrusion was modelled with a density of 2.9 g/cm^3 and susceptibility of 0.05 SI.

Comparing the values obtained by Neres et al. (2018) and the values for the ESI: the density of the Guadalquivir-Portimão Bank is higher than the ESI density value, however the value of susceptibility is the same.

There are several considerations that support considering the Estremadura Spur Intrusion as part of the wider Late Cretaceous magmatic event:

- Preliminary seismic stratigraphy criteria, and considering the ESI is disturbing post-rift strata, this intrusion is assigned as part of this magmatic event, in accordance with outcropping analogues of the WIM.
- The similarities between the combined gravity and magnetic models of the ESI and the Sintra massif, namely for its geometry (laccolith) and an interpreted predominantly gabbroic nature.
- The Fontanelas volcano was associated with the Late Cretaceous magmatic event (Miranda, 2010). This volcano is basaltic in nature, which is the extrusive equivalent of the gabbro.
- The similarities between the density and, notably, the susceptibility values obtained in Neres et al. (2018), who also relate the Guadalquivir-Portimão intrusion to the Late Cretaceous magmatic cycle.

In summary, the similarities in the density and susceptibility values between the ESI and the other magmatic bodies previously mentioned corroborate with the hypothesis of this intrusion be a part of the Late Cretaceous magmatic event.

Ultimately, the results presented in this study bear implication and can be integrated into future analysis, namely:

- For revised models of the geodynamic evolution of the WIM, especially in a post-rift setting, considering the magmatism more widespread than initially anticipated, confirming hypothesis presented by other published scientific literature (e.g. Neres et al., 2014).
- The existing magmatic models and the emplacement mechanisms of the Late Cretaceous magmatic event of the WIM:
    - The alkaline magma ascended through ruptures in the lithosphere and/or due to the thinning generated during the rotation of the Iberian plate (Ribeiro et al., 1979).
    - The generation and installation of the aligned Sintra-Sines-Monchique complexes along deep seated faults reactivated after the Jurassic rifting (Terrinha, 1998).
    - A fracture caused by a meteorite impact arguably formed the Tore seamount crater, resulting in the alignment of magnetic anomalies along the Estremadura Spur (Ribeiro, 2002).
    - A wide mantle plume or thermal anomaly emitted scattered magmatic pulses during the complex motion of Iberia (Merle et al., 2009).
    - A northward motion of the Iberian plate above a mantle plume (hot-spot; Grange et al., 2010). However, this hypothesis was excluded since the plate motion is not supported by paleomagnetic data (e.g. Neres et al., 2012).
    - Tore-Sintra tectono-magmatic lineament of intrusive/extrusive alkaline bodies (Neres et al., 2014).
- The impact on petroleum systems, including its influence on the maturation of hydrocarbons and the preservation/destruction of reservoir properties and sealing potential of these igneous rocks.

Chapter 7: Conclusions and final considerations

The northwest Iberian Margin was investigated using potential field data, in order to clarify the nature and geometry of some enigmatic evidence of Late Cretaceous magmatism and its implications for the evolution on this segment of the Newfoundland-Iberia conjugate margins. The results of this analysis reveal that:

- The methodology applied in this study was validated through the development of the work because it was possible to successfully accomplish the goals initially defined.
- The Estremadura Spur is the locus of two distinct magmatic features, namely a volcanic edifice (the Fontanelas volcano, e.g. Miranda et al., 2009; Pereira et al., 2017) and a magmatic intrusion described here for the first time, the Estremadura Spur Intrusion (ESI).
- The qualitative analysis of potential field data, performed in chapter 4, allowed to perform a regional characterization of the Fontanelas volcano and the Estremadura Spur Intrusion, namely the nearly circular shape of the anomalies caused by these source bodies. This preliminary study conducted to a more detailed analysis.
- The most relevant results obtained by 2.5D modelling allowed to perform a comprehensive characterization of these magmatic features estimating their magmatic nature and a possible geometry.
- The geometry of the Fontanelas volcano, based on results from both gravity and magnetic models, is characterised by an approximately triangular shape. This magmatic feature can be subdivided into two segments: a seawater-rock contact zone and a buried zone. The density (D=2.6 g/cm^3) and susceptibility (S= 0.07 SI) values for the buried sector indicated a possible basaltic nature. On the other hand, the density (D=2.45 g/cm^3) and susceptibility (S=0.05 SI) for the contact zone of the volcano indicated an alteration on its original basaltic nature.
- Regarding the geometry of the Estremadura Spur Intrusion, it is interpreted as a laccolith (sheet-like magmatic structure). Although the conclusions regarding its magmatic affinities are not straightforward, the values of density (D= 2.7 g/cm3) and susceptibility (S=0.05 SI) for this magmatic feature suggest the presence of a predominantly gabbroic intrusion, which is similar in nature with outcropping intrusions (Sintra and Sines) and offshore the Algarve margin (Guadalquivir-Portimão Bank).
- The Fontanelas volcano was interpreted as part of the Late Cretaceous magmatic event (Miranda, 2010). According to seismic information and due to the similarities between onshore and offshore analogues intrusions on the WIM it was also possible to link the Estremadura Spur Intrusion with this magmatic cycle.
- It was possible to confirm the results concerning the Fontanelas volcano due to the availability of published data. Being able to constraint its lithology allows for a greater degree of confidence in the results/interpretation of the Estremadura Spur Intrusion.
- The results obtained in this thesis may have implications on the current models describing the evolution of the Iberian margin, the existing magmatic models and emplacement mechanisms of the Late Cretaceous magmatic event, as well as on petroleum systems.

As suggestions for future work, it is included:

- To perform a 3D inversion of potential field data (separately or jointly). This is important to validate the results obtained with the 2.5D modelling, particularly the geometry of the bodies, namely the Estremadura Spur Intrusion and the Fontanelas volcano.
- To perform a Magnetization Vector Inversion (MVI), to obtain information about the magnetization of the area (namely, where the 3D survey was performed). This method is important to identify and characterise the presence of remanent magnetisation because there is an indication that it may prevail in some of the modelled magnetic sources. This method is available in the VOXI package of the Oasis Montaj from Geosoft.
- Perform 2.5D modelling in other regional lines over the Estremadura Spur Intrusion, given the positive results in this study.
- Conduct an oceanographic campaign on the Estremadura Spur Intrusion and the Fontanelas Seamount, including rock sampling, in order to validate the results of this study.

References

Alves, T.M., Moita, C., Cunha, T., Ullnaess, M., Myklebust, R., Monteiro, J.H., Manuppella, G., 2009. Diachronous evolution of late jurassic-cretaceous continental rifting in the northeast atlantic (west iberian margin). Tectonics 28, 1–32. https://doi.org/10.1029/2008TC002337

Azerêdo, A.C., Duarte, L. V., Henriques, M.H., Manuppella, G., 2003. Da dinâmica continental no Triásico aos mares do Jurássico Inferior e médio, Cadernos de Geologia de Portugal. Instituto Geológico e Mineiro.

Badagola, A., 2008. Evolução morfo-tectónica da plataforma continental do Esporão da Estremadura. Faculdade de Ciências da Universidade de Lisboa.

Badagola, A., Rodrigues, A., Terrinha, P., Veiga, L., 2006. Caracterização geomorfológica da plataforma continental do Esporão da Estremadura, in: VII Congresso Nacional de Geologia. Évora, pp. 377–380.

Bernard, P., Autin, J., Munschy, M., Maire, P. Le, 2019. Revised interpretation of magnetic anomalies in magma-poor rifted margins : case study of the Australia-Antarctica Basin, in: EGU General Assembly.

Bevan, B.W., 2017. Analysis of dipolar magnetic anomalies.

Blakely, R.J., 1995. Potential theory in gravity and magnetic applications. Cambridge University Press.

Blakely, R.J., Connard, G.G., Curto, J.B., 2016. Tilt Derivative Made Easy. Energy Geosci.

Boillot, G., Malod, J.A., Mougenot, D.-, 1979. Évolution géologique de la marge ouest-ibérique. Ciências da Terra 5, 215–222.

Bronner, A., Sauter, D., Manatschal, G., Péron-Pinvidic, G., Munschy, M., 2011. Magmatic breakup as an explanation for magnetic anomalies at magma-poor rifted margins. Nat. Geosci. 4, 549–553. https://doi.org/10.1038/ngeo1201

Casacão, J., Fernandes, S., Silva, F., Rocha, J., 2018. Frontier exploration in the Peniche Basin (West Iberia Margin): New insights from recent 3D seismic and Grav-Mag modeling, in: CONJUGATE MARGINS CONFERENCE 2018.

Corti, G., Bonini, M., Conticelli, S., Innocenti, F., Manetti, P., Sokoutis, D., 2003. Analogue modelling of continental extension: A review focused on the relations between the patterns of deformation and the presence of magma. Earth-Science Rev. 63, 169–247. https://doi.org/10.1016/S0012-8252(03)00035-7

Dias, R., Ribeiro, A., 1995. The Ibero-Armorican Arc: A collision effect against an irregular continent? Tectonophysicsc 246, 113–128. https://doi.org/https://doi.org/10.1016/0040-1951(94)00253-6

Doré, T., Lundin, E., 2015. Hyperextended continental margins — Knowns and unknowns 43, 95–96. https://doi.org/10.1016/0040

Duarte, J.C., Rosas, F.M., Terrinha, P., Schellart, W.P., Boutelier, D., Gutscher, M., Ribeiro, A., 2013. Are subduction zones invading the Atlantic ? Evidence from the southwest. Geology 41, 839–842. https://doi.org/10.1130/G34100.1

Escada, C., Santos, F., Represas, P., Pereira, R., Mata, J., 2019. Post-rift magmatism on the central West Iberian Margin : New evidence from magnetic and gravimetric data inversion in the Estremadura Spur, in: EGU General Assembly. https://doi.org/10.1144/jgs2016-050

Franke, D., 2012. Rifting, lithosphere breakup and volcanism: Comparison of magma-poor and volcanic rifted margins. Mar. Pet. Geol. https://doi.org/10.1016/j.marpetgeo.2012.11.003

Galice, G., 1977. 33. THE CONTINENTAL MARGIN OFF GALICIA AND PORTUGAL: ACOUSTICAL STRATIGRAPHY, DREDGE STRATIGRAPHY, AND STRUCTURAL

EVOLUTION Groupe Galice 1,2,3.

Geoffroy, L., 2005. Volcanic passive margins. Comptes Rendus - Geosci. 337, 1395–1408. https://doi.org/10.1016/j.crte.2005.10.006

Geoffroy, L., Burov, E.B., Werner, P., 2015. Volcanic passive margins: Another way to break up continents. Sci. Rep. 5, 1–12. https://doi.org/10.1038/srep14828

Geosoft, 2015a. Calculating the Energy Spectrum in MAGMAP, in: MAGMAP Filtering How-To Guide. pp. 1–5.

Geosoft, 2015b. Calculating the Analytic Signal and Generalised and Tilt Derivatives in MAGMAP, in: MAGMAP Filtering How-To Guide. p. 4.

Geosoft, 2013. Geosoft Oasis Montaj Geophysics How-to Guide: Applying Filters with montaj Geophysics.

Girolami, C., Barchi, M.R., Pauselli, C., Heyde, I., 2016. Use of gravity potential field methods for defining a shallow magmatic intrusion : the Mt . Amiata case history (Tuscany , Central Italy), in: EGU General Assembly 2019.

Grange, M., Scharer, U., Merle, R., Girardeau, J., Cornen, G., 2010. Plume-lithosphere interaction during migration of cretaceous alkaline magmatism in SW Portugal: Evidence from U-Pb Ages and Pb-Sr-Hf isotopes. J. Petrol. 51, 1143–1170. https://doi.org/10.1093/petrology/egq018

Gubbins, D., Herrero-Bervera, E. (Eds.), 2007. Encyclopedia of geomagnetism and paleomagnetism.

Hay, W.W., DeConto, R., Wold, C.N., Wilson, K.M., Voigt, S., Schulz, M., Wold-Rossby, A., Dullo, W.-C., Ronov, A.B., Balukhovsky, A.N., Soeding, E., 1999. Alternative global Cretaceous paleogeography, in: Barrera, E., Johnson, C. (Eds.), The Evolution of Cretaceous Ocean/Climate Systems. Geological Society of America Special Paper, pp. 1–47.

Lichoro, C.M., n.d. GRAVITY AND MAGNETIC METHODS, in: Short Course I on Exploration and Development of Geothermal Resources. p. 7.

Magee, C., Stevenson, C.T.E., Ebmeier, S.K., Keir, D., Hammond, J.O.S., Gottsmann, J.H., Whaler, K.A., Schofield, N., Jackson, C.A.L., Petronis, M.S., O'Driscoll, B., Morgan, J., Cruden, A., Vollgger, S.A., Dering, G., Micklethwaite, S., Jackson, M.D., 2018. Magma plumbing systems: A geophysical perspective. J. Petrol. 59, 1217–1251. https://doi.org/10.1093/petrology/egy064

Manatschal, G., 2014. New models for evolution of magma-poor rifted margins based on a review of data and concepts from West Iberia and the Alps. https://doi.org/10.1007/s00531-004-0394-7

Manatschal, G., Bernoulli, D., 1999. Architecture and tectonic evolution of nonvolcanic margins: Present-day Galicia and ancient Adria. Tectonics 18, 1099–1119. https://doi.org/10.1029/1999TC900041

Manatschal, G., Bernoulli, D., 1998. Rifting and early evolution of ancient ocean basins: the record of the Mesozoic Tethys and of the Galicia-Newfoundland margin. Mar. Geophys. Res. 20, 371–381.

Manatschal, G., Sutra, E., Péron-Pinvidic, G., 2010. The lesson from the Iberia-Newfoundland rifted margins : how applicable is it to other rifted margins ?, in: Central & North Atlantic Conjugate Margins Conference: Re-Discovering the Atlantic, New Winds for an Old Sea. Lisbon, pp. 27–37.

Martins, L., Miranda, R., Alves, C., Mata, J., Madeira, J., Munhá, J., Terrinha, P., Youbi, N., Bensalah, K., 2010. Mesozoic magmatism at the West Iberian Margins : timing and geochemistry, in: Central & North Atlantic Conjugate Margins Conference: Re-Discovering the Atlantic, New Winds for an Old Sea. Lisbon, pp. 172–175.

Martins, L.T., Madeira, J., Youbi, N., Munhá, J., Mata, J., Kerrich, R., 2008. Rift-related magmatism of the Central Atlantic magmatic province in Algarve, Southern Portugal. Lithos 101, 102–124. https://doi.org/10.1016/j.lithos.2007.07.010

Mata, J., Alves, C.F., Martins, L., Miranda, R., Madeira, J., Pimentel, N., Martins, S., Azevedo, M.R., Youbi, N., De Min, A., Almeida, I.M., Bensalah, M.K., Terrinha, P., 2015. 40Ar/39Ar ages and petrogenesis of the West Iberian Margin onshore magmatism at the Jurassic-Cretaceous transition: Geodynamic implications and assessment of open-system processes involving saline materials. Lithos 236–237, 156–172. https://doi.org/10.1016/j.lithos.2015.09.001

Mauffret, A., Mougenot, D., Miles, P.R., Malod, J.A., 1989. Cenozoic deformation and Mesozoic abandoned spreading centre in the Tagus Abyssal Plain (west of Portugal): results of a multichannel seismic survey. Can. J. Earth Sci. 26, 1101–1123. https://doi.org/https://doi.org/10.1139/e89-095

Merle, O., 2011. A simple continental rift classification. Tectonophysics 513, 88–95. https://doi.org/10.1016/j.tecto.2011.10.004

Merle, R., Jourdan, F., Girardeau, J., 2018. Geochronology of the Tore-Madeira Rise seamounts and surrounding areas: a review. Aust. J. Earth Sci. 65, 591–605. https://doi.org/10.1080/08120099.2018.1471005

Merle, R., Jourdan, F., Marzoli, A., Renne, P.R., Grange, M., Girardeau, J., 2009. Evidence of multi-phase Cretaceous to Quaternary alkaline magmatism on Tore-Madeira Rise and neighbouring seamounts from 40Ar/39Ar ages. J. Geol. Soc. London. 166, 879–894. https://doi.org/10.1144/0016-76492008-060

Meyer, B., Saltus, R., Chulliat, A., 2017. EMAG2: Earth Magnetic Anomaly Grid (2-arc-minute resolution) Version 3. [WWW Document]. Natl. Centers Environ. Information, NOAA. https://doi.org/10.7289/V5H70CVX

Miranda, R., 2010. Petrogenesis and Geochronology of the Late Cretaceous Alkaline Magmatism in the West Iberian Margin.

Miranda, R., Terrinha, P., Mata, J., Azevedo, R., Chadwick, J., Lourenço, N., Moreira, M., 2010. Caracterização geoquímica do monte submarino de Fontanelas , Margem Oeste Ibérica, in: Flores, D., Marques, M. (Eds.), X Congresso de Geoquímica Dos Países de Língua Portuguesa, XVI Semana de Geoquímica. Universidade do Porto (Porto), pp. 151–156.

Miranda, R., Valadares, V., Terrinha, P., Mata, J., Azevedo, M. do R., Gaspar, M., Kullberg, C., Ribeiro, C., 2009. Age constraints on the Late Cretaceous alkaline magmatism on the West Iberian Margin. Cretac. Res. 30, 575–586. https://doi.org/10.1016/j.cretres.2008.11.002

Mougenot, D., 1989. Geologia da Margem Portuguesa. Documento Técnico n^{o}32, Instituto Hidrográfico.

Neres, M., Bouchez, J.L., Terrinha, P., Font, E., Moreira, M., Miranda, R., Launeau, P., Carvallo, C., 2014. Magnetic fabric in a Cretaceous sill (Foz da Fonte, Portugal): Flow model and implications for regional magmatism. Geophys. J. Int. 199, 78–101. https://doi.org/10.1093/gji/ggu250

Neres, M., Font, E., Miranda, J.M., Camps, P., Terrinha, P., Mirão, J., 2012. Reconciling Cretaceous paleomagnetic and marine magnetic data for Iberia: New Iberian paleomagnetic poles. J. Geophys. Res. Solid Earth 117. https://doi.org/10.1029/2011JB009067

Neres, M., Terrinha, P., Custódio, S., Silva, S.M., Luis, J., 2018. Geophysical evidence for a magmatic intrusion in the ocean-continent transition of the SW Iberia margin. Tectonophysics 744, 118–133. https://doi.org/10.1016/j.tecto.2018.06.014

NGA, 2004. GM-SYS: Gravity/Magnetic Modeling Software - User's Guide Version 4.9:01.

Ocdanologique, O., Azur, G., 2001. Non-volcanic rifted margins , continental break-up and the onset of sea-floor spreading : some outstanding questions 9–30.

Pereira, R., 2013. Continental rifting and post breakup evolution of Southwest Iberia: Tectono-stratigraphic record of the first segment of the North Atlantic Ocean.

Pereira, R., Alves, T.M., 2012. Tectono-stratigraphic signature of multiphased rifting on divergent

margins (deep-offshore Southwest Iberia , North Atlantic). Tectonics 31, 1–21. https://doi.org/10.1029/2011TC003001

Pereira, R., Alves, T.M., 2011. Post-rift compression on the Southwest Iberian margin (Eastern North Atlantic): A case of prolonged inversion in the Ocean-Continent Transition. J. Geol. Soc. London. 168, 1249–1263. https://doi.org/10.1144/0016-76492010-151

Pereira, R., Alves, T.M., Mata, J., 2017. Alternating crustal architecture in West Iberia : a review of its significance in the context of NE Atlantic rifting. J. Geol. Soc. London. 174, 522–540. https://doi.org/https://doi.org/10.1144/jgs2016-050

Pinheiro, L.M., Wilson, R.C.L., Reis, R.P., Whitmarsh, R.B., Ribeiro, A., 1996. The Western Iberia Margin: a geophysical and geological overview 149.

Proença Cunha, P., Pena dos Reis, R., 1995. Cretaceous-sedimentary-and-tectonic-evolution-of-the-northern-pdf. Cretac. Res.

Ramalho, M., Pais, J., Rey, J., Berthou, P.Y., Alves, C.A.M., Palácios, T., Leal, N., Kullberg, M.C., 1993. Notícia explicativa da folha 34-A Sintra, Serviços Geológicos de Portugal.

Rasmussen, E.S., Lomholt, S., Andersen, C., Vejbæk, O. V., 2013. Aspects of the structural evolution of the Lusitanian Basin in Portugal and the shelf and slope area offshore Portugal. Tectonophysics 300, 199–225. https://doi.org/10.1016/S0040-1951(98)00241-8

Ravat, D., 2007. Upward and Downward Continuation, in: Gubbins, D., Herrero-Bervera, E. (Eds.), Encyclopedia of Geomagnetism and Paleomagnetism. Springer, pp. 974–976. https://doi.org/10.1007/978-1-4020-4423-6

Reid, A.B., Allsop, J.M., Granser, H., Millet, A.J., Somerton, I.W., 1990. Magnetic interpretation in three dimensions using Euler deconvolution. Geophysics 55, 81–91. https://doi.org/10.1190/1.1892190

Reid, A.B., Ebbing, J., Webb, S.J., 2014. Avoidable Euler Errors - the use and abuse of Euler deconvolution applied to potential fields. Geophys. Prospect. 62, 1162–1168. https://doi.org/10.1111/1365-2478.12119

Reston, T.J., 2016. The formation of non-volcanic rifted margins by the progressive extension of the lithosphere : the example of the West Iberian margin 77–110.

Ribeiro, A., 2002. Soft Plate and Impact Tectonics. Springer.

Ribeiro, A., Antunes, M., Ferreira, M., Rocha, R., Soares, A., Zbyszewski, G., De Almeida, F.M., De Carvalho, D. Monteiro, J., 1979. Introduction à la géologie générale du Portugal. Serviços Geológicos Port.

Ribeiro, P., Silva, P.F., Moita, P., Kratinová, Z., Marques, F.O., Henry, B., 2013. Palaeomagnetism in the Sines massif (SW Iberia) revisited: Evidences for late cretaceous hydrothermal alteration and associated partial remagnetization. Geophys. J. Int. 195, 176–191. https://doi.org/10.1093/gji/ggt261

Robert L. Mcpherron, 2019. Geomagnetic field [WWW Document]. Encycl. Br. inc. URL https://www.britannica.com/science/geomagnetic-field (accessed 8.8.19).

Roque, C., Terrinha, P., Lourenço, N., Abreu, M.P. De, 2009. Morphostructure of the Tore Seamount and evidences of recent tectonic activity (West Iberia Margin), in: 6º Simposio Sobre El Margen Ibérico Atlántico. Oviedo, pp. 1–4.

Russell, S.M., Whitmarsh, R.B., 2003. Magmatism at the west Iberia non-volcanic rifted continental margin : evidence from analyses of magnetic anomalies 706–730.

Salem, A.S., Williams, S., Ravat, D., Smith, R.S., 2007. Tilt-depth method : A simple depth estimation method using first-order magnetic derivatives. Lead. Edge. https://doi.org/10.1190/1.2821934

Sanchez, G., Sanchez, G., Merle, R., Hinschberger, F., Thinon, I., 2019. Post-spreading deformation

and associated magmatism along the Iberia- Morocco Atlantic margins : Insight from submarine volcanoes of the Tore- Madeira Rise Post-spreading deformation and associated magmatism along the Iberia- Morocco Atlantic margins : In. https://doi.org/10.1016/j.margeo.2018.10.011

Sengör, A.M.C., Burke, K., 1978. Relative timing of rifting and volcanism on Earth and its tectonic implications. Geophys. Res. Lett. 5, 419–421. https://doi.org/https://doi.org/10.1029/GL005i006p00419

Shahverdi, M., Namaki, L., Montahaei, M., 2017. Interpretation of magnetic data based on Tilt derivatie methods and enhancement of total horizontal gradient, a case study : Zanjan Depression. J. Earth Sp. Phys. 43, No. 1, 8.

Singh, P.K., Gupta, M.K., Kara, V., Paul, P.K., Dasgupta, R., 2010. 3D Seismic survey using swath or patch-centered shooting : A comparative analysis, in: 8th Bienal Internation Conference & Exploration on Petroleum Geophysics.

Soares, D.M., Alves, T.M., Terrinha, P., 2012. The breakup sequence and associated lithospheric breakup surface: Their significance in the context of rifted continental margins (West Iberia and Newfoundland margins, North Atlantic). Earth Planet. Sci. Lett. 355, 311–326.

Srivastava, S.P., Sibuet, J.C., Cande, S., Roest, W.R., Reid, I.D., 2000. Magnetic evidence for slow seafloor spreading during the formation of the Newfoundland and Iberian margins. Earth Planet. Sci. Lett. 182, 61–76. https://doi.org/10.1016/S0012-821X(00)00231-4

Telford, W.M., Geldart, L.P., Sheriff, R.E., 1990. Applied Geophysics, Second. ed. Cambridge University Press.

Terrinha, P., Aranguren, A., Kullberg, M.C., Pueyo, E.L., 2003. Complexo ígneo de Sintra – um modelo de instalação constrangido por novos dados de gravimetria e ASM.

Terrinha, P., Kullberg, J.C., Neres, M., Alves, T., Ramos, A., Ribeiro, C., Mata, J., Pinheiro, L., Afilhado, A., Matias, L., Luís, J., Muñoz, J.A., 2019. Rifting of the Southwest and West Iberia Continental Margins, in: Quesada, C., Oliveira, J.T. (Eds.), The Geology of Iberia: A Geodynamic Approach. Springer International Publishing, pp. 251–283. https://doi.org/10.1007/978-3-030-11295-0

Terrinha, P., Pueyo, E.L., Aranguren, A., Kullberg, J.C., Kullberg, M.C., Casas-Sainz, A., Azevedo, M. do R., 2017. Gravimetric and magnetic fabric study of the Sintra Igneous complex: laccolith-plug emplacement in the Western Iberian passive margin. Int. J. Earth Sci. 107, 1807–1833. https://doi.org/10.1007/s00531-017-1573-7

Terrinha, P.A.G., 1998. Structural Geology and Tectonic Evolution of the Algarve Basin, South Portugal. Imperial College London (University of London).

Thompson, L., LaCoste, L., 1960. Aerial gravity measurements. J. Geophys. Res. 65, 305–322.

Tucholke, Brian E, Sibuet, J., 2007. LEG 210 synthesis: Tectonic, magmatic and sedimentary evolution of the Newfoundland-Iberia rift, in: Tucholke, B.E., Sibuet, J.-C., Klaus, A. (Eds.), Proceedings of the Ocean Drilling Program, Scientific Results. https://doi.org/10.2973/odp.proc.sr.210.101.2007

Verati, C., Rapaille, C., Féraud, G., Marzoli, A., Bertrand, H., Youbi, N., 2007. 40Ar/39Ar ages and duration of the Central Atlantic Magmatic Province volcanism in Morocco and Portugal and its relation to the Triassic-Jurassic boundary. Palaeogeogr. Palaeoclimatol. Palaeoecol. 244, 308–325. https://doi.org/10.1016/j.palaeo.2006.06.033

Verduzco, B., Fairhead, J.., Green, C.., MacKenzie, C., 2004. New insights into magnetic derivatives for structural maping. Lead. Edge 23, 116–119. https://doi.org/10.1190/1.1651454

Wilson, R.C.L., 1988. Mesozoic Development of the Lusitanian Basin, Portugal. Rev. Soc. Geol. Espanha I, 393–407.

Wilson, R.C.L., Manatschal, G., Wise, S., 2001. Rifting along non-volcanic passive margins :

Stratigraphic and seismic evidence from the Mesozoic successions of the Alps and Western Iberia, in: Wilson, R.C.L., Whitmarsh, R.B., Taylor, B., Froitzheim, N. (Eds.), Non-Volcanic Rifting of Continental Margins: A Comparison of Evidence from Land and Sea. Geological Society of London, Special Publications, pp. 429–452. https://doi.org/10.1144/GSL.SP.2001.187.01.21

Won, I.J., Bevis, M., 1987. Computing the gravitational and magnetic anomalies due to a polygon: algorithms and Fortran subroutines. Geophysics 52, 232–238.

Annexes

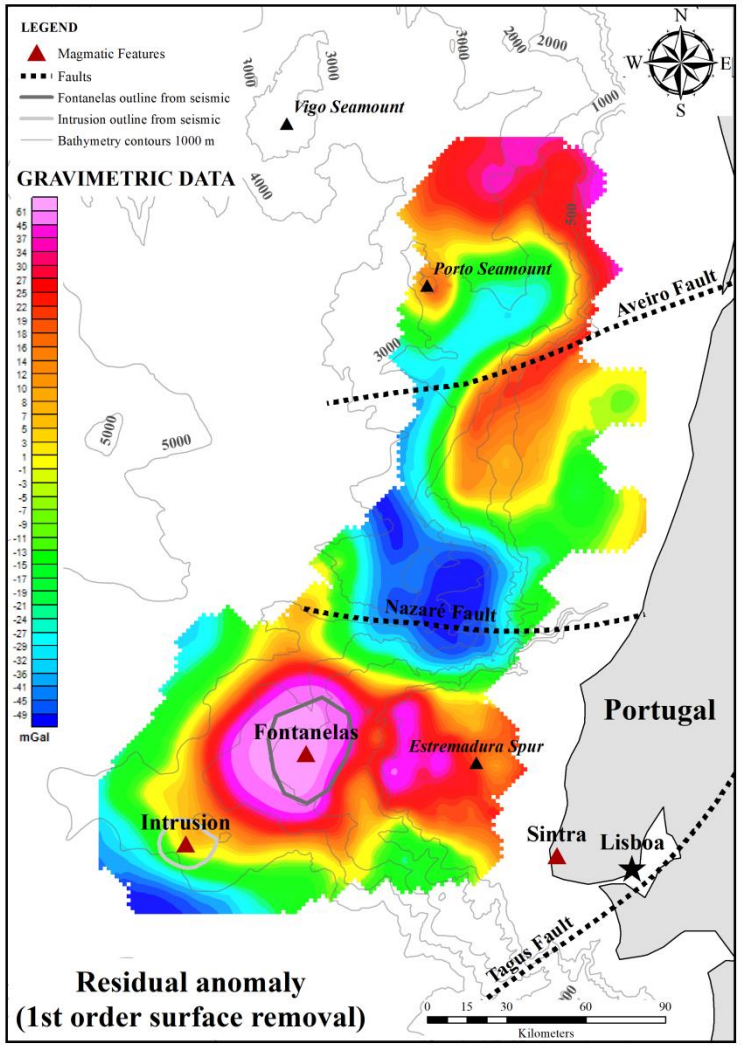

Annex 1. Residual anomaly map calculated through the polynomial surface adjustment.

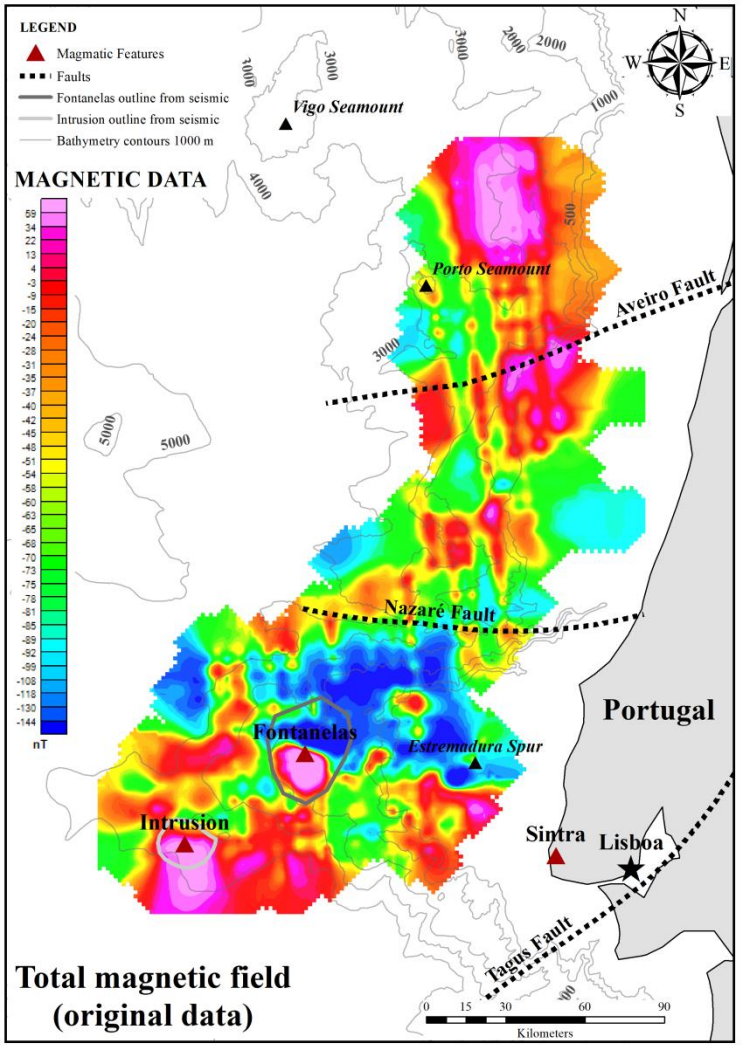

Annex 2. Total magnetic field map (original data).

2D Modeling (Extended profile)

Gravimetric data

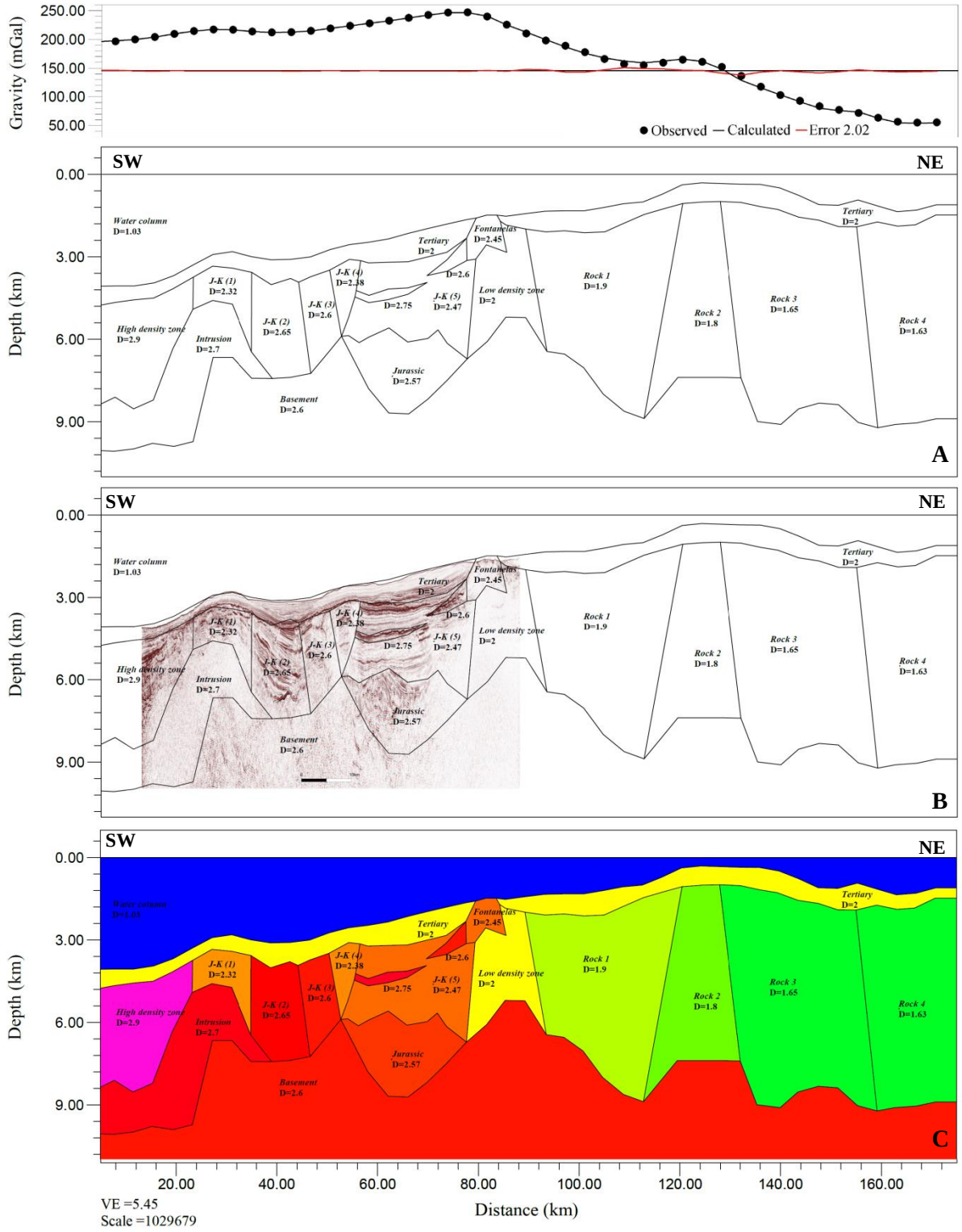

Annexe 3. Extended gravity 2D model: **A)** panel with the susceptibility values and the structure of each block, **B)** panel with the seismic background image, the susceptibility values and structure of each block and **C)** the colour of each block it is in accordance with density's colour scale. The model profile has the same direction as the (A-A') profile presented in Figure 4.2, over the Bouguer anomaly map, and is extended to the edges of the acquisition area.

Annexe 4. Table of densities adapted from Telford et al. (1990).

Lithology	Range (g/cm^3)	Average (g/cm^3)	Lithology	Range (g/cm^3)	Average (g/cm^3)
Sandstone	1.61 - 2.76	2.35	Gabbro	2.70 – 3.50	3.03
Limestone	1.93 - 2.90	2.55	Basalt	2.70 - 3.30	2.99
Sedimentary	-	2.50	Acid igneous	2.30 - 3.11	2.61
Granite	2.50 - 2.81	2.64	Basic igneous	2.09 - 3.17	2.79
Rhyolite	2.35 – 2.70	2.52	Quartzite	2.50 – 2.70	2.60
Diorite	2.72 - 2.99	2.85	Serpentine	2.40 – 3.10	2.78
Andesite	2.40 - 2.80	2.61	Metamorphic	2.40 – 3.10	2.74

Annexe 5. Table of susceptibilities adapted from Telford et al. (1990).

Lithology	Range (SI)	Average (SI)	Lithology	Range (SI)	Average (SI)
Sandstone	0-0.02	0.0004	Gabbro	0.001-0.09	0.07
Limestone	0-0.003	0.0003	Basalt	0.0002-0.175	0.07
Sedimentary	0-0.018	0.0009	Acid igneous	0-0.08	0.008
Granite	0-0.05	0.0025	Basic igneous	0.0005-0.097	0.025
Rhyolite	0.0002-0.035	0.017	Quartzite		0.004
Diorite	0.0006- 0.12	0.085	Serpentine	0.003-0.017	
Andesite		0.16	Metamorphic	0-0.07	0.0042